4-7-2016

Mechanical Integrity and Fabrication of Carbon Nanotube/Copper-based Through Silicon Via

Ibrahim E. Awad
University of Connecticut, ibrahim.awad@uconn.edu

Mechanical Integrity and Fabrication of Carbon Nanotube/Copper-based Through Silicon Via

Ibrahim Awad

University of Connecticut, 2016

Three-dimensional integrated circuits' (3D ICs') market demands for further miniaturized microelectronics devices are growing drastically. Accordingly, miniaturized through silicon vias (TSVs) are sought in order to fulfill ever-growing market demands. Copper (Cu) is the state-of-the-art filling material for TSVs; however, required electrical current density in nano/microelectronics would exceed the breakdown limit of Cu in the next-generation microelectronics. This increased current density will exacerbate the electro-migration issues associated with using copper interconnects. Therefore, new materials with higher current capacity—ampacity—are needed in order to continue the same miniaturization trend. The proposed substitute is carbon nanotube/copper (CNT/Cu) composite. This composite material is deemed to offers substantial improvement in electrical, thermal and mechanical properties over copper material. It is proven that CNT/Cu-composite exhibits two order of magnitude higher ampacity than that of Cu.

Not only electrical properties of interconnects are important, mechanical behavior of these interconnects dictate their long term behavior and reliability of these interconnects. However, CNT/Cu mechanical properties are not well known in the literature. Furthermore, fabrication of defect free CNT/Cu composite material is yet to be accomplished limiting the experimental evaluation of these interconnects. Simulation and modeling offer a feasible preliminary way to understand the mechanical behavior of these novel materials. Hence, this study investigates the mechanical properties of the CNT/Cu-based TSV theoretically by conducting a multiscale

modeling technique. Molecular dynamics (MD) simulation is utilized to evaluate the CNT/Cu interfacial strength and to obtain cohesive zone model for the interface at the atomistic scale. Furthermore, coefficient of thermal expansion (CTE) of CNTs and axial stress-strain behavior are evaluated using MD simulations. At the micro level, finite element analysis is used to evaluate the mechanical integrity of CNT/Cu-TSV under bending and thermal loading conditions. Fatigue life of CNT/Cu-TSV is also estimated and compared with that of Cu-filled TSV. CNTs addition to Cu in TSVs is found to redistribute plastic deformation, in Cu, over two interfaces; Si/Cu and Cu/CNT. Thus, the maximum equivalent plastic strain amplitude is alleviated, since it is not concentrated at Si/Cu interface only in Cu-only-TSVs. Rather, it is distributed over the two surfaces. Accordingly, CNT/Cu-TSV has obtained a threefold increase in the fatigue life in the adopted representative model.

A systematic scale-up fabrication technique of CNT/Cu-TSV is investigated as well. Filling TSVs with high aspect ratio (4:1 or 5:1) self-aligned and dense CNTs is sought in order to achieve the sought properties of high conductivity in the axial direction. Several different techniques, such as electroless plating, electroplating and sputtering are used Cu deposition on vertically oriented CNTs. Different, catalysts and under-layer materials such as Ti, TiN and Al_2O_3 are used to evaluate the CNTs growth rate and to facilitate electroplating. Both thermal and plasma enhance chemical vapor depositions (CVD and PECVD) are used, growth rate, density, alignment and Cu deposition are evaluated. Using thermal CVD on Fe/Al_2O_3 (catalyst/under-layer) is found to give dense, self-aligned CNTs. Moreover, increasing growth temperature increases the growth rate. However, CNTs adhesion to the substrate is so weak that CNTs detaches from the surface during plating processes. Physical Cu deposition using sputtering covered only the surface of CNTs and could not infiltrate them deeply. On the other

hand, PECVD on Fe/TiN or Ni/TiN yields self-aligned CNTs and strongly anchored to the substrate. However, CNTs are less dense than CNTs grown using thermal CVD, and their growth rate is less by two orders of magnitude. Cu plating could not be conducted because of the high resistance of the substrate. Several alternative scenarios are proposed to overcome growth rate, adhesion and Cu deposition problems.

Mechanical Integrity and Fabrication of Carbon Nanotube/Copper-based Through Silicon Via

Ibrahim Awad

M.S., Cairo University, 2013

B.S., Cairo University, 2008

A Dissertation

Submitted in Partial Fulfillment of the

Requirements for the Degree of

Doctor of Philosophy

at the

University of Connecticut

2016

APPROVAL PAGE

Doctor of Philosophy Dissertation

Mechanical Integrity and Fabrication of Carbon Nanotube/Copper-based Through Silicon Via

Presented by
Ibrahim Awad

Major Advisor _____

Leila Ladani

Associate Advisor _____

Chengyu Cao

Associate Advisor _____

George Lykotrafitis

Associate Advisor _____

Jafar Razmi

Associate Advisor _____

Steven Suib

University of Connecticut
2016

ABBREVIATIONS AND SYMBOLS

Abbreviations:

ASE	Atomic simulation environment
CAGR	Compound annual growth rate
CNT	Carbon nanotube
Cu	Copper
CNT/Cu-TSV	Carbon nanotube/Copper- through silicon via
CNF	Carbon nanofibers
Cu-TSV	Copper-through silicon via
CVD	Chemical vapor deposition
CZM	Cohesive zone model
DRIE	Deep reactive ion etching
E-Beam	Electron-beam evaporation
EPS	Equivalent plastic strain
FE	Finite element
GIM	Global interconnect market
LAMMPS	Large-scale atomic/molecular massively parallel simulator
MD	Molecular dynamics
MFP	Mean free path
MWCNT	Multi-wall carbon nanotube
SWCNT	Single-wall carbon nanotube
PECVD	Plasma enhanced chemical vapor deposition
TSV	Through silicon via

Symbols:

α and β	Atoms in the specified domain
α_b	Basal angle
$\Delta\varepsilon_f$	Stabilized EPS amplitude
ε	Depth of the potential well
ε_f	Ductility of Cu
λ	Principal expansion ratio in the axial direction
σ	Finite distance
τ_{max}	Interfacial shear strength
a	Atomic spacing of Cu
C_{i0}	Material constant
CTE_a	Coefficient of thermal expansion in axial direction
CTE_r	Coefficient of thermal expansion in radial direction
c	Interfacial length
c_3	Fatigue ductility
d_i	MWCNT inner diameter
d_o	MWCNT outer diameter
d_z	Displacement in z-direction
$f_j^{\alpha\beta}$	Component of the force applied on atom α by atom β
F_{avg}	Average pull-out force
F	Pull-out force
F_o	Internal force due to adhesion
I_1	Strain invariant
i and j	Direction indices and take the values $x, y\ and\ z$
L	MWCNT current length
L_o	MWCNT initial length
m^α	Mass of atom α
N	Number of atoms neighboring atom α
N_f	Number of fatigue cycles

v_i^α and v_j^α	ith and jth velocity components of atom α respectively
r	Atoms position
r^{CNT}	MWCNT current radius
r_o^{CNT}	MWCNT initial radius
T	Current temperature
T_o	Initial temperature
V	Volume of the domain
W	Strain-energy density
w	Amount of work done to overcome vdW interaction
x	Displacement

ACKNOWLEDGMENTS

"I would like to express my immense gratitude to my advisor professor Leila Ladani, the National Science Foundation and the University of Connecticut for giving me the opportunity to conduct this research. I would like to thank my advisory committee members: professors Chengyu Cao, George Lykotrafitis, Jafar Razmi and Steven Suib for generously offering their time, support and guidance throughout the review of this dissertation. I could not have reached this point of my life without the enormous support of my family. Words are not enough to express my profound appreciation to my honorable teachers and professors throughout all my educational years in Cairo, Egypt and USA; they are my role model for ethical principles and scientific integrity. My inland and alien friends have been always my source of inspiration."

TABLE OF CONTENTS

LIST OF TABLES

LIST OF FIGURES

CHAPTER 1. INTRODUCTION

1.1 Problem Statement

Society's demand for easier, faster, and more efficient smaller means of communication that would provide a faster pace of life is growing drastically. As we approach the future, continuous miniaturization of silicon-based devices is becoming inevitable. Silicon-based devices are utilized as microelectronics in a wide range of applications that have great impact on society; from smart phones and wearable electronics to defense applications. Improvement of these applications—in terms of size, performance or functionality—is concurrent to the miniaturization of microelectronic devices. Microelectronic devices come in different forms (e.g. transistors, sensors, micro-electro-mechanical systems (MEMS) and 3D integrated circuit (3D IC) packages). In particular, 3D IC packages are addressed in this study. 3D IC packages promote the miniaturizability of microelectronics. 3D ICs exhibit some advantages over the 2D ICs which make them preferable in the microelectronic packages industry; higher overall package volume utilization, higher performance and higher band width [1]. One of the key components of a 3D IC package of devices is through silicon via (TSV). TSV's implementation is very significant to microelectronics manufacturers because of their unique

advantages associated with performance, bandwidth and space utilization [1,2]. TSVs are the main focus of this study. A TSV is a vertical interconnect access (via) passing completely through a silicon wafer or die to vertically connect multiple layers (Fig. 1) in 3D IC packages.

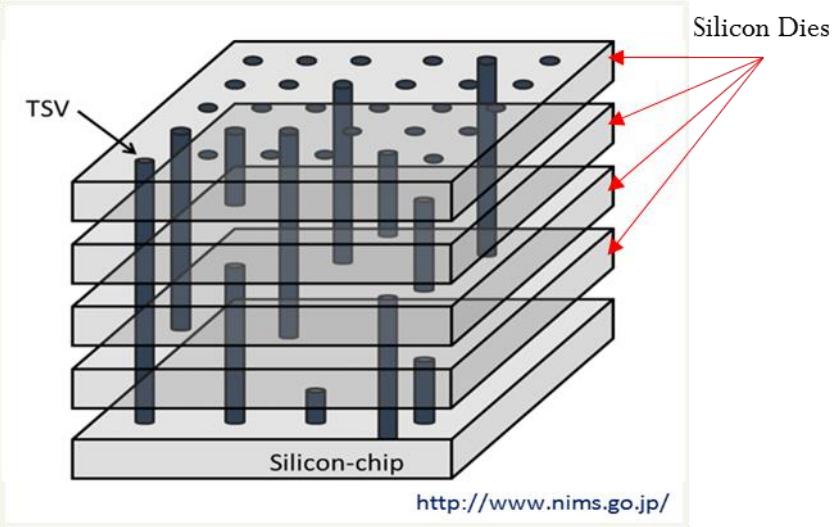

Fig. 1. Schematic of TSVs

There are several semiconductor manufacturers that are actively pursuing TSV technology such as Micron, Intel, Samsung, etc. Intel has presented versions of Ivy Bridge processor that incorporates TSVs into chip's architecture. Micron with collaboration of many other companies created that Hybrid Memory Cube (HBC) and it acquires 15x speed of DDR3. Copper (Cu) as the current technology has already fulfilled its potential for the current scales [1,3]. Semiconductor industry is trying to launch new product with increased functionality and speed and smaller interconnect size in order to fulfill the demanding microelectronics marked. Therefore, new materials and new designs are of great interest. Since electronic devices are constantly getting smaller to fulfill the market demands, miniaturized electronic packages are sought. TSVs market is growing drastically. Global interconnect market (CIM) forecasts a compound annual growth rate (CAGR) of 8.4% over the period 2014-2019 in TSVs' market

[4]. Also, Markets & Markets expected the 3D ICs and TSV interconnects market to grow from $2.21 billion in 2009 to $6.55 billion in 2016 at a CAGR of 16.9% over that period [5]. However, International Technology Roadmap for Semiconductors (ITRS) has already predicted that the current density would exceed the breakdown limit of Cu, state-of-the-art filling material for TSVs, in 2023 as shown in Fig. 2, since there would not be known solutions for the inherent electro-migration issues in Cu. Thus, finding novel candidate materials that exhibit higher ampacity and can replace Cu is believed to overcome the electro-migration issue in next-generation devices. Furthermore, in order to cope with the growing TSV market, a scale-up and systematic fabrication technique of this new material has to be provided. Therefore,

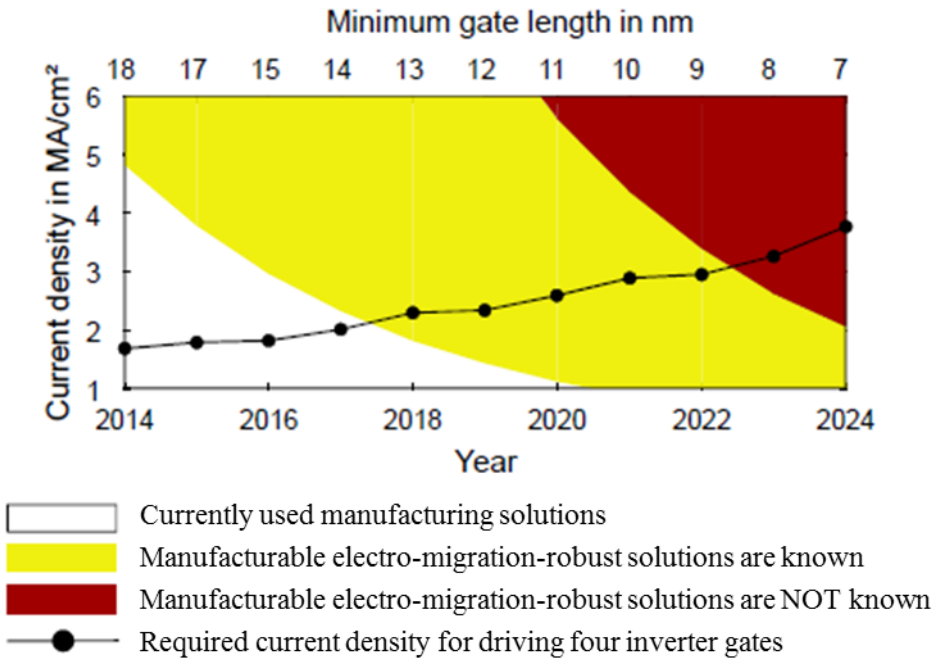

Fig. 2. Forecast of required current density and minimum gate length over the years (graph courtesy of ITRS)

Despite of Cu's excellent conductivity, there are some reliability issues that prohibit further miniaturization of TSVs; Cu is prone to failure due to high stresses in a deep via due to electro-migration caused by high current densities and resistance increases at further miniaturized scales [3]. The low current carrying capacity (ampacity) of Cu at these miniaturized scales is the major cause of electro-migration and low reliability accordingly. Also, Cu resistance increases at nanoscales because its low mean free path [6].

1.2 Proposed Solution

Novel materials with higher ampacity and reliability are prompted. Advanced materials such as graphene and CNTs have potential to transform the electronic industry [7–11] because of their high reliability and superior thermal, mechanical and electrical properties [12–14]. The extraordinary properties of CNTs make them ideal for high density and miniaturized devices. They also offer a great potential to replace the most common interconnect material, Cu. Cu is prone to electro-migration and its resistivity increases drastically at nanoscale. Researchers were able to report CNT/Cu-composite that attain similar conductivity to Cu but with a two orders of magnitude higher ampacity [15]. Higher ampacity is a critical factor in future nanoscale devices. Ampacity corresponds to the maximum current carrying capacity that is both structure- and material- dependent. Increasing ampacity will increase the reliability and the life-time and the performance accordingly. Thus, CNT/Cu-TSV could offer an efficient replacement to Cu-TSVs.

1.3 Background and Literature Review

1.3.1 *CNTs*

CNTs have been studied extensively since their discovery by Sumio Iijima [16,17]. Their extraordinary electrical and mechanical properties have drawn the attention of researchers in many aspects such as, in particular, Si-based devices [18–20]. These remarkable properties are attributed to the unique atomic structure and atomic bonding of CNTs at the nanoscale. However, these remarkable properties, inherent at the nanoscale, have not yet been obtained in the current technological applications due to manufacturing complexity and change of properties at micro-scales. For example, graphene (one layer of graphite) has very good 2-dimensional conductive properties, while graphite (multilayers of graphene sheets) obtains very poor electrical conductivity. CNTs are likewise.

1.3.1.1 *Structure*

CNT is an allotrope of carbon with cylindrical structure. A single single-walled CNT (SWCNT) is a wrapped graphene sheet. The wrapping direction ($\vec{c}$) of the graphene sheet defines the chirality of CNTs. There are two highly symmetric SWCNT structures; *armchair* and *zigzag*. They are named after the shape the hexagonal lattice makes around the axis perpendicular to the axis of the SWCNT. These two extreme symmetric structures of SWCNT are displayed in Fig. 3. A *chiral* SWCNT is a linear combination of the armchair and zigzag structures and it is defined by a unique chiral vector ($\vec{c} = n\boldsymbol{a_1} + m\boldsymbol{a_2}$), such that a_1 and a_2 are semi-orthogonal base vectors as indicated in Fig. 3. Parameters *n* and *m* are integers and the chiral vector is displayed in the form (*n*,*m*). A zigzag SWCNT is represented by chiral vector (*n*,0) and armchair SWCNT is represented by chiral vector (*n*,*n*).

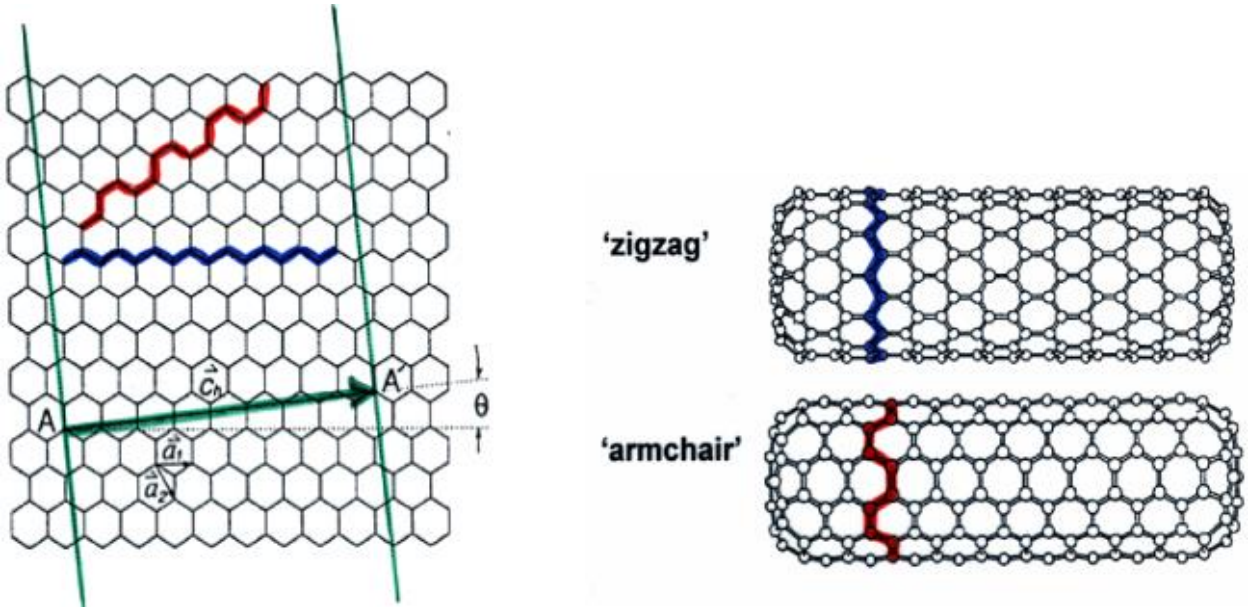

Fig. 3. Illustration of CNT's chirality [21]

CNTs are categorized into Single-Wall CNTs (SWCNTs) and Multi-Wall CNTs (MWCNTs) as shown in Fig. 4. A MWCNT consists of several nested SWCNTs and it is structurally similar to SWCNT. Diameter of SWCNT and MWCNT range from 0.8 to 2 nm and 5 to 20 nm, respectively; however, MWCNT diameters may exceed 100 nm [22].

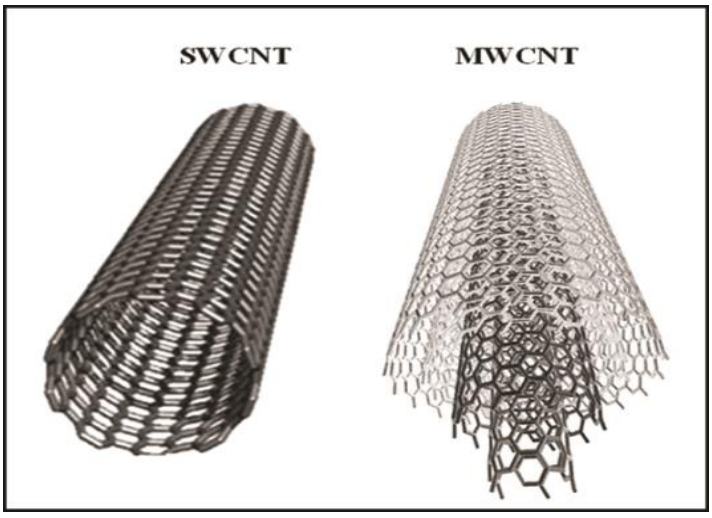

Fig. 4: SWCNT and MWCNT

1.3.1.2 *Electrical and Mechanical Properties*

Electrical conductivity of SWCNTs depends on their chirality. A SWCNT is considered *metallic* if *n-m* is divisible by three, which means that all armchair SWCNT are conducting. Otherwise, it is considered semiconducting [23]. So far, a systematic growth procedure to control the chirality of grown CNTs is still unknown. As-grown SWCNT forest is a mixture of both with 2/3 of the total being semiconducting and 1/3 conducting, while MWCNTs are all conducting [24]. For MWCNT, determination of conductivity is more complex, since it consists of shells with different chiralities; however, all MWCNTs exhibit metallic properties [25].

The excellent electrical properties of graphene and conducting CNTs are attributed to their atomic and bonding structure. A CNT consists of one or more nested graphene sheets. Each sheet consists of hexagons of carbon atoms. Every carbon atom is connected to other three atoms by sp^2 bonds, or sigma bonds, leaving behind a free electron. These high mobile electrons are called Pi-electrons and are located above and below the graphene sheet. These Pi electrons are traveling in overlapped Pi orbitals with minimal bumping into atoms or scattering. Accordingly, mean free path (MFP) increases and resistance becomes independent of length when the CNT's length is less than MFP. This phenomenon is called *ballistic transport* in SWCNT and *quasi-ballistic* in MWCNT due to the complex combination of chiralities of the different shells. In metals, free electrons bump into metal atoms. That creates some resistance and heat. This conventional way of electron transport follows Joule's Law.

This is not the case for CNTs where Ballistic Transport takes place and mean free path is increased [23].

CNTs exhibit very high tensile strength and Young's modulus—almost 200 times those of steel—because of the strong covalent sp^2 bonds between carbon atoms. Reported theoretical and experimental results has shown that tensile strength and Young's modulus are as high as 1 126 GPa and 1 TPa, respectively [26]. However, studies have found that mechanical properties are dependent of diameter, chirality and number of hells [26]. Table 1 summarizes the properties of CNTs with respect to those of Cu. CNTs exhibits extraordinary electrical and mechanical properties compared to Cu; 100× ampacity, 3× melting point, 100 to 200× tensile strength, 15× thermal conductivity and 600× the mean free path of Cu [23].

Table 1. Comparison between the parameters of Cu, SWCNT and MWCNT [23]

	Copper	SWCNT	MWCNT
Ampacity (A/cm^2)	10^7	$>10^9$	$>10^9$
Melting Point (C)	1083	3527	3527
Tensile Strength (GPa)	0.22	22.2±2.2	11-63
Thermal Conductivity ($\times10^3$ W/m K)	0.385	1.75-5.8	3
Temperature Coefficient of Resistance ($\times10^{-3}$/K)	4	<1.1	-1.37
Mean Free Path at Room Temp. (nm)	40	10^3	2.5×10^4

1.3.2 *CNT composites*

The outstanding mechanical, electrical and thermal properties of CNTs have made them among the most promising future-materials in a wide range of applications. Number of publications and patents on CNT- and graphene-based materials has grown rather substantially during the last decade (Fig. 5) due to the ever-growing market demand for their properties. Scaling-up and commercialization has also grown significantly since 2006, which is a solid

indication of their promise. Due to the very soft structure of CNTs, they are preferably mixed with different materials in a matrix to facilitate their production. Most of CNTs production is used in bulk composite materials and thin films such that CNTs are unorganized and not self-aligned. Although, alignment and organization of these CNTs in the composite will enhance the functionality and the performance of the composite such as conductivity, Young's modulus and tensile strength [27]. However, commercialization is yet challenging due to the lack systematic fabrication techniques.

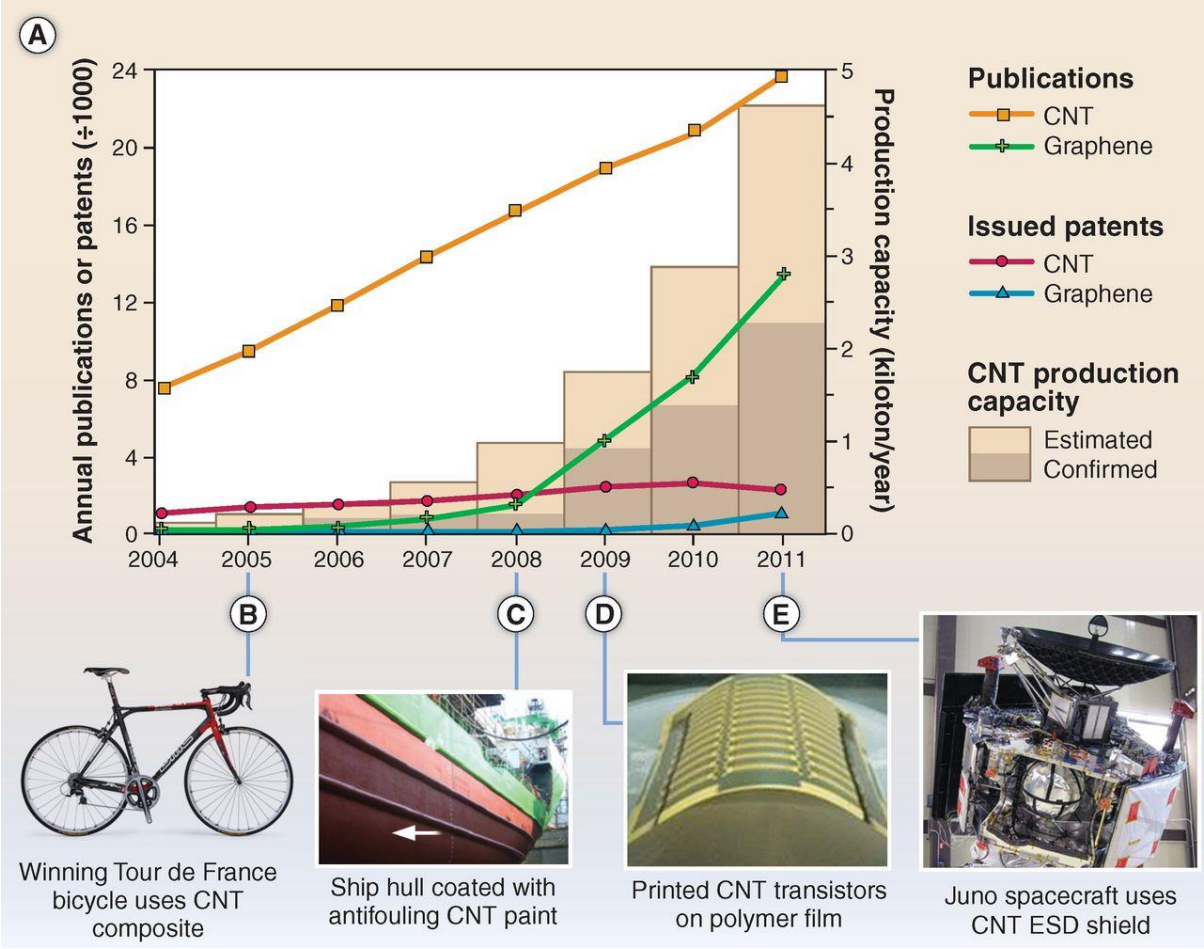

Fig. 5. Research and commercialization trends of CNT and graphene (A) Journal publications and issued worldwide patents per year, along with estimated annual production capacity (B to E) Selected CNT-related products: composite bicycle frame [Photo courtesy of BMC Switzerland AG], antifouling coatings [Courtesy of NanoCyl], printed electronics [Photo

courtesy of NEC Corporation; unauthorized use not permitted]; and electrostatic discharge shielding [Photo courtesy of NanoComp Technologies, Incorporated]. [Figure courtesy of [22]]

There are several applications of CNT-composites. CNT powders mixed with polymers or precursor resins are used for load-bearing applications because of the high toughness, strength and stiffness [28]. Addition of 1 wt % MWCNT to epoxy resin increases fracture toughness and stiffness by 23 and 6%, respectively [29]. Moreover, the stick-slip behavior of CNT/CNT and CNT/polymer enhances the damping properties and can be used in sporting products such as baseball bats, tennis racquets and bicycle frames [30]. CNT resins are used to enhance carbon fiber composites [28,31]. For example, his technology is utilized in the manufacture of strong, lightweight wind turbine blades and hulls for maritime security boats by *Zyvex Technologies*.

The addition of CNTs to metals has also increased tensile strength and Young's modulus [32]. Applications of CNT/metal composites can be found in aerospace and automotive structures. Commercial MWCNT/Al composites obtain strengths higher stainless steel (0.7 to 1 GPa) at one-third the density (2.6 $g.cm^{-3}$).

Most of the commercialized applications are in bulk size, where CNTs are randomly organized in the composite. These CNT composites have not yet achieved properties near those of individual CNTs. Many factors such as orientation, chirality and number of walls dictate the mechanical and electrical properties. Furthermore, their effect becomes very significant for applications at smaller scales such as nano- and microelectronics. Therefore, Researchers have started to study CNT-composites at different scales (nano through micro) using different techniques. For nanoscale investigations, it becomes so challenging to conduct tests experimentally because of the very small size and time scales of the tests (nanometer and

picoseconds, respectively). Therefore, simulation and modeling become a very effective way to preliminary investigate these materials.

1.3.2.1 *Literature on Simulation and Modeling*

Due to the mentioned difficulties at the nano- and microscales, simulation can be used as guiding tool to provide insights on mechanical integrity and long term reliability of these CNT-composites. The forces at the interface of CNTs and different materials are governed by molecular interactions. Therefore, regular continuum-level simulations, such as finite element analysis, are not capable of modeling this interface behavior. Thereupon, researchers have used and have investigated several simulation techniques at the atomic level. These techniques include molecular mechanics, density function theory, ab initio and molecular dynamics. Key properties such as cohesive interfacial properties are determined use these atomistic level simulations. Extracted parameters from the atomistic models are then used in a continuum model such as finite element of constitutive model. This approach is called multiscale modeling, where different scales are linked together using distinct techniques. The literature includes investigation of the interfacial properties of CNTs and polymer, non-metals and metals. Also, multiscale modeling is conducted on these composites in order to understand the behavior at larger scales.

1.3.2.1.1 Polymers and Non-metals

The interface between CNT and polymers has been studied widely by many research groups due to the promise of CNT/polymer composites in the mechanical and structural applications. Tsuda et al. [33] experimentally evaluated the interfacial shear strength (τ_{max}) of CNT/PEEK (poly-ether-ether-ketone) composite. An individual multi walled CNT (MWCNT)

was pulled out from the composite using a testing system installed inside a scanning electron microscope (SEM). The pull-out force was measured by the deformation of an atomic force microscope (AFM) cantilever. τ_{max} of MWNT/PEEK composite was measured as 3.5–7 MPa. However, when heat treatment was applied to the specimen, shear strength (τ_{max}) increased to 6-14 MPa as a result of interfacial bonds' recovery. The results agree with the macroscopic stress-strain behavior of MWNT/PEEK. The experiments have shown that vdW forces are dominant in the interface. The authors have found that the reported results of τ_{max} from molecular dynamics (MD) simulations are small (<10 MPA) when considering vdW interactions only. Wernik et al. [34] investigated the interfacial properties of CNT reinforced polymers through atomistic-based continuum model by simulating CNT pull-out experiment. The interface between CNT and polymer matrix was constituted by Lennard Jones constitutive relation that represents vdW interactions. Although, pull-out force is not affected by CNT's embedded length, the authors claimed the τ_{max} decay significantly with the embedded length. They calculated τ_{max} by dividing maximum force by interfacial area of various CNT lengths. In the same way, increasing CNT diameters increases pull-out forces but decreases τ_{max}. Their study also illustrates the effect of different CNT capping scenarios showing that incorporating an end cap in the simulation yields high initial pull-out peaks that better correlate with experimental findings. Li et al. [35] carried out a series of pull-out simulations of CNT to investigate the interfacial properties between CNT and polymer matrix with only consideration of van der Waals (vdW) interaction. They also derived an expression to determine the interfacial shear stress. Kim et al. [36] examined the effect of interfacial bonding between CNT and Si on the mechanical properties. Only vdW interactions are considered in C-Si and are represented by Lennard Jones relationship. They observed that Young's modulus, maximum

tensile strength and toughness are increased steadily with increasing Si-C bonding strength (ε, the potential well depth in Lennard Jones constitutive relationship).

In order to establish a realistic model on a hybrid structure like CNT-composite, a complete characterization of the interface is needed. Vast research has been done on the cohesive zone model (CZM) of CNTs with different materials, mostly polymers. Jiang et al. [37], analytically, established the cohesive law for interfaces between a CNT and polymer that are characterized by the vdW force. For a CNT in an infinite polymer, tensile cohesive stress depends only on the normal displacement and the shear cohesive stress vanishes. On the other hand, in the same study, for a CNT in a finite polymer matrix, the shear cohesive stress depends on both opening and sliding displacements, i.e., the tension/shear coupling and the tensile cohesive stress remains the same. The simple, analytical expressions of the cohesive law are useful to study the interaction between CNT and polymer, such as in CNT-reinforced composites. The effect of polymer surface roughness on the cohesive law is also studied and shear cohesive stress was found to vanish for a wavy polymer surface and flat graphene. Tan et al. [38] incorporated the nonlinear cohesive law derived from the weak vdW force for carbon nanotube/polymer interfaces in a micromechanics model in order to study CNT-reinforced composites. Although CNTs can improve the mechanical behavior of composite at the small strain, such improvement disappears at relatively large strain because the completely de-bonded CNTs may weaken the composite as they behave like voids in the matrix. They proposed that the increase of interface adhesion between CNTs and polymer matrix may significantly improve the composite behavior at the large strain. Jiang et al. [39] used an inverse iterative Finite Element approach to estimate the CZM parameters viz., interfacial strength and interfacial fracture energy. A microstructure-level 3D FE model for nano-

indentation simulation has been developed where the composite microstructure is modeled using three distinct phases, viz., the CNT, the polymer, and the interface. The unknown CZM parameters of the interface are then determined by minimizing the root mean square (RMS) error between the simulated and the experimental nano-indentation load–displacement curves for a 2 wt. % CNT–polyvinyl alcohol (PVA) composite sample at room temperature. Namilae and Chandra [40] developed a hierarchical multiscale methodology linking MD and FEM in order to study the atomic scale interface effects on composite behavior of CNT/fiber matrix . Pull-out simulation has been done by MD. Then, the results of the pull-out simulations are used to extract the parameters of CZM. These parameters are then used in FE in order to study the macroscopic mechanical response of the composite. This developed methodology is employed to study the effect of interface strength on stiffness of CNT-based composites. It is found that interfaces significantly alter the elastic response of CNT-based composites. Representative volume element (RVE) was also used for the mechanical behavior evaluation of the CNT/polymer composites [41–43]. RVE combines nano- and continuum-level mechanics in order to link the nano- and the meso-scales. Nano-mechanics was used to simulate the behaviors of the individual CNT and the matrix, respectively. Then, FE method or continuum constitutive relations were used to build the RVE.

1.3.2.1.2 Metals

Maiti and Ricca [44] have theoretically investigated the wetting properties of CNTs to different metals e.g. Au, Pt and Pd with different configurations using density function theory. Nemec et al. [45] applied *ab initio* density function theory to distinguish between poor and strong contacts of metals to CNTs and observed superiority of Pd to Ti in metal-nanotube

hybridization. They have also suggested that the optimum metal-nanotube contact combines a weak hybridization with a large contact length of few hundred nanometers between the metal and the nanotube. Banhart [46] has reviewed the interaction between metals and CNTs in different material systems. The interface reaction between the CNTs and metallic materials are classified into side and end contact interactions. It is assumed that, for weakly bonded metal to CNT contacts, only van der Waals (vdW) interactions exist and covalent bonds are absent. Toprak and Bayazitoglu [47] created MD simulation to predict the thermal conductivity of a single wall CNT filled with a Cu nanowire for different lengths with different temperatures at the two ends; 320° K and 280° K. It was found that the thermal conductivity of the CNT/Cu nanowire is higher than that of a pure CNT and estimated to be lower than that of a pure Cu nanowire. Hartmann et al. [48,49] performed a tensile test and pull-out test of a single walled CNT embedded inside gold using MD simulation. They reported the influence of the embedded length and the temperature on the pull-out force. The results show that embedded length has minor effect. The temperature has a small effect on the maximum pull-out force as well.

Many studies have investigated the interaction between different materials and CNTs. Studies in the area of interaction between Cu and CNTs are scarce. However, Cu composites with CNTs have promising mechanical and electrical properties that make them potentially suitable for many micro/nano-electronic applications e.g. TSVs, interconnects, transistors, etc. Therefore, a study of the mechanical interactions between the CNTs and the metallic material typically used for interconnects such as Cu is of paramount importance. MD simulation is a feasible and reliable methodology to preliminarily investigate the mechanical behavior of novel materials. Therefore, in this MD simulation is used to explore the cohesive interfacial

strength and behavior of metallic CNTs at the interface of Cu. The interface properties extracted are be beneficial for the multiscale modeling of the hybrid or composite material made using CNTs and Cu.

1.3.2.2 *Literature on experimental fabrication*

In general, carbon nanostructures, have been investigated widely as candidate materials for next-generation interconnects due to their promising thermal, mechanical and electrical properties [23] that are believed to increase the interconnects' reliability, performance and functionality. These nanostructures been investigated to replace the materials of some microelectronics' key components such as transistors [18–20] and interconnects [50–53]. CNTs are among those carbon nanostructures. Researchers have investigated adopting CNTs in TSV fabrication. For the fabrication of CNT-TSV, MWCNT are studied, since as-gown MWCNTs are all conducting whereas there is not a specific technique to control the conductivity of as-grown SWCNTs because the mixture of as-grown SWCNTs yields 2/3 semiconducting and 1/3 conducting SWCNTs [24]. One approach that has been studied extensively is filling TSVs with CNTs [11,54,55]; however, CNT-TSVs have not shown improved electrical performance compared to Cu-TSV due to several issues such as the low density of CNT bundles that decreases the conductivity, the increased resistivity between the CNT bundle and the other metallic contacts and the low mechanical stability of CNT bundles. In order to overcome these issues, another proposed approach is to fill the TSVs with CNTs, densify them and then Cu is electroplated around the densified CNT bundle to fill the gap between the CNT bundle and the TSV wall [56,57]. However, the resulted TSV did not show improved performance compared to Cu-TSVs due to the obtained high resistivity. One of the

factors that contribute to the high resistivity is the low composite density. Recent experimental characterization of CNT/Cu-composite has shown that the ampacity of CNT/Cu is two orders higher than that of Cu, and the same conductivity as Cu [15], which means that the novel material would be able to endure higher current density without failure at further miniaturized scales. In other words, CNT/Cu-TSV has a promising potential to replace Cu-TSV in next-generation microelectronics. Fabrication cost is a main concern in the industry. Therefore, a systematic scale-up fabrication technique should be investigated as well.

1.4 Dissertation Objectives

Due to the novelty of the proposed TSV hybrid material, very little information is available on the mechanical interfacial properties of CNT/Cu matrix. Mechanical integrity and interfacial properties dictate long term behavior and reliability of these interconnects which are critical factors in adapting the new technology by semiconductor manufacturers [34,37,58]. TSVs or other interconnects in general are prone to failure due to thermal and mechanical stresses. Thus, the mechanical behavior of the TSV has to be studied under different conditions of loading; bending and thermal lading. The adhesion between CNT and Cu at the interface has to be evaluated as well. Furthermore, a scale-up fabrication technique of the novel CNT/Cu-TSV needs to be proposed.

1.5 Dissertation Approach

The core of this dissertation is the investigation of the novel CNT/Cu-TSV from the mechanical aspect and the proposal of a systematic fabrication technique. Information about the mechanical properties of CNT/Cu-composite is not thoroughly discussed in the literature. Therefore, simulation and modeling is employed to preliminary investigate the mechanical

properties of the novel composite material. Moreover, a systematic fabrication technique is to be investigated.

1.5.1 *Simulation and Modeling*

There is not enough information about CNT/Cu interfacial mechanical properties because the lack of their mechanical application. Scientists have used many ways to understand the interfacial properties between CNTs and some other materials composites. One of the most reliable ways is MD. MD simulation is a good way to predict some properties at the nanoscale since experiments at this scale are extremely challenging. Pull-out tests is one of the ways to evaluate the interfacial strength of the interface. As mentioned in the literature review, MD simulation can be used to evaluate the interfacial strength of CNT composites by applying a series of pull-out tests considering vdW interactions [35,48,49]. In the same manner, pull-out tests are conducted on different case studies of SWCNTs at the interface with Cu in order to study the effect of different factors on the interfacial strength including number of CNTs, length, point of force application, multi-layer and boundary conditions. Then, CNT/Cu interfacial shear strength can be predicted. The test is conducted by applying displacement controlled loading as shown in Fig. 6-c.

Interfacial properties in the direction normal to the interface have to be also evaluated in order to provide a complete understanding of the interfacial properties. Normal CZM gives a complete insight on the interfacial behavior in the normal direction to the interface. CZM of CNT/polymer composites has been evaluated by applying a series of pull-out tests in axial and tangential directions by MD simulations [40,58]. After load is applied, CZM can be extracted. CZM is a relationship between stress (σ) and separations (δ) in Angstroms. The key

parameters of CZM are the maximum stress (σ_{max}), separation at σ_{max} ($\overline{\delta_n}$) and separation when σ_{max} = 0 (δ_{n0}). Displacement controlled loading is applied in a direction normal to the CNTs axis as shown in Fig. 6-d. The effects of the number of walls and the temperatures on the CZM are important to be studied.

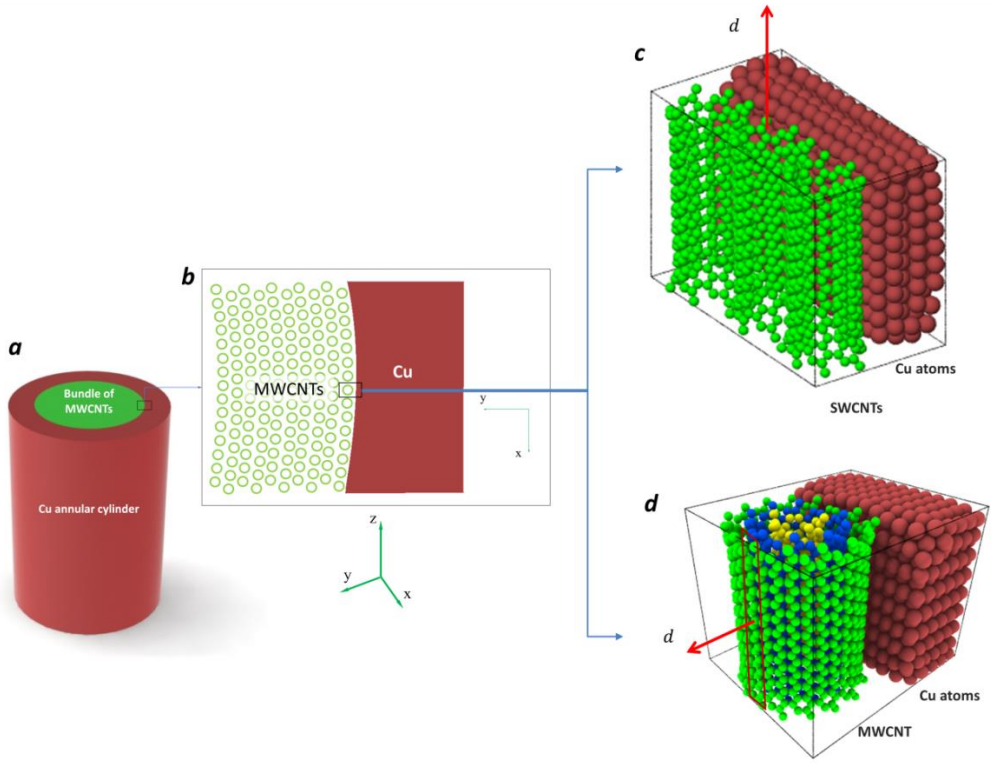

Fig. 6: Schematic of the simulation: [a] cylindrical TSV; [b] top view of the interface ; [c] pull-out test; [d] normal CZM model evaluation

Stress-strain behavior and coefficient of thermal expansion (CTE) of CNTs vary with the number of walls and the chirality of CNTs. Therefore. They are evaluated by using MD simulation on the selected MWCNT under study. Stress-strain behavior is evaluated by applying displacement controlled loading on the upper end of the CNT strand while the other

end is fixed. CTE is conducted by applying temperature on the selected CNT. Temperature effect on CTE is to be evaluated as well.

Information gathered from the MD simulation can be then utilized at larger scale to evaluate the mechanical behavior of the CNT/Cu hybrid material. In the current study, Multiscale modelling is used to bridge nano- through micro-scale (Fig. 7). First, MD simulation is used to evaluate both the interfacial shear strength and interfacial normal strength at the nanoscale (atomic level). Consequently cohesive zone model was developed that fit the interfacial behavior at interface of Cu/CNT. This CZM model is then used to define the material properties for the contact elements in the FEM at the micro-scale (continuum level).

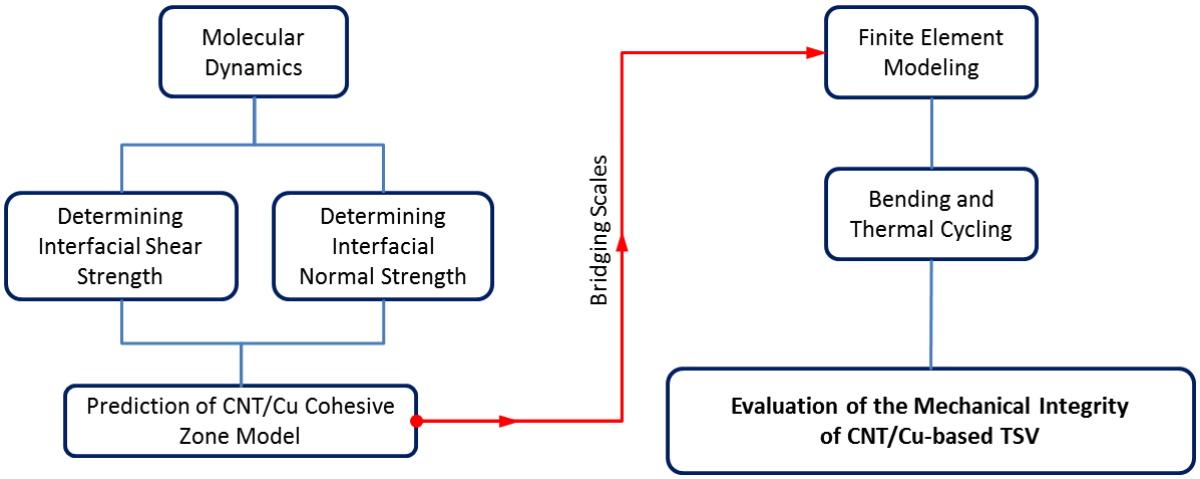

Fig. 7: Schematic of multiscale modeling steps

At the continuum level, the interface between the Cu and CNT can be modeled in two manners. One unrealistic model would be to assume a perfect interface and complete adhesion between CNT and Cu. Another arbitrary technique would be to assume some sort of contact element at the interface and arbitrarily assume some contact behavior. The approach presented here fills this gap, by providing a realistic MD model at the interface and obtaining the interface properties that otherwise had to be guessed or arbitrarily assigned. This combined

multiscale modeling approach is then used to evaluate the mechanical integrity of these interconnects in a realistic package under thermo-mechanical and mechanical cyclic load. Furthermore, fatigue life can be predicted. CNT/Cu-TSV is compared to Cu-TSV in order to evaluate the extent of improvement. The adopted approach is believed to give a sufficient preliminary understanding of the mechanical behavior of the novel CNT/Cu composite material under bending and thermal cycling, since there is not enough information provided in the literature; either theoretical or experimental.

1.5.2 *Fabrication*

Due to the novelty of the CNT/Cu-composite material, there is not a scale-up fabrication technique. The proposed process starts with photolithography (Fig. 8-a) to create array of circles on the photoresist. Deep etching of the Si wafers is done to produce high-aspect-ratio-vias (≥ 4) using deep ion reactive etching (DRIE) as seen in Fig. 8-b. Then, a dielectric layer of SiO_2 is diffused on the walls of the blind vias (Fig. 8-c). A catalyst layer, e.g. Fe, over a buffer layer of Al_2O_3 is deposited using electron beam evaporation (Fig. 8-c). Vertically aligned CNTs are then grown using thermal chemical vapor deposition (CVD) (Fig. 8-d). Then, Cu is deposited by electroplating (Fig. 8-e). While conducting the current research research, results of densifying CNTs and encasing them with Cu were published and did not show improved performance to Cu [57]. Therefore, instead, Cu is electroplated to fill the interstitial spaces between the CNT strands and between the CNT and the wall of the via. CNT/Cu-composite on the surface of the wafer are etched away to leave only the CNT bundles inside the vias (Fig. 8-f). This proposed fabrication process is placed under scrutiny in this study because it is subject to alteration due to the possibility of failure to meet any of the

sought objectives e.g. growing CNTs inside the vias, high density CNTs, well aligned CNTs, electroplating CNTs with Cu and good adhesion between CNTs and the substrate.

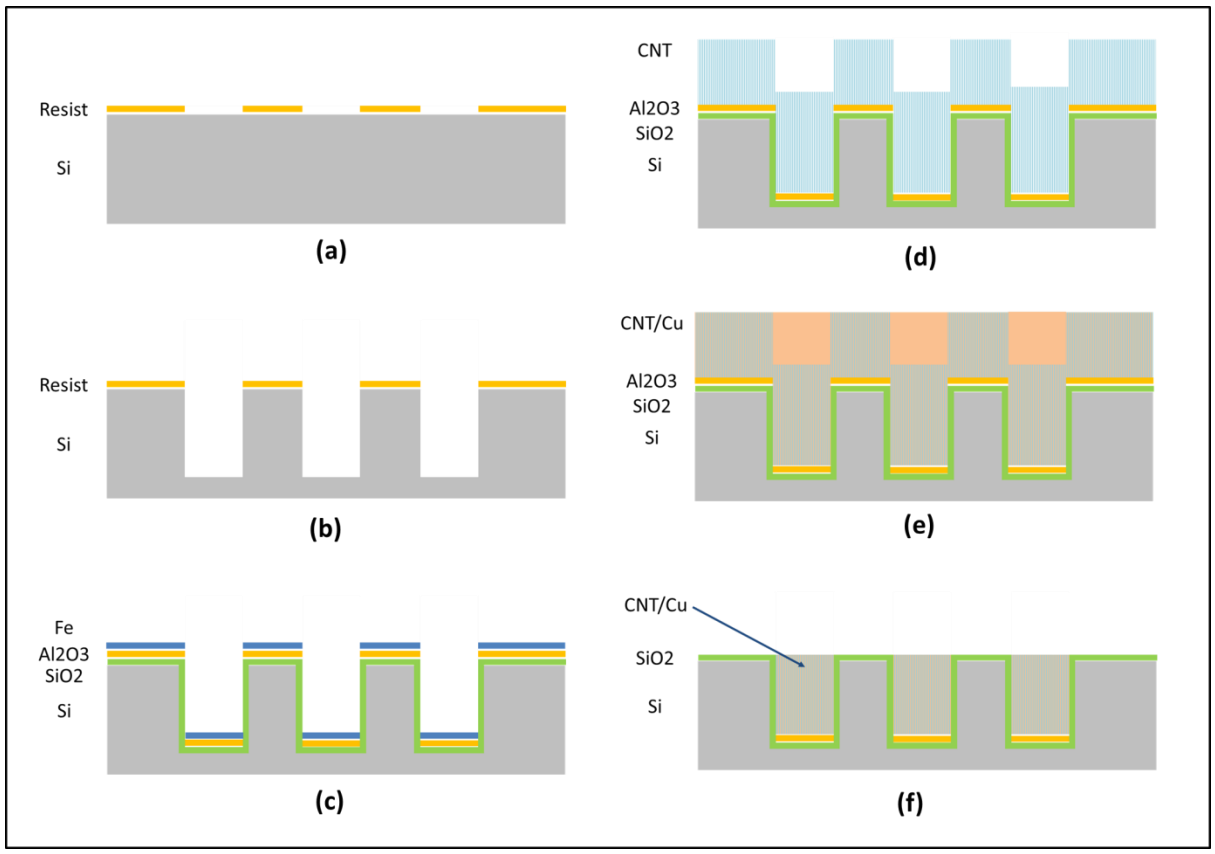

Fig. 8: Proposed fabrication process

CHAPTER 2. SIMULATION AND MODELING

2.1 Molecular Dynamics Simulation of the Mechanical Behavior

Several case studies of CNT are simulated to evaluate the mechanical behavior of CNT/Cu-interface and CNT at the atomic level. Large-scale Atomic/Molecular Massively Parallel Simulator (LAMMPS) code [59] is used for MD simulations. Cases of SWCNTs at the interface with Cu are simulated to study the effect of different arrangements of SWCNT and conditions on the interfacial strength. Also, cases of MWCNT at the interface with Cu are studied in order to estimate the effect of number of walls and temperature on the interfacial strength. Moreover, stress-strain behavior and CTE are evaluated and the temperature effect on CTE is also investigates.

2.1.1 *Case Studies with SWCNT*

Different arrangements or case studies of SWCNT/Cu-interface are conducted in order to study different effects such as the effect of number of SWCNT strands, the effect of multi-layers, the effect of boundary conditions and the effect of length. LAMMPS is used to simulate force-displacement relations in a simple model that consists of SWCNTs interfaced with a Cu slab. The current study focuses on TSVs. Fig. 9 shows a cylindrical TSV made of vertically

oriented CNTs embedded inside an annular cylinder of Cu. A bundle of embedded CNTs contains thousands of them, which makes it challenging and time consuming to model by MD. To make the model computationally feasible, only a few strands of CNT have been modeled as shown in Fig. 9. For each case study, displacement controlled loading has been applied to pull the CNTs out of the Cu slab. The resulted force-displacement curves show the interfacial strength. More details on the atomistic simulation are included in APPENDIX A.

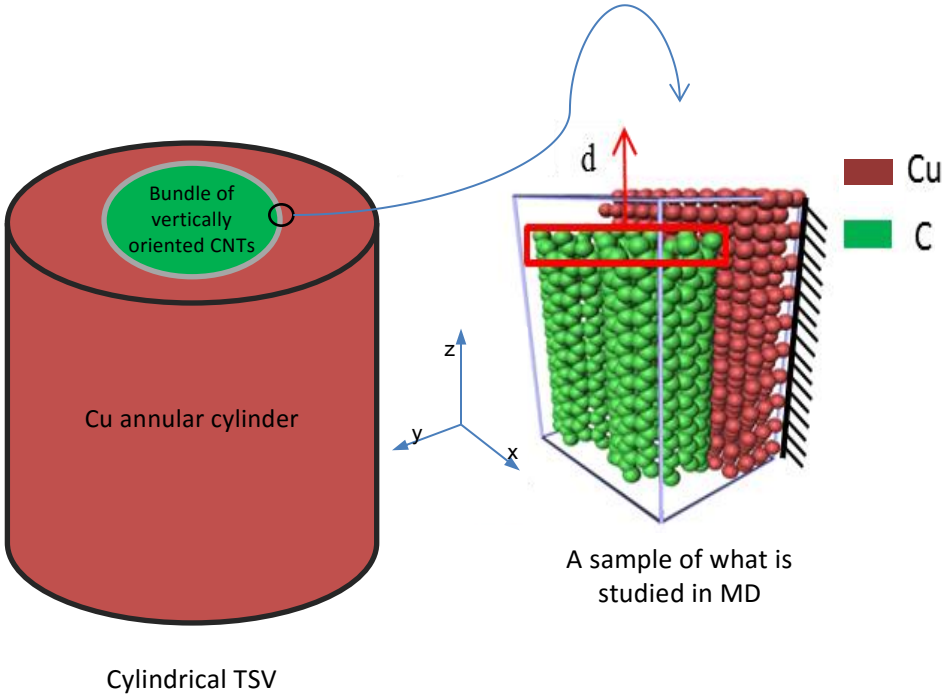

Fig. 9. Schematic of the TSV and a sample of the MD structure

The structure is built by Atomic Simulation Environment ASE [60] using Python coding software. For the current case, a few CNTs of chirality (7,7) (armchair electrically conductive CNT) and a length of 26 A^{o} have been modeled. Cu slab is assumed to be FCC (100) in the direction of CNT axis. Embedded Atom Method potential (EAM) [61] is used for interatomic potential between Cu atoms. Adaptive Intermolecular Reactive Empirical Bond Order (AIREBO) [16, 17] interatomic potential is used for carbon atoms as [18–20]. (AIREBO)

model is a function to calculate the potential energy of covalent bonds, interatomic force and the long-ranged interaction between atoms. For the interatomic potential between Cu and Carbon atoms, only vdW potential occurs and that has been implemented in LAMMPS by the use of Lennard Jones interatomic potential [11 &21]. The Lennard Jones parameters used for C-Cu interactions are (σ= 3.088 A^o and ε = 0.025 eV) where σ is the finite distance and ε is the depth of the potential well. For the inter-tube (CNT-CNT) potential only vdW interaction is considered as in [22–24]. Lennard Jones parameters used for CNT-CNT interaction are (σ = 3.4 A^o and ε = 0.00284 eV).

The energy of the structure was first minimized using conjugate gradient algorithm [12 & 20]. The minimization was done to place the atoms in more stable positions where it is geometrically optimized. The system was then heated up to the desired temperature using NPT ensemble where N, the number of atoms, P, the pressure of the system and T, the temperature, are kept constant. The pressure was kept at zero to mimic the experimental condition of an AFM experiment conducted at vacuum pressure. The system is heated to 1^o K for 50 ps as an arbitrary value because it was reported that temperature has little effect on the pull-out force [12]. NPT equilibration process is followed by NVE and Berendsen thermostat [70] integrations for 50 ps where V is the volume and E is the total energy which were kept constant. Berendsen thermostat keeps the temperature constant at 1^o K. Displacement was applied on Carbon atoms using discrete displacements in a displacement controlled manner. The two uppermost rings of the CNT were subjected to discrete displacements of 0.1 A^o until the CNT strand is pulled out completely. The system is equilibrated using NVE ensemble and Berendsen thermostat for 10 ps after each step in order to avoid energy build-up and destabilization. Both NVT and NVE combined with Berendsen thermostat are used in literature

to create a thermostat in order to keep the temperature constant and perform time integration. NVE and Berendsen thermostat function as NVT equilibration to converge to the environment temperature after applying the displacement [12, 26, & 27]. NVT ensemble performs both Nose-Hoover thermostating and time integration while Berendsen thermostat performs only Nose-Hoover thermostating. Therefore, another ensemble is necessitated to perform time integration, which is NVE. When combined with Berendsen thermostat, NVE does not keep the energy constant and the system exchanges energy with the environment to bring the temperature down to 1°K. To make sure that the effect are the same a model was run with NVT and NVE combined with Berendsen thermostat. As shown in Fig. 10 the results are identical.

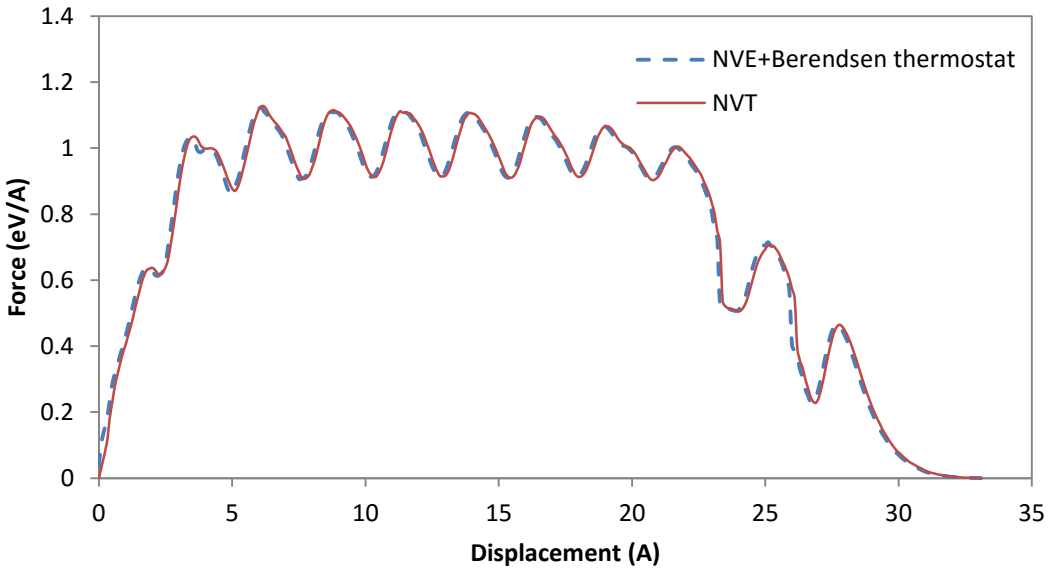

Fig. 10. NVT vs. (NVE+Berendsen thermostat)

2.1.2 *Case Studies with MWCNT*

MWCNT at the interface with Cu is also studied. In these case studies CZM is evaluated by applying a series of pull-out tests in both axial and tangential directions. Also the effect of

number of walls and temperature are also investigated. LAMMPS code was employed to simulate the stress-displacement relations in a simple model that consists of MWCNT interfaced with a Cu slab. Fig. 11-a shows a cylindrical TSV made of vertically oriented MWCNTs embedded inside an annular cylinder of Cu. A bundle of embedded MWCNTs contains thousands of them (Fig. 11-b), making it practically impossible to model the whole bundle and copper cylinder. In order to make the model computationally feasible only a single strand of the CNT is modeled at the interface of the copper (Fig. 11-c). Since the bundle consist of many CNTs that are periodically arranged at the interface of copper, it is reasonable to model only one strand and assume periodicity in x directions, as shown in Fig. 11-b. Thus, just a single unit cell is modeled as shown in Fig. 11-c. It is also assumed that the CNTs are long enough and behave consistent in z direction. Therefore, the same assumption is made in z direction. Displacement controlled loading (shown by "d" arrow in Fig. 11-c) has been applied to pull the MWCNT out of the Cu slab in a direction normal to the axes of the nanotubes. The resulted stress-displacement curves are obtained and related to available CZMs in literature. More details on the atomistic simulation are included in APPENDIX A.

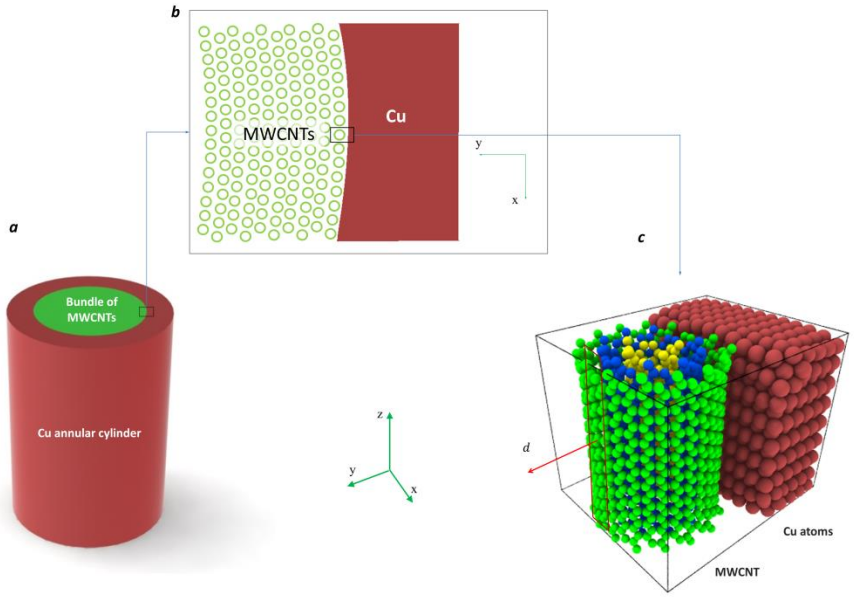

Fig. 11. Schematic of the simulation: [a] cylindrical TSV; [b] top view of the interface; [c] a sample of the Molecular Dynamics structure

The structure is built using ASE [60] using Python coding software. MWCNTs used in this study contain up to 7 walls. Their chiralities are (5,5), (10,10), (15,15), (20,20), (25,25), (30,30) and (35,35), armchair CNTs, and a length of 27 Å have been modeled. Cu slab's thickness in y-direction is 15 A^o and is chosen to be larger than C-Cu cut-off distance which is 7.7 Å (2.5 σ which is the finite distance at which the inter-particle potential is zero [73]) . The length in x-direction ranges from 29 to 50 Å based on the outer diameter of the CNT strand. Cu slab is assumed to be FCC (100) in the direction of CNT axis. Interatomic potentials and parameters of C-Cu and Cu-Cu are the same as the last subsection of the case of SWCNT. For the inter-tube (CNT-CNT) potential only vdW interaction is considered as in [22–24]. LJ parameters used for CNT-CNT interaction are (σ = 3.4 Å and ε = 0.00284 eV) [22–24].

After building the structure of the atoms, the system was then equilibrated at the desired temperature 1^{o} K for 50 to 250 ps, dependent on the simulation size, using Langevin thermostat accompanied with NVE ensemble to perform time integration and update the positions and velocities of the atoms where N, the number of atoms, V, the volume of the system and E, the Energy, are kept constant. Displacement was applied on Carbon atoms using discrete displacements in a displacement controlled manner. As depicted in Fig. 11, the farthest column of atoms in y-direction of the MWCNT was subjected to discrete displacements of 0.1 A^{o} until the MWCNT strand is completely pulled out. The system is equilibrated using NVE ensemble and Langevin thermostat for 10 ps after each loading step in order to avoid energy build-up and destabilization.

Stress calculation in MD simulation is discussed here because it is a matter of controversy. Atomic level stress, aka virial stress, is developed from the virial theorem of Clausius [74] and Maxwell [75] by Swenson [76] and Tsai [77] and it is given as follows,

$$\sigma_{ij} = \frac{1}{V}\sum_{\alpha \in V}\left[\frac{1}{2}\sum_{\beta=1}^{N}\left(r_i^{\beta} - r_i^{\alpha}\right) f_j^{\alpha\beta} - m^{\alpha} v_i^{\alpha} v_j^{\alpha}\right] \qquad \text{Eq. 1}$$

where r indicates the position and subscripts i and j are the direction indices and take the values $x, y\ and\ z$, α and β are atoms in the domain, V is the volume of the domain, N number of atoms neighboring atom α, $f_j^{\alpha\beta}$ is the component of the force applied on atom α by atom β, m^{α} is the mass of atom α and v_i^{α} and v_j^{α} are the i^{th} and j^{th} velocity components of atom α respectively. The above expression contains two parts; potential energy part and kinetic energy part.

The controversy was about whether virial stress tensor is equivalent to Cauchy's mechanical stress tensor or not. Costanzo et al. [78,79] derived Cauchy stress from

Lagrangian-based MD method. They have found their derived Cauchy stress does not coincide with virial stress because Cauchy stress has no explicit dependence on velocity terms while virial stress does. Knowing that the involved instantaneous velocities in the above expression of the virial stress are due to thermal fluctuation, virial and Cauchy stresses only coincide at absolute zero temperature because the velocity term vanishes in the virial stress expression. Costanzo et al. also discussed the assumptions under which both stresses can be said to have the same meaning. They are only equivalent if they are time averaged for all times.Zhou [80] and Shen [81] have another opinion about the relationship between virial and Cauchy stress. They derived their own stress definition and proved through examples that virial stress is equivalent to Cauchy stress when the velocity term in virial stress is ignored. Sun, Tschopp and Yang [82–84] and others have used Zhou's interpretation to justify using only the potential part of the virial stress. This point of view contradicts with the opinon of Subramaniyan at al. [85]. In that study, they have proven through some examples that the kinetic energy term that contains velocities should not be ignored In the same time ,Costanzo , Subramaniyan and Gao [78,85,86] also mentioned that the kinetic part in the virial stress in unnecessary when Lagrangian frame of reference is considered and velocity terms vanish. Lagrangian frame is implied when atoms do not cross the periodic boundaries of the simulation box.

In the current work, simulation box is large enough that atoms do not cross the periodic boundary conditions. Consequently, considering the later point of view, Lagrangian frame of reference is implied and kinetic part vanishes from Eq. 1. Thus, the virial stress will be given as

$$\sigma_{ij} = \frac{1}{V}\sum_{\alpha \in V}\left[\frac{1}{2}\sum_{\beta=1}^{N}\left(r_i^{\beta} - r_i^{\alpha}\right) f_j^{\alpha\beta}\right] \qquad \text{Eq. 2}$$

which agrees with the point of view of Zhou and the others.

2.2 Multiscale Modeling of Package

Multiscale modeling has been used extensively to evaluate the mechanical behavior of the CNT/polymer composites. Some researchers studied CNT/polymer interfaces by developing a hierarchical multiscale methodology linking MD simulations and the FE method through atomically determined CZM [40,58]. In this study multiscale modelling is used to bridge nano- through micro-scale (Fig. 7). First, MD simulation is used to evaluate both the interfacial shear strength and interfacial normal strength at the nanoscale (atomic level). MD simulation has been used in many cases to predict the interfacial shear strength and to evaluate the mechanical behavior at the interface between CNT and different materials, mostly polymers, by conducting pull-out tests in a the tangential direction to the interface [34,36,48,87]. It also has been used to predict the interfacial normal strength and the behavior by applying pull-out tests in the normal direction to the interface [40,58]. Consequently, CZM is developed that fit the interfacial behavior at interface of Cu/CNT in both directions; tangential and normal. This CZM model is then used to define the material properties for the contact elements in the FE modeling at the micro-scale (continuum level).

At the continuum level, the interface between the Cu and CNT can be modeled in two manners. One unrealistic model would be to assume a perfect interface and complete adhesion between CNT and Cu. Another arbitrary technique would be to assume some sort of contact element at the interface and arbitrarily assume some contact behavior. The approach presented here fills this gap, by providing a realistic MD model at the interface and obtaining the interface properties that otherwise had to be guessed or arbitrarily assigned. This combined multiscale modeling approach is then used to evaluate the mechanical integrity of these

interconnects in a realistic package under mechanical and thermal cyclic loading. Thus, the adopted approach is believed to provide a sufficient preliminary understanding of the interfacial properties of the novel CNT/Cu composite material at the atomic level and also the mechanical behavior of the CNT/Cu-TSV at the micro level under the described loading conditions.

2.2.1 *Cohesive Zone Model Evaluation*

CZM depends on the nature of CNT. It changes with number of walls and dimensions of CNT. Therefore, in order to provide a realistic model that adequately represents the CNT/Cu-TSV, CZM parameters are extracted for a selected MWCNT that has already found in the transmission electron microscope (TEM) imaging of the grown CNTs during the fabrication process as shown in Fig. 12

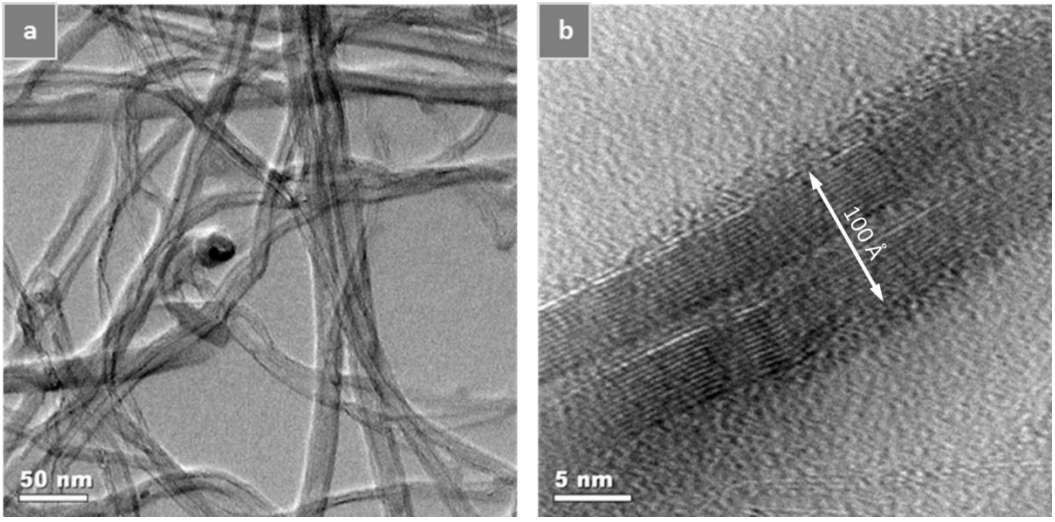

Fig. 12. [a] group of grown MWCNTs [b] sample of the studied MWCNT

Force- and stress-displacement behaviors of MWCNT/Cu interface are simulated by MD using LAMMPS code. A cylindrical representation of a single TSV made of vertically aligned

MWCNTs embedded inside an annular cylinder of Cu is shown in Fig. 13-a. The inner CNT bundle consists of a huge number of MWCNT strands (Fig. 13-b), making it impractical to model the whole bundle along with Cu cylinder. Periodicity is utilized in order to reduce the computation time by only modeling one single strand of MWCNT at the interface of Cy as seen in Fig. 13-c. Periodicity is assumed in x-direction in Fig. 13-c based on the unit cell shown in Fig. 13-b. Also the curvature is considered negligible at the scale of a single MWCNT strand. More details on the atomistic simulation are included in APPENDIX A.

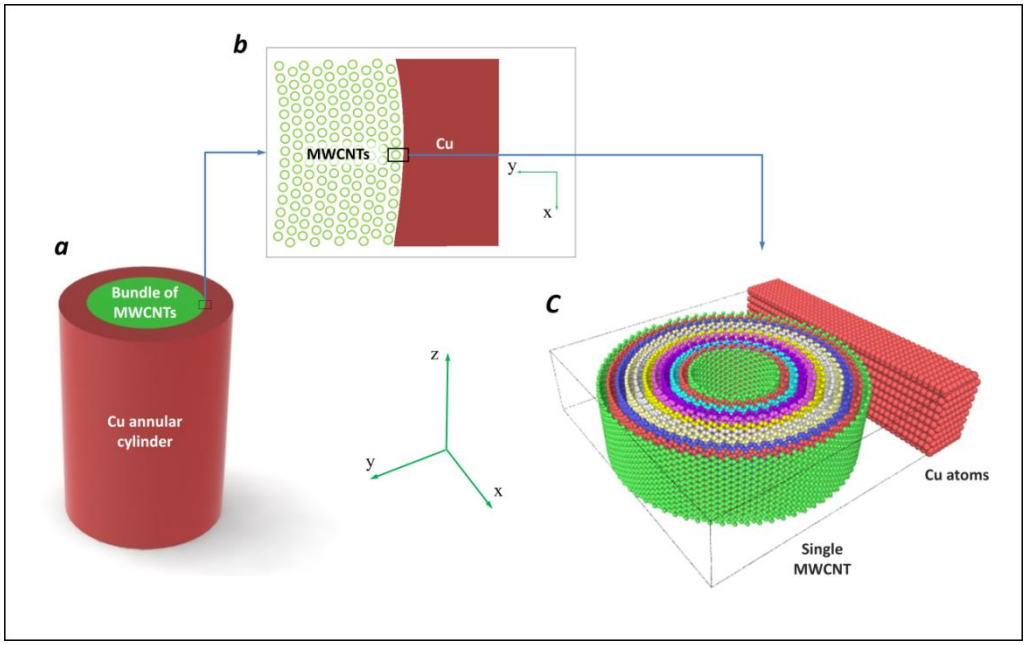

Fig. 13. Schematic of the MD simulation model: [a] cylindrical TSV; [b] top view of MWCNTs/Cu interface; [c] a MD structure used in the current study

Displacement controlled loading has been applied to pull the MWCNT out of the Cu block in two directions as shown in Fig. 14-a and -b; parallel (d_z) and normal (d_y) to the CNT axis. The corresponding force-displacement and stress-displacement curves are then obtained during the simulation of the two loading cases depicted in Fig. 14-a and –b, respectively.

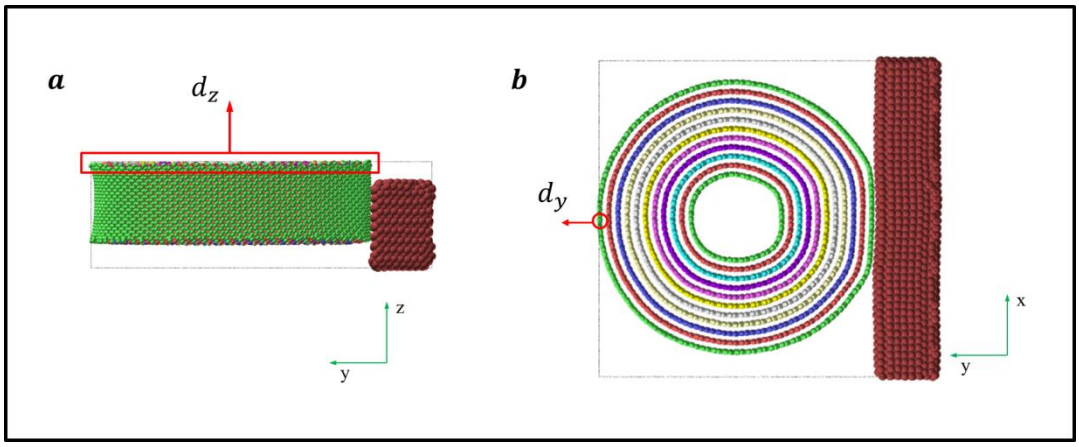

Fig. 14. Loading of the MWCNT: [a] in z-direction; [b] in y-direction

The structure is built using ASE [60] using Python coding software. From Transmission Electron Microscopy (TEM) images of most recently grown MWCNTs for the TSV fabrication within the same group, diameters were found to be around 15 nm and number of walls varies (Fig. 12-a). One sample was taken as a reference for the MD study (Fig. 12-b).

In MD simulation, 11-wall MWCNT strand shown in Fig. 12-b is assumed to have armchair-chirality CNTs and 100 Å diameter. The CNT length is chosen to be 30 Å. CZM parameters are assumed to be unaffected by the CNT's length since it was found in chapter 2 that length does not have a significant effect on the pull-out results [87]. The thickness of the Cu block in y-direction is 15 Å (> C-Cu cut-off distance which is 7.7 Å). Cut-off distance is equal to 2.5 σ, while σ is the finite distance at which the inter-particle potential is zero [73]. The x-direction length is about 110 Å. Cu block is assumed to have FCC crystalline structure with orientation (100) in the CNT's axial direction. For the interatomic potentials between atoms, they are similar the potentials and parameters used in chapters 2 and 3.

After setting up the appropriate potentials and building the atomic structure, the system is equilibrated at the room temperature (298^{o} K) for 200 ps using Langevin thermostat [88]

accompanied with NVE ensemble to conduct time integration and update the atoms' positions and velocities such that N, the number of atoms, V, the volume of the system and E, the energy, are maintained constant. Displacement-controlled loading is applied on Carbon atoms by applying discrete displacements. For the first case (Fig. 14-a), the uppermost two rings in z-direction are subjected to discrete displacements of 0.1 Å until the MWCNT strand is completely pulled out. In the same manner for the second pull-out case (Fig. 14-b) the farthest column of the MWCNT's atoms in y-direction is subjected to the discrete displacement until separation takes place. After each loading step in order to avoid destabilization and energy build-up, the system is equilibrated using NVE ensemble and Langevin thermostat for 10 ps.

2.2.2 *Finite Element Simulation of Package*

In this part, continuum model using FE analysis is employed to investigate the mechanical integrity of the CNT/Cu-TSV by applying bending and thermal loading. These two types of loads are loads that packages that contain these interconnects are subject to during their life cycle. Thermo-mechanical load is induced by mismatch of coefficient of thermal expansion in different package layers and bending is caused by mechanical loads that packages may endure in field or even during fabrication.

2.2.2.1 *Bending Scenario*

In the bending case, the main objective is to obtain insights on mechanical integrity of CNT/Cu contact under bending conditions. Therefore, a single TSV in the middle of a long Si wafer is studied where stresses and strains are maxima during bending (Fig. 15). The Si wafer is chosen long enough so that large bending displacement can be induced without reaching

silicon strength. Three-point bending test is conducted by applying displacement controlled loading as depicted in Fig. 15.

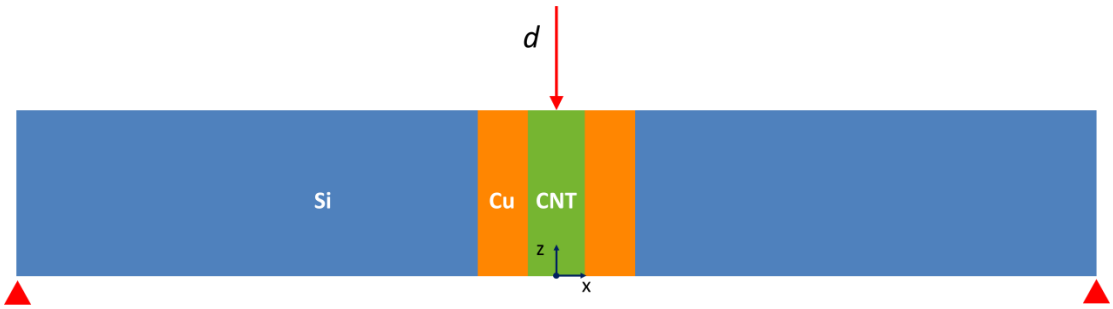

Fig. 15. Schematic of 3-point bending test

ANSYS Mechanical APDL is used for the FE analysis. CNT/Cu-TSV is 25 μm diameter and 100 μm long. CNT bundle is 10 μm diameter. The modeled Si wafer is 1000 μm long and 60 μm thick. Symmetry boundary condition is utilized to reduce computation time as seen in Fig. 16. Material properties used in FE are listed in Table 2. Plastic properties are only considered for Cu since CNT's Yield Strength and Si's Ultimate Tensile Strength (UTS) (100 GPa and 7 GPa, respectively) are very high compared to Cu Yield Strength (172.8 MPa). Furthermore, CZM parameters for CNT/Cu interface extracted from the results of MD simulations in section 2.2.1 are to be used. CZM is implemented through contact elements at the interface of CNT and Cu.

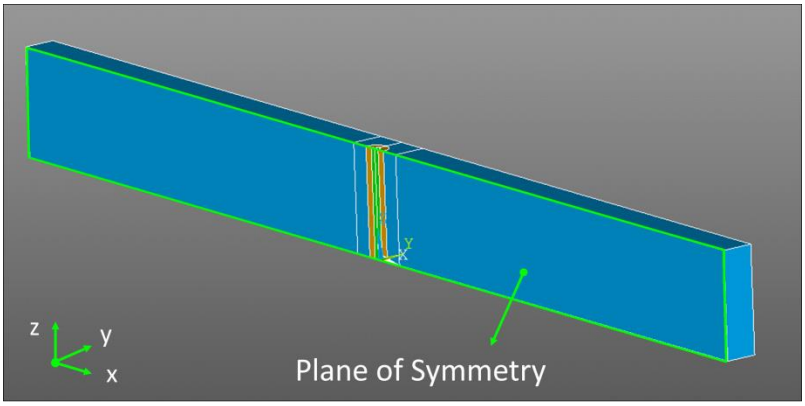

Fig. 16. Schematic of TSV in FE bending case

Table 2: FE material properties: bending loading case [89,90]

Material	Property	Value
Si (Linear Isotropic)	Modulus of Rigidity (E)	191 GPa
	Poisson's Ratio (μ)	0.3
Cu (Bilinear Isotropic)	E	171 GPa
	μ	0.35
	Yield Stress (σ_y)	172.8 MPa
	Tangent Modulus	517.8 MPa
CNT (Linear Isotropic)	E	1 TPa
	μ	0.17

Fig. 17 shows parts of the meshed model. The element type used is SOLID185 for the whole solid block. Contact elements are used to represent the interface between the CNT bundle and Cu material. TARGET170 and CONTA174 elements are used for target (Cu surface) and contact (CNT bundle surface) elements, respectively. Boundary conditions are shown schematically in Fig. 15.

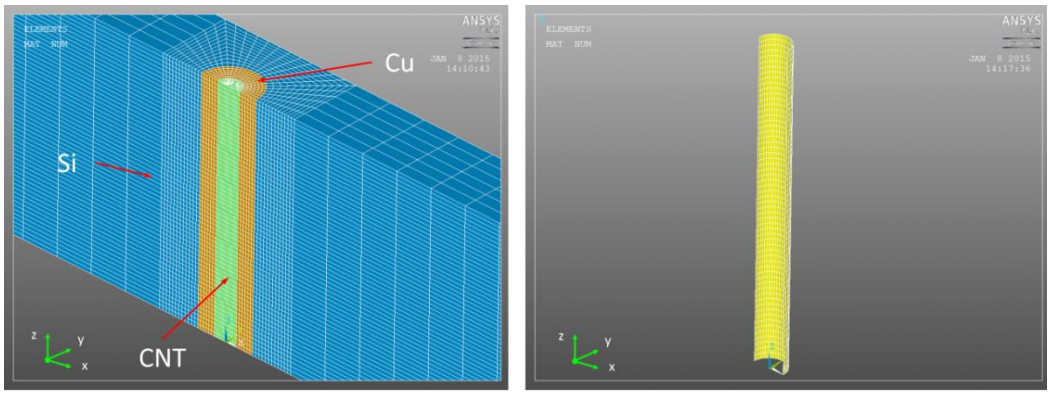

Fig. 17. Meshed model

2.2.2.2 *Thermal Cyclic Load Scenario*

To represent thermo-mechanical loading in the electronic package and its effect on the integrity of CNT/Cu interface, a model is generated in which TSV is placed within a silicon layer and attached to a substrate using die attach material (Fig. 18). This geometry is considered to mimic the real case situation in which the thermal expansion and stiffness mismatch between the substrate and silicon induces a thermo-mechanical load on silicon and consequently TSVs. TSV is placed in middle of the silicon where interfacial strains are maximum due to bending curvature. Additional TSVs are deemed unnecessary as any additional TSV further away from the center will experience lower interfacial strains.

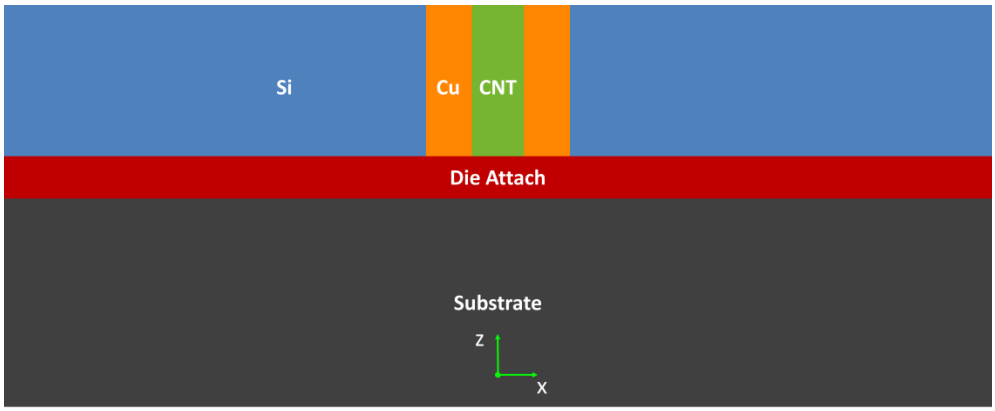

Fig. 18: Geometric representation of the thermal model

In a real case scenario, thermal loading is caused by the thermal processes that package is subjected to during the fabrication or thermal cyclic load that package is subjected to during normal field life. Temperature cycle applied to the package is selected based on Joint Electron Device Engineering Council (JEDEC) standard for accelerated testing of military and aerospace applications (Fig. 19).

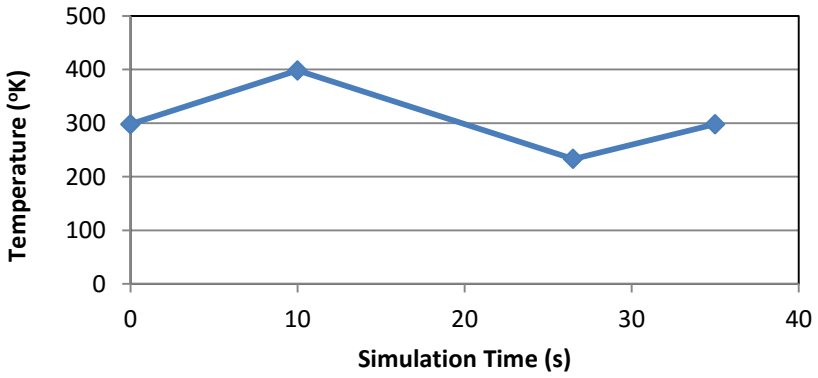

Fig. 19. Thermal loading cycle

The dimensions of the CNT/Cu-TSV and the Si are the same as the dimensions in the previous bending case. Heights of die attach and substrate are 35 μm and 250 μm, respectively. Symmetric boundary conditions are applied to this case as well (Fig. 20. In addition to the material properties indicated in Table 2, the properties shown in Table 3 are also used in the

FE model of the thermal loading case since coefficients of thermal expansion (CTE) are needed and new materials are added.

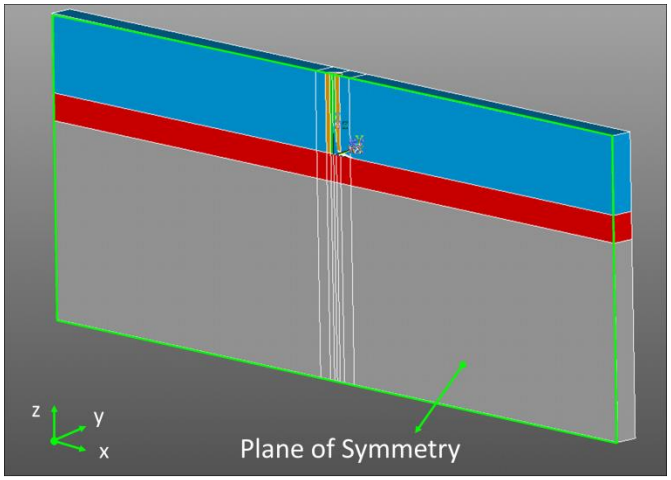

Fig. 20. Schematic of TSV in FE: thermal loading case

Table 3: FE material properties: thermal loading case [89,90]

Material	Property	Value
Si	CTE	2.33E-06 $^{o}K^{-1}$
Cu	CTE	1.43E-05 $^{o}K^{-1}$
CNT	CTE	Fig. 21
Die Attach (Linear Isotropic)	E	6 GPa
	μ	0.3
	CTE	30E-6 $^{o}K^{-1}$
Substrate (Linear Isotropic)	E	26 GPa
	μ	0.39
	CTE	15E-6 $^{o}K^{-1}$

CTE for CNT bundle is assumed to change with temperature [91] as shown in Fig. 21. Moreover, CZM parameters extracted from MD simulation for CNT/Cu interface are to be used to define the contact elements between CNT bundle and Cu.

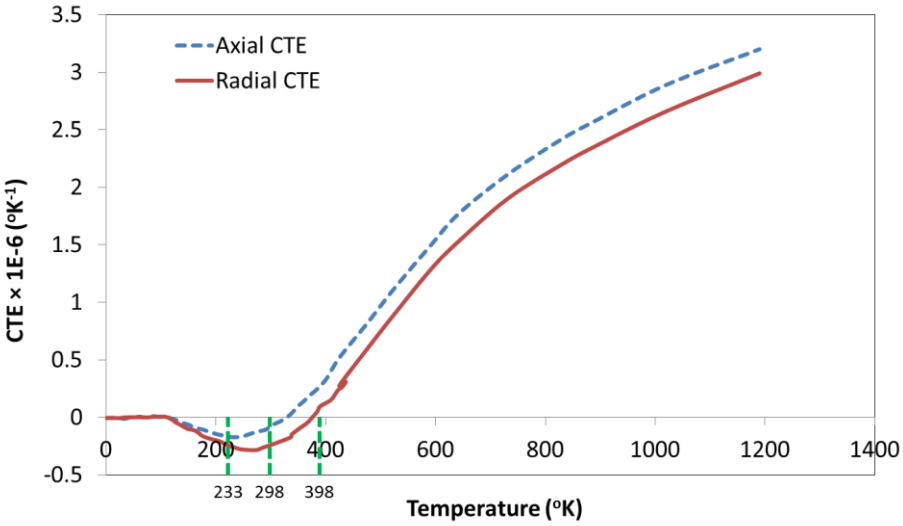

Fig. 21. CTE of CNT bundle

The same meshing technique used in bending is used for the thermal loading case. Lowermost point on the centerline is fixed in all directions in order to act as a pivot.

2.3 Fatigue Life Analysis

After studying the mechanical integrity of CNT/Cu-TSV in terms of bending loading and thermo-mechanical cycling, it becomes necessary to investigate how much improvement CNT/Cu-TSV adds to Cu-TSV under loading conditions that mimic the real-life conditions that TSVs are exposed to during operating. Although there are still practical and manufacturing issues with robust fabrication of CNT/Cu-TSVs, the promising prospect has caused many people to initiate predictions of the behavior of these structures, in particular, reliability. Reliability of TSVs is an important factor for microelectronics and semiconductor industry in adapting this technology. Fatigue life is one of the important aspects that measure the reliability of microelectronic packages. It is essential to understand the mechanical behavior under cyclic mechanical and thermo-mechanical loading. Previously, FE analysis was used to

evaluate the reliability of Cu-TSVs by applying thermal cyclic loading [89,92,93]. As expected, the mismatch in CTEs between the different components of the package is the major cause of the plastic deformation of Cu during the application of the thermal cyclic load. Moreover, different parameters such as die-attach's thickness, Cu-TSV's diameter and pitch, and under-fill's thickness have an effect on the thermo-mechanical reliability and the fatigue life of Cu-TSV. Therefore, it becomes important to study how adding CNTs to the current state-of-the-art Cu would behave under the same loading conditions. FEM can be used to investigate the fatigue life of CNT/Cu-TSV under thermal cyclic loading using the properties extracted from MD simulation. In the previous section (2.2), CZM of CNT/Cu-interface was evaluated using MD simulations. However, previously published data on Young's modulus and CTE of CNTs were used, assuming that the selected MWCNT (Fig. 14 and Fig. 12) obtains the same values, which are not particularly very relevant to the type of the CNT that is used. Therefore, additional information about mechanical and thermo-mechanical properties at the atomic level such as stress-strain behavior and CTE of the selected MWCNT are needed to be provided in order to establish more accurate multiscale model and more reliable fatigue life estimation accordingly. Thus, MD simulations are conducted to predict the required properties that are relevant to the selected MWCNT in this study. Then, FEM uses these defined properties along with CNT/Cu interfacial properties extracted from 2.2.1 to estimate the fatigue life.

2.3.1 *Molecular Dynamics Simulations*

Only the MWCNT shown in Fig. 14 is modeled. Dimensions and interatomic potentials are also the same. MD simulation is conducted here to evaluate the uniaxial stress-strain behavior and the CTE of the selected MWCNT.

2.3.1.1 *Stress-Strain Behavior of Selected MWCNT*

Uniaxial loading is applied to obtain the stress-strain behavior of the MWCNT. The system is first equilibrated at 1 ^{o}K for 100 ps at 0.5 fs-time-step and Langevin thermostat [88] along with microcanonical ensemble to conduct time integration and update the atoms' positions and velocities such that total energy is maintained constant. Then, the two lower rings of the MWCNT are fixed, while discrete displacements of 0.1 Å are applied to the two top most rings. After each displacement, the rest of the atoms are equilibrated for 10,000 time-steps, and force and displacement in z-direction for each atom are calculated. The total force and the total displacement in z-direction--F_z and d_z, respectively—are calculated by time-averaging the obtained force and displacement results over the 10,000 equilibration time-steps after each discrete displacement. MWCNT is deemed as an annular cylinder with a cross-sectional area $\left[\frac{\pi}{4}[d_o^2 - d_i^2]\right]$, where d_o is the outer wall's diameter and d_o is the inner wall's diameter. Stress (σ) is calculated by dividing the obtained F_z by the cross-sectional area, while strain is calculated as $\left[\varepsilon = \frac{d_z}{29}\right]$.

2.3.1.2 *CTE of Selected MWCNT*

CTE can be obtained by measuring the thermal expansion of the MWCNT at different temperatures. For this purpose, the MWCNT is held freely and unconstrained. Moreover, periodic boundary conditions are activated in the three dimensions. The system is equilibrated first at the desired temperature (1, 50, 100, 150, 200, 250, 300, 350 or 400 ^{o}K) using Langevin thermostat and the microcanonical ensemble for 25 ps. At this point, the temperature, pressure and the energy of the system stabilize. Then, equilibrating the system at the desired temperature and 0-bar-pressure continues using the isothermal-isobaric ensemble [94] for 300,000 time-steps. Since CNTs have shown anisotropic thermal expansion; axial expansion is different than radial expansion [95]. Hence, anisotropic pressure change is activated which allows the MWCNT dimensions to deform independently in x, y and z direction. The average radius is calculated at each time-step. The radius is calculated as the average distance between the atoms of the outermost layer and the center of mass of the MWCNT. Axial length is also calculated at each time-step. It is calculated as the distance between the centers of mass of the lowermost 3 rings and the uppermost 3 rings. Radii and lengths are time-averaged over the last 100,000 of the equilibration and the final radius and length are calculated. The previous technique is conducted at different temperatures (1, 50, 100, 150, 200, 250, 300, 350 or 400 ^{o}K). The reference radius and length are calculated at 1 ^{o}K, and thermal expansions at each temperature are calculated with respect to them. Axial and radial coefficients of expansions (CTE_a and CTE_r, respectively) are calculated form the following relations:

$$CTE_a = \frac{\frac{l-l_o}{l_o}}{T-T_o} \qquad \text{Eq. 3}$$

$$CTE_r = \frac{\frac{r^{CNT} - r_O^{CNT}}{r^{CNT}}}{T - T_O} \qquad \text{Eq. 4}$$

such that l is the MWCNT's length at temperature (T) and l_o is the MWCNT's length at the reference $T_o = 1$ ^{o}K. And, r and r_o are the MWCNT's radii at temperature (T) and $T_o = 1$ ^{o}K, respectively.

2.3.2 *Package Geometry, Dimensions and Finite Element Model*

The current FEM in the last chapter is modified in order to achieve more realistic results the mimic Electronic packages typically consist of many layers. CTE and stiffness mismatch between these layers are the main source of interfacial stresses that are formed during thermal loads. The interfacial stresses caused by the thermal mismatch at any point depend on the distance from the neutral point. This characteristic dictates larger stresses at the corners and further from the center of the package [96,97]. The interfacial stresses in turn transfer to the layers themselves and any component within any layer is then subject to stresses that are resultant of the thermal mismatch. TSVs are not excluded from this mechanics. High stresses on the TSV during operation at different temperatures may cause it to deform plastically. Consequently, low cycle fatigue may occur in Cu-TSV interconnects. Cu is expected to deform plastically far earlier than CNTs. Therefore it is the key material to be studied. In order to obtain the stress distribution within a package, a rough model is developed in which a single TSV placed at the edge of a wide enough Si wafer attached to a substrate using die attach material as shown in Fig. 22. A single TSV is used because modeling multiple TSVs will increase the computational time substantially, especially when contact elements are used to define the CNT/Cu-interface. A base model is developed with the same structure, but a TSV

made fully from Cu. The objective is to compare the fatigue life of CNT/Cu-TSV with Cu-TSV's life.

Symmetry is utilized to reduce the model size and computational time. Therefore, only a quarter of the package is modeled as shown in Fig. 22. Furthermore, only a slice of the model that contains one TSV is developed. Therefore, the thickness of the model in y direction is only 30 μm. CNT/Cu-TSV is 100 μm deep 25 μm diameter. CNT bundle is 10 μm diameter. Die attach and substrate layers are 35 μm and 250 μm high, respectively. The length of the model in x-direction is 1000 μm. The length is chosen to be long enough in order to give sufficient observation of the deformation in the model's components.

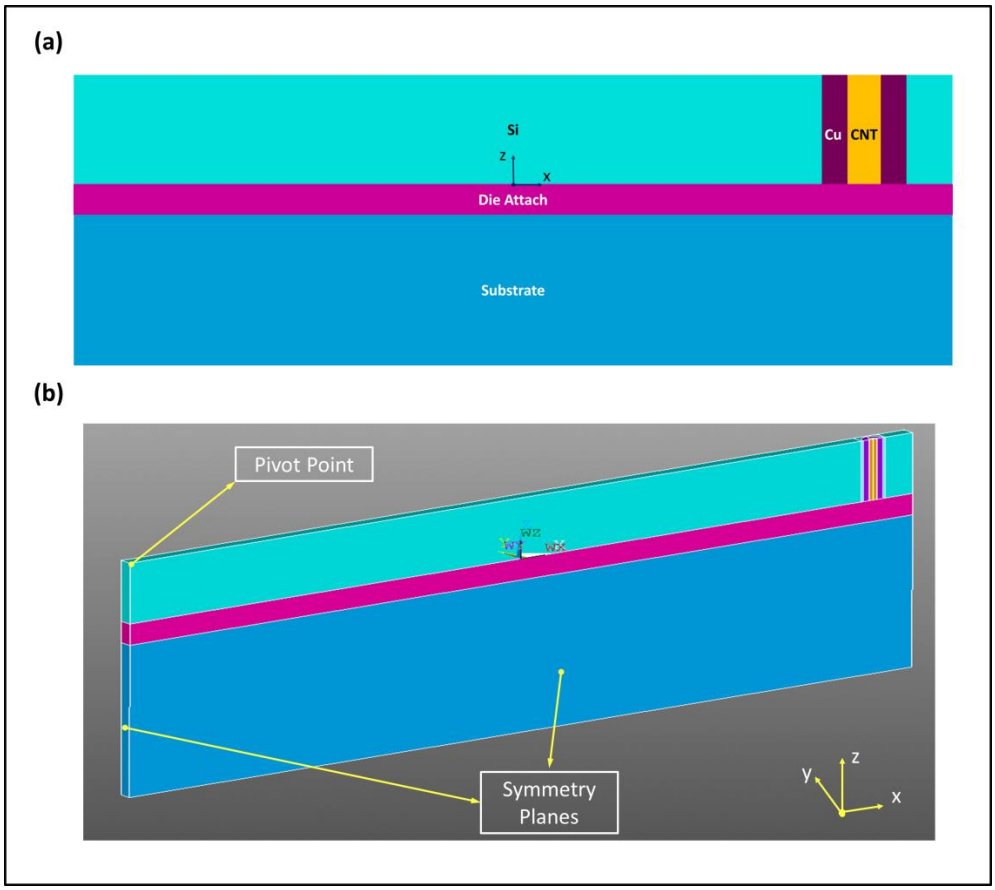

Fig. 22. [a] Schematic of the CNT/Cu-TSV's model; [b] Geometric model used in the FE analysis

The same element types used in the previous FEM in section 2.2.2 are assigned to the package components in the current FEM. Material properties of Si, Cu, die attach and substrate are the same as those listed in Table 2 and Table 3. MD results resulted from the simulations described in section 2.3.1 are used to define the non-linear uniaxial behavior and the CTEs of CNT bundle in FEM.

Cohesive zone properties resulted from the simulations in section 2.2.1 are assigned to the contact elements. The Standard accelerated JEDEC temperature cycle is applied on the FE model in order to induce thermo-mechanical load (Fig. 19). Usually, this standard thermal cycle includes a dwell after each heating-up and cooling-down step in order to study the creep effect. However, creep is not expected in the materials used in this analysis and therefore, the dwelling time is eliminated. The model is conducted for several cycles for the plastic hysteresis to stabilize. Fatigue life calculation is based on the plastic deformation amplitude obtained for the third cycle.

CHAPTER 3. SIMULATION RESULTS

3.1 Interfacial Behavior

The results of the case studies related to SWCNT are presented in this section. Different arrangements of SWCNT at the interface with Cu have been studied. The effect of several factors on the interfacial behavior has been evaluated. These factors include number of SWCNTs, SWCNT length, point of loading, boundary conditions, nonuniform loading and inner layers. Finally, considering the effect of the different parameters, an analytical expression for the interfacial shear strength of SWCNT/Cu-interface has been derived.

3.1.1 *The Effect of the Number of SWCNTs*

First, the effect of the number of aligned SWCNTs is explored. Fig. 23 depicts the simulation models for four arrangements at different stages; before minimization and equilibration, after minimization and equilibration, during pull-out and after pull-out. The last vertical layer of Cu atoms not in contact with the SWCNTs is fixed in all directions during simulation. Pull-out force is calculated by summing up carbon atoms' forces in Z direction.

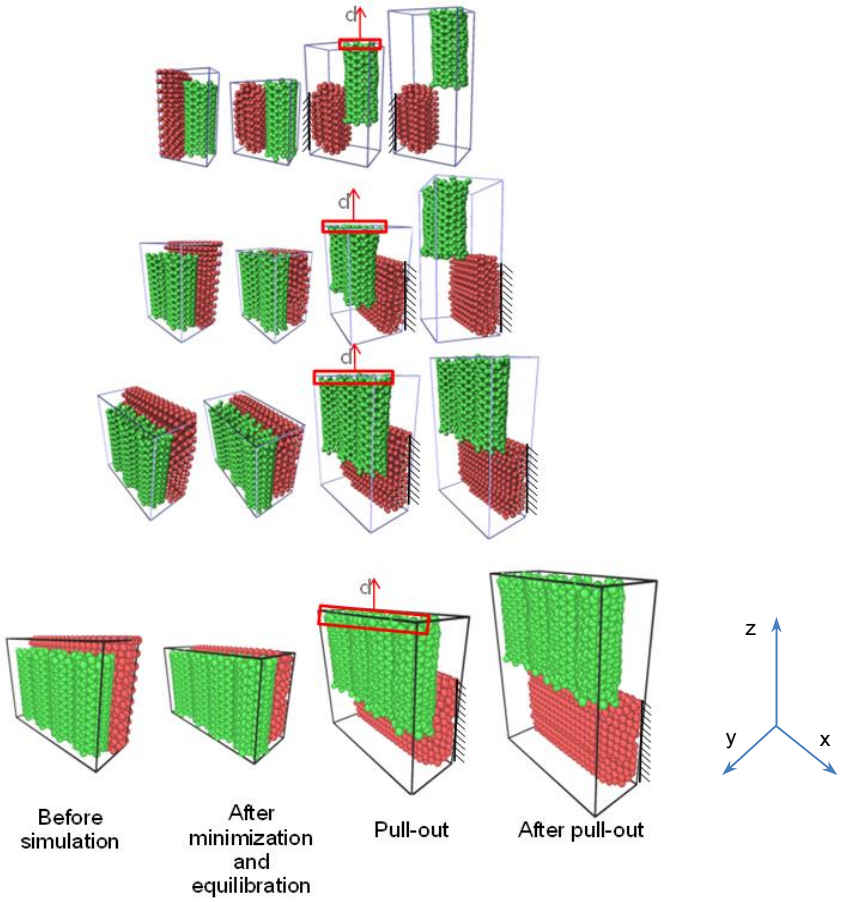

Fig. 23. Simulation of aligned SWCNTs

Fig. 24 shows the resulted force-displacement curves. The common behavior of the four simulated arrangements is that the force increases to a certain value at the beginning then it oscillates with constant decreasing amplitude until force drops to zero at the end of the pull-out. These oscillations are due to vdW interactions' separation and re-attraction with Cu atoms i.e. (stick-slip behavior [98]); when separation occurs there is a sudden drop in force but this is followed by re-attraction of C-Cu vdW interactions with adjacent atom of SWCNT. After the first peak, force oscillates around a constant average value until the last three maxima when significant deterioration is observed.

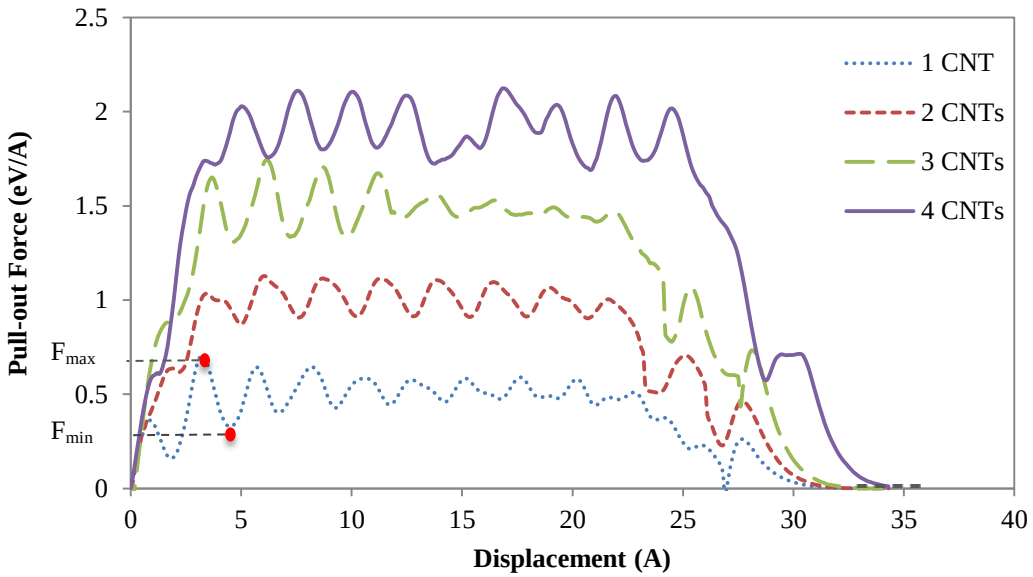

Fig. 24. Number of aligned SWCNTs' effect

Generally, fracture is neither observed in SWCNT or Cu. The SWCNT was completely pulled-out with no further rearrangement in the Cu atoms. So, the separation is attributed to the weak interatomic interaction between SWCNT and Cu modeled by Lennard-Jones potential. According to Amonton's friction law with adhesion [99], the total friction force is given by:

$$F = \mu L + F_o \qquad \text{Eq. 5}$$

where μ, L and F_o are the coefficient of friction, external normal force and internal force due to adhesion respectively.

The external normal force may come from non-uniformity of connection between SWCNT and Cu, such as waviness of SWCNT and mismatch in coefficient of thermal expansion (CTE) or an applied external force. In this study, there is not applied normal force (L) and the interface is deemed perfect. Thus, the force to consider in is only the internal force due to adhesion (F_o) i.e. vdW force that dominates the pull-out force.

Fig. 25 shows the maximum, force (F), average force (F_{avg}) and the maximum amplitude (F_{max}-F_{min}) of oscillation for each arrangement. It is clear that (F) and (F_{avg}) are linearly proportional with the same slope to the number of adjacent SWCNTs (N). The trend of the maximum and average forces could be estimated for more SWCNTs by extrapolating these relationships:

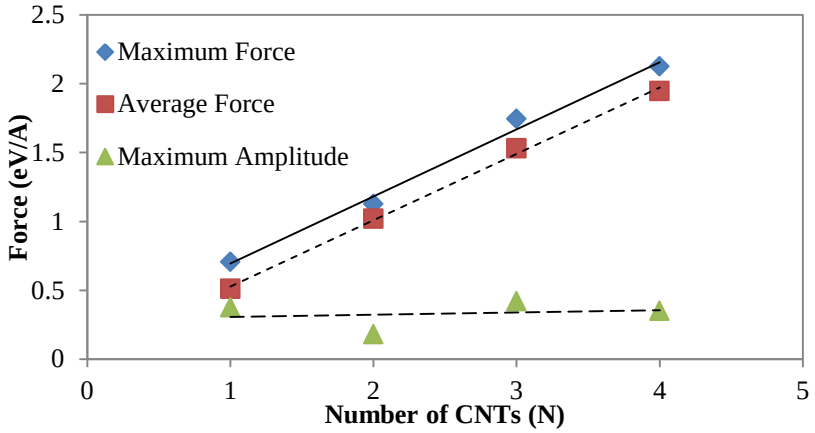

Fig. 25. Pull-out forces - Number of SWCNTs curve

$$F = 0.487N + 0.2064 \qquad \text{Eq. 6}$$

$$F_{avg} = 0.482N + 0.0468 \qquad \text{Eq. 7}$$

From Fig. 25, the maximum amplitude is almost constant in all cases. This is discussed in the next part when embedded length effect is studied.

3.1.2 *The Effect of the Length of SWCNTs*

The effect of the SWCNT embedded length has been studied as well. Different lengths of single SWCNTs are simulated. The simulated lengths are 26 A^o, 36 A^o, and 52 A^o. Fig. 26 shows the resulted pull-out force-displacement curves for these three cases. As seen in this figure, the average force is the same for SWCNTs with different lengths. However, the amplitude of the oscillation is increasing as the length of the SWCNT increases. The amplitude is believed to be

the result of summation of the forces between each pair of SWCNT-Cu atoms in stick and slip situation. As the number of SWCNT atoms that are in contact with Cu atoms increases, the force summation increases, resulting in larger amplitude in the oscillation in longer SWCNTs. That could explain the constant amplitude observed in Fig. 25, as the embedded length is the same for all the cases in that figure.

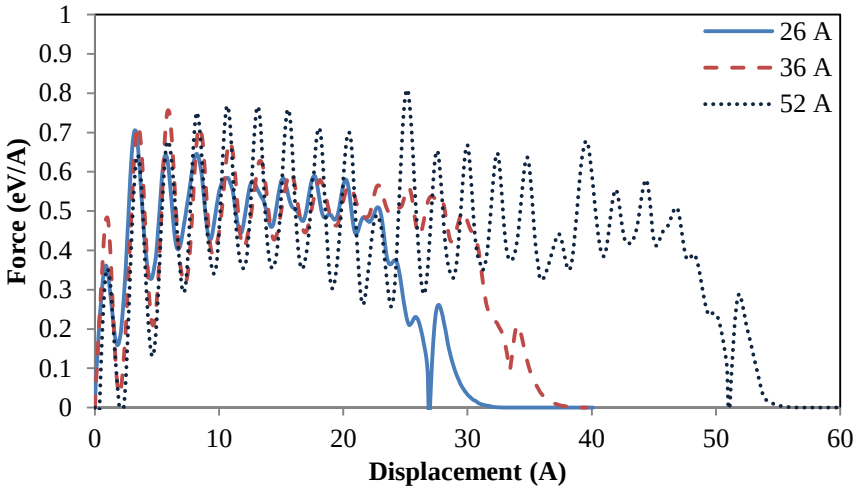

Fig. 26. Embedded length's effect

3.1.3 *The Effect of Nonuninform Loading*

In order to evaluate the adhesion between the SWCNTs themselves, in one case, the load was only applied on one SWCNT while the other SWCNT strand was left standing freely adjacent to it. The model and the force displacement results are shown in Fig. 27. As seen in this figure, the amount of force that is required for this case is less than the force applied to both SWCNTs. One SWCNT moves out of Cu and the other remains attached to it. This is because C-Cu vdW interaction is stronger than SWCNT-SWCNT vdW interaction. As the number of the dominant C-Cu interactions is fewer in this case, pull-out force will decrease as shown in Fig. 27. This case is also compared with pulling-out one SWCNT (Fig. 27). The force required to pull-out one

standalone SWCNT is less than the force of the current case. This is attributed to that more force is required to overcome, both, C-Cu and SWCNT-SWCNT vdW interactions instead of only C-Cu interactions, however, C-Cu interaction is still dominant as it has major effect on the pull-out force.

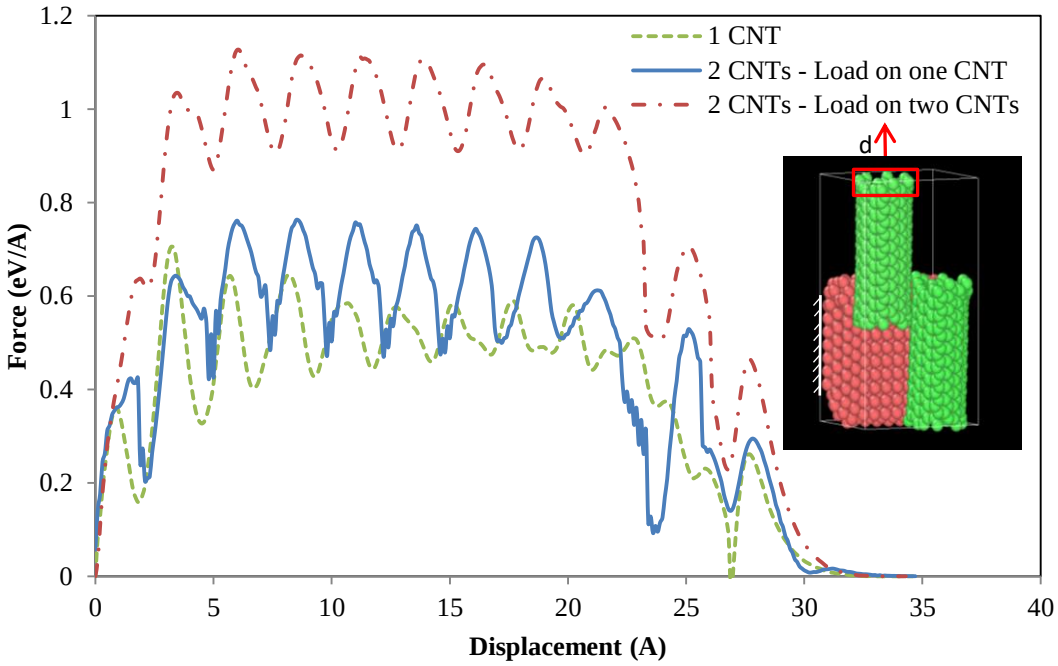

Fig. 27. Point of loading's effect

3.1.4 *The Effect of Fixed Boundary Conditions*

In the case of SWCNT bundle inside an annular Cu cylinder, the SWCNTs may also be connected to the bottom of TSVs (end-contact). Therefore the boundary condition on the bottom side of the SWCNTs may play a significant role. Therefore, it's important to evaluate the effect of end contact connections on the interfacial strength. For this reason, another model is built in which the boundary condition for the SWCNTs base was changed such that the two lowermost rings of one of the SWCNTs were completely fixed. As expected, witness to strong bond between SWCNT atoms, the amount of force that is required to pull out the SWCNTs

increases exponentially to mid-hundred eV/A as seen in Fig. 28. The oscillating behavior is eliminated in the results or perhaps absorbed in the magnitude of this force and not discernible. In this case the SWCNT behaves as being loaded in tensile test and what is measured in load-displacement curve is essentially the strength of the SWCNT strand. After maximum force is attained, the force drops in several increments. Each increment corresponds to a C-C bond breaking. After all the bonds are broken, the forces reaches zero.

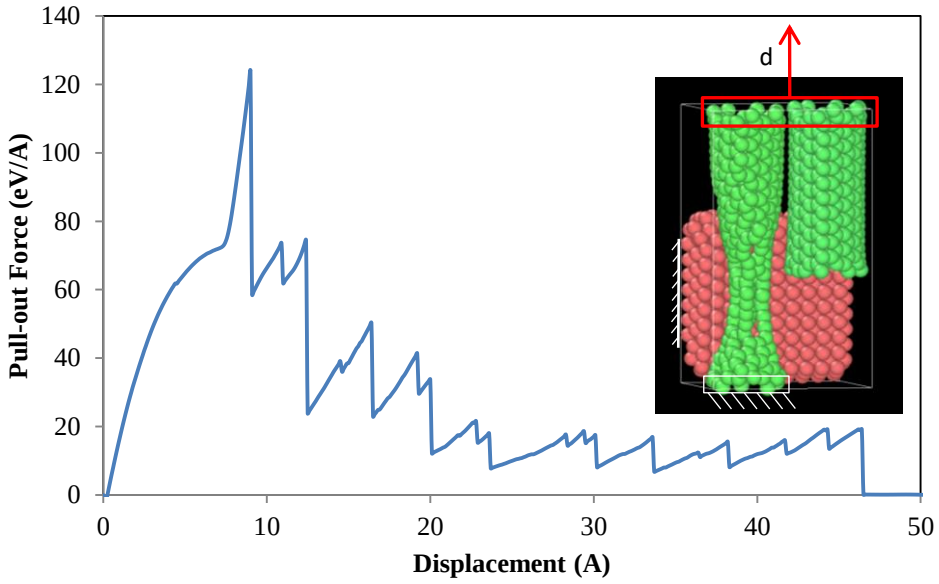

Fig. 28. Applicaton of load when SWCNT strand is completely fixed at one side

3.1.5 *The Effect of Inner Layers of CNTs*

If SWCNTs are used as bundle in interconnects, inevitably some SWCNTs will be in contact with Cu and some will be in contact with other SWCNTs and won't have a direct contact with Cu. It is essential to know if adding more SWCNT strands which are not directly adjacent to metallic material has the same effect as adding them adjacent to Cu. So in another arrangement, the original case of two SWCNTs adjacent to the Cu was changed and one SWCNT strand was

added on top of two SWCNTs such that it did not have any contact with Cu. This arrangement is shown in Fig. 29.

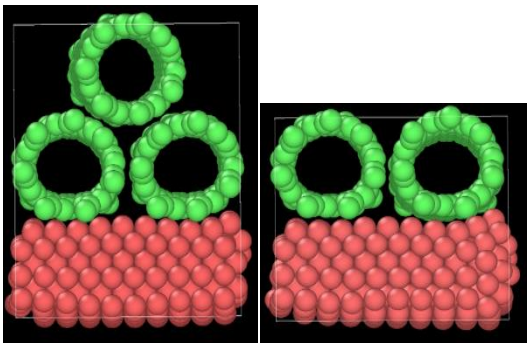

Fig. 29. The MD simulation structure when SWCNT strand is added to the top

Interestingly, the amount of average force that is required to pull-out new three strands of SWCNTs in this case is the same as the amount of average force to pull out two SWCNTs which are directly adjacent to Cu (Fig. 30). The average force is the force used in calculation of the shear strength and therefore of more interest to this study.

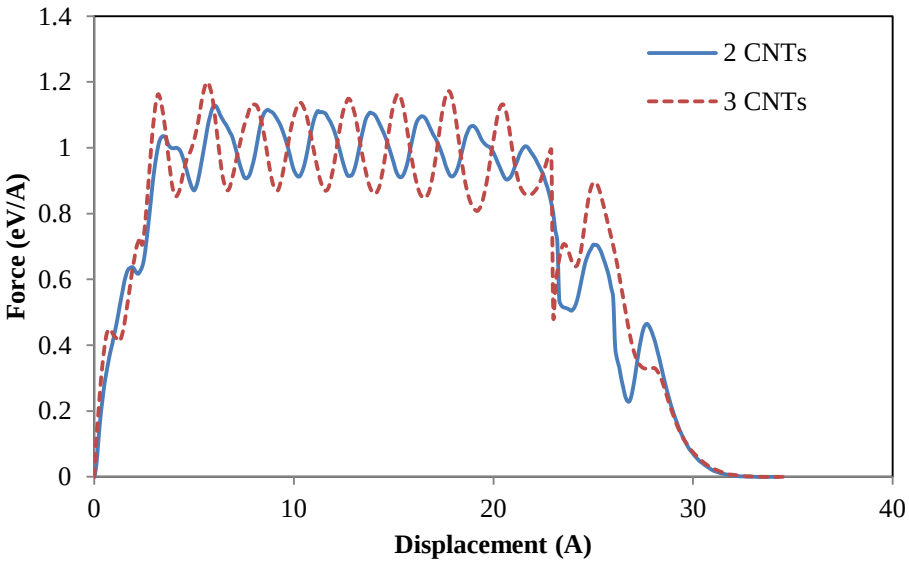

Fig. 30. Force - displacement curve to show the second order interaction effect

3.1.6 *Evaluation of the Interfacial Shear Strength*

After pull-out force calculation, τ_{max} can be determined. In this study, perfect interface is assumed. In the selected SWCNT, waviness, mismatch in coefficient of thermal expansion (CTE) and applied normal force do not exist. So, Eq. 5 reduces to

$$F = F_o. \qquad \text{Eq. 8}$$

Consequently, the interfacial shear strength will be induced only by C-Cu vdW interaction. If τ_{max} is deemed constant along the embedded length and(τ_{max}) is calculated by dividing maximum (F) by interfacial area as in [34], pull-out force (F) will vary with the change of length during pull-out, which contradicts with the previous force-displacement results. Thus, this assumption is inappropriate for a perfect interface. Moreover, according to this assumption, when SWCNT's length is extremely long (∞), the interfacial shear strength approaches to zero, which is irrational. Therefore, shear strength is only contributed by separation and rejoining of C atoms i.e. (stick-slip) behavior as shown in Fig. 31. The same rationale was used to obtain the interfacial shear strength by Li and Liu et al. [35,100,101]. When an atom of C is pulled out of two Cu atoms the oscillatory behavior takes place. Apparently, as seen in Fig. 31, oscillations are attributed to stick-slip behavior. The wave length of this oscillation is (a). This process repeats itself every specific displacement (a) and takes place along the SWCNTs. Moreover, (a) denotes the atomic spacing of Cu. The work (w) done by this force to overcome vdW interaction is given by the area under the curve:

$$w = F_{avg} a \qquad \text{Eq. 9}$$

where (F_{avg}) is the average force.

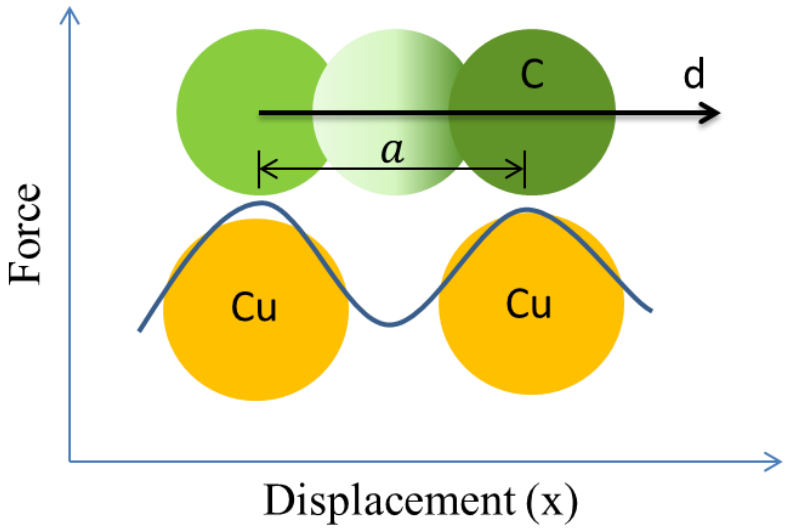

Fig. 31. Illustration of the work done by pull-out forces

On the other hand,

$$w = \int_0^a F(x)dx. \qquad \text{Eq. 10}$$

As $F(x)$ is induced by the interfacial shear strength (τ_{max}), and it is assumed to be uniform along the distance (a):

$$w = \int_0^a \tau_{max}\, c a \mathrm{dx} \qquad \text{Eq. 11}$$

where (c) is the interfacial length For example, in the case of two SWCNTs in contact with Cu (Fig. 32), (c) is the distance given by (c_1+c_2)

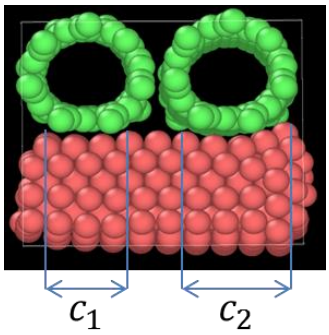

Fig. 32. Illustration of the interfacial length

From equations 9, 10 and 11,

$$w = F_{avg}a = \int_0^a \tau_{max}\, ca\mathrm{dx}$$

$$F_{avg} = \tau c(x)_0^a = \tau_{max} ca$$

$$\tau_{max} = \frac{F_{avg}}{ca}. \qquad \text{Eq. 12}$$

(F_{avg}) can be predicted from $F_{avg} = 0.482N + 0.0468$ Eq. 7. From Fig. 32, only 90% of C atoms, of both strands, are in contact with Cu. Therefore, for a bundle of SWCNTs, (c) is$[0.9(2\pi r)]$, where (r) is the radius of the bundle. Thus, interfacial shear strength could be predicted.

3.2 Cohesive Zone Model Evaluation

Normal CZM has been evaluated by applying a series of pull-out tests in the direction normal to the interface between MWCNT and Cu. The effects of number of walls of a MWCNT and temperature have been also investigated.

3.2.1 *The Effect of the Number of Walls*

First, the effect of the number of MWCNT's walls is explored. Fig. 33-a depicts the simulation models for 2, 3, 4, 5, 6 and 7-wall MWCNTs right after equilibration at 1^o K. Fig. 33-b shows the different stages during the simulation: before equilibration, after equilibration, during loading and after separation. Cu atoms are fixed in all directions during simulation. In order to calculate stress, carbon atoms influenced by C/Cu vdW interaction must be determined first. Carbon atoms that lie within C/Cu cut-off distance (distance within which C atoms are influenced by vdW interaction [73]), which is approximately 7.7 Å, are believed to be the ones influenced by the vdW interaction. That is why only the first and second wall of the MWCNT

at the interface with Cu are studied. The average stress in the direction of loading, y-direction, is calculated over the atoms enclosed in the red box indicated in Fig. 33-b. Stress per atom is calculated using $\sigma_{ij} = \frac{1}{V}\sum_{\alpha \in V}\left[\frac{1}{2}\sum_{\beta=1}^{N}\left(r_i^{\beta} - r_i^{\alpha}\right) f_j^{\alpha\beta}\right]$ Eq. 2 for each atom inside the box then the average is computed in order to give the average stress per atom. The Average displacement of the same group of atoms in that region is calculated in the same manner as stress.

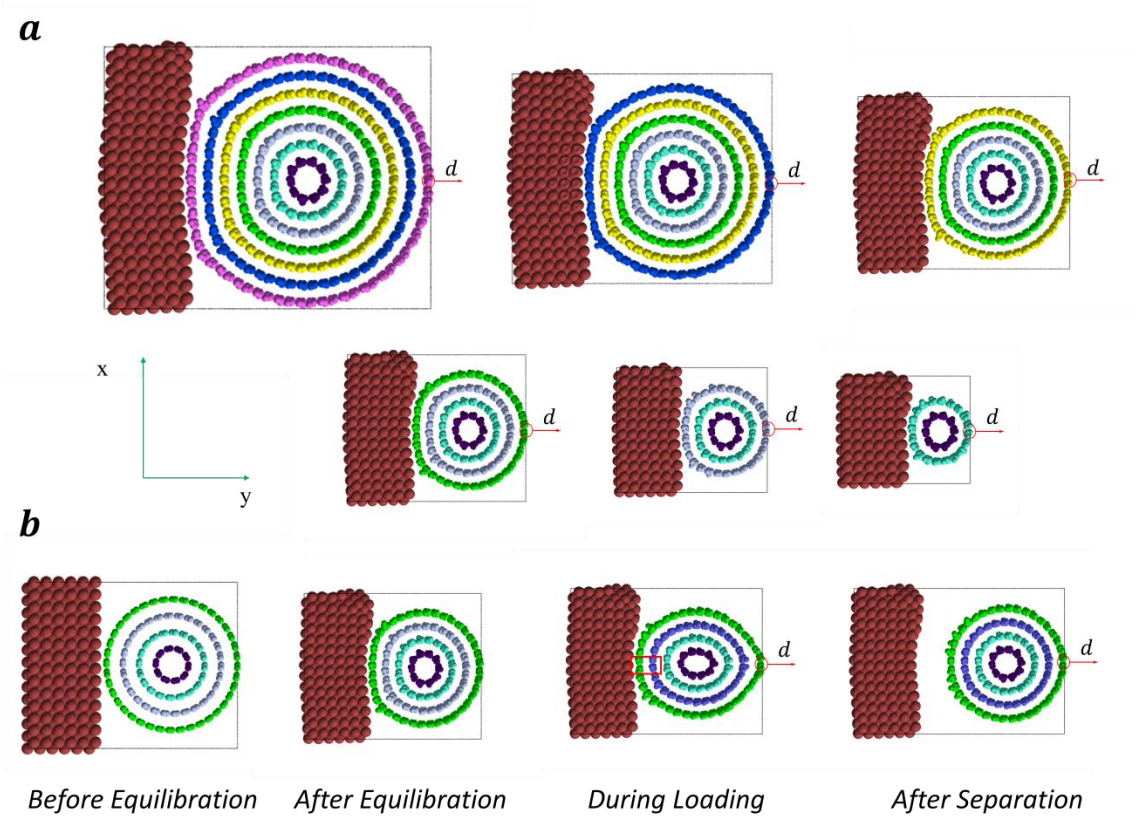

Fig. 33. [a] Simulation of MWCNT, [b] simulation stages of 4-wall MWCNT

Fig. 34 shows the resulted normal stress-displacement curves. The common behavior of the simulated MWCNTs is that the stress (σ) starts initially at some negative value, compressive stress due to equilibration, and increases until it becomes zero at a certain intermolecular

distance ($b \cong 0.2$ Å) then it increases to a maximum value at displacement (δ_n). After this point, stress drops rapidly with increasing displacement until separation takes place. As shown in Fig. 34, dropping down behavior changes and depends on the number of walls. By tracking C/Cu vdW potential energy, separation always takes place at $\delta \cong 5.8$ Å, point marked in red in Fig. 34; however, this in not the point at which normal stress stabilizes when the number of walls goes beyond three walls. Even after MWCNT strand is separated and stabilized, some compressive stress remains in it due to inter-tubular interaction and it is increasing with increasing number of walls.

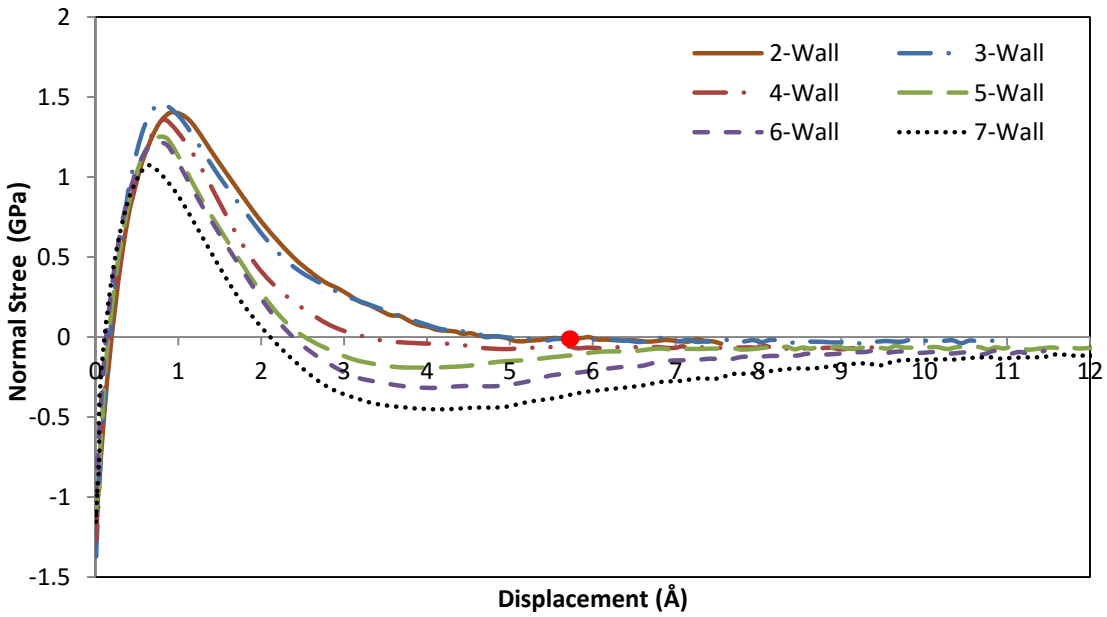

Fig. 34. Number of walls effect

Fig. 35 shows the 5-wall MWCNT at different instants: (1) before separation, (2) at the instant of separation, and (3) after separation. After the second zero-stress is attained, the inner layers of MWCNT strand are squeezed due to pulling of the outer layer. Thus as the strand is squeezed, inner walls push the outer walls farther towards Cu causing a gradual increase in the

compressive stress of the studied group of atoms until maximum compressive stress occurs at point 1. Then compressive stress starts to decrease as C/Cu vdW interaction starts to deteriorate until the interatomic potential reaches to zero eV at point 2. Between points 1 and 2 the MWCNT tries to retrieve its cylindrical configuration and relieve the gained compressive stress until it stabilize at point 3. Even though the MWCNT is stable, there is some compressive stress residue due to the effect of C/C vdW interaction during loading.

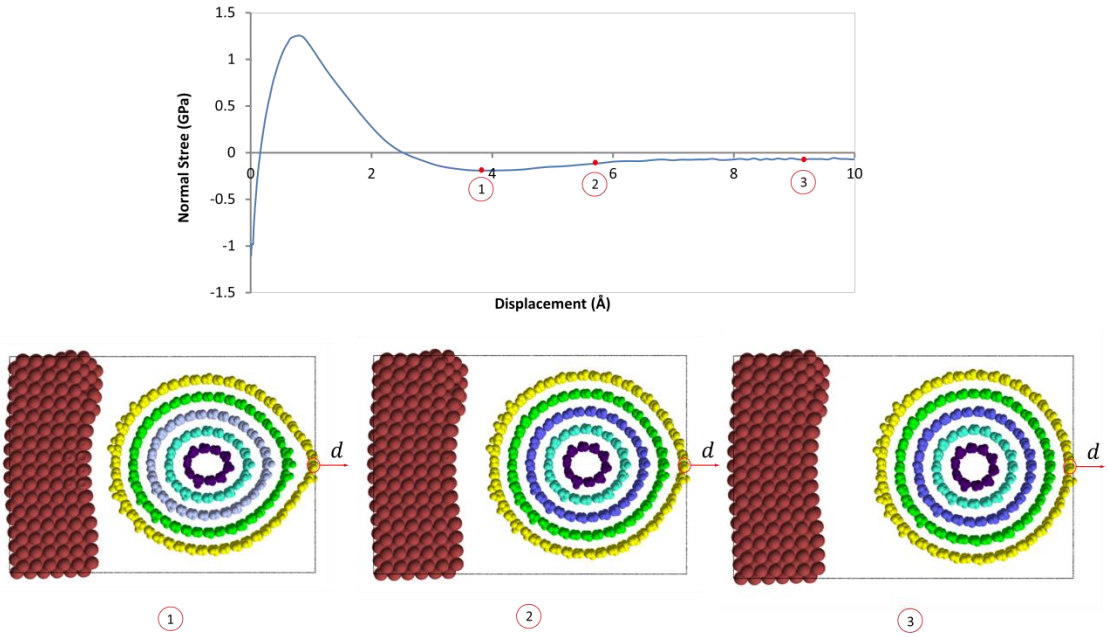

Fig. 35. Squeezing of 5-wall MWCNT

As noticed from Fig. 34, dropping down behavior, maximum normal stress and the accompanied displacement are changing with changing the number of walls. There are many CZM models proposed by scientists and Barenblatt model [102] is found to best fit the results in this study except for the compressive stress region at the end of the pull out. Maximum normal stress, normal cohesive strength (σ_{max}), and the displacement at this point (δ_n) are the key parameters in the study of CZM. Thus, the effect of number of walls on those parameters is studied. From Fig. 36, σ_{max} decreases non-linearly, polynomial fit of degree 2 with a

correlation coefficient of 0.97, with the increase of the number of walls from 2 to 7-wall MWCNTs. The current hypothesis is that as the number of walls increases, C/C vdW interaction increases between the walls resulting in pulling the outermost walls that are in the interface with Cu towards the centers of the MWCNT. Thus the C/Cu interface becomes weaker.

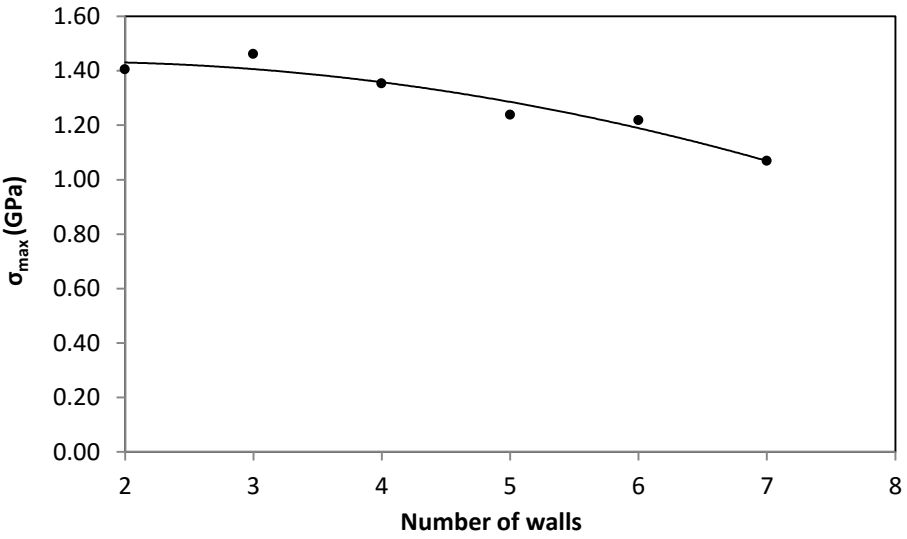

Fig. 36. Normal cohesive strength – Number of Walls curve

The relationship between δ_n and number of Walls is shown in Fig. 37. As the number of walls increases from 2 to 7, δ_n decreases non-linearly, logarithmically with a correlation coefficient of 0.9. From Fig. 34, Fig. 36 and Fig. 37, as the number of walls increases, interfacial stiffness remains constant but σ_{max} and δ_n decrease which means that the CZM gets weaker.

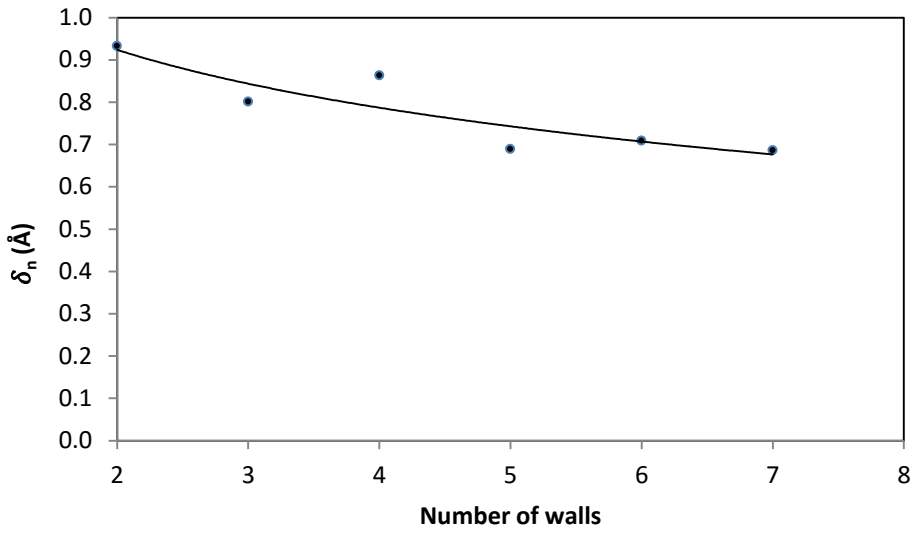

Fig. 37. δ_n – Number of Walls

3.2.2 *The Effect of Temperature*

Temperature effect was also studied. 3-wall MWCNT was simulated at different temperatures (from 1°K to 398°K). First the system of MWCNT-Cu was equilibrated at the desired temperature and then load is applied in the same manner. Resulted Normal Stress - displacement curves (CZM models) for the temperatures are shown in Fig. 38. As depicted from the curves, there is an abrupt change in the CZM when temperature changes from 1 to 75 K.

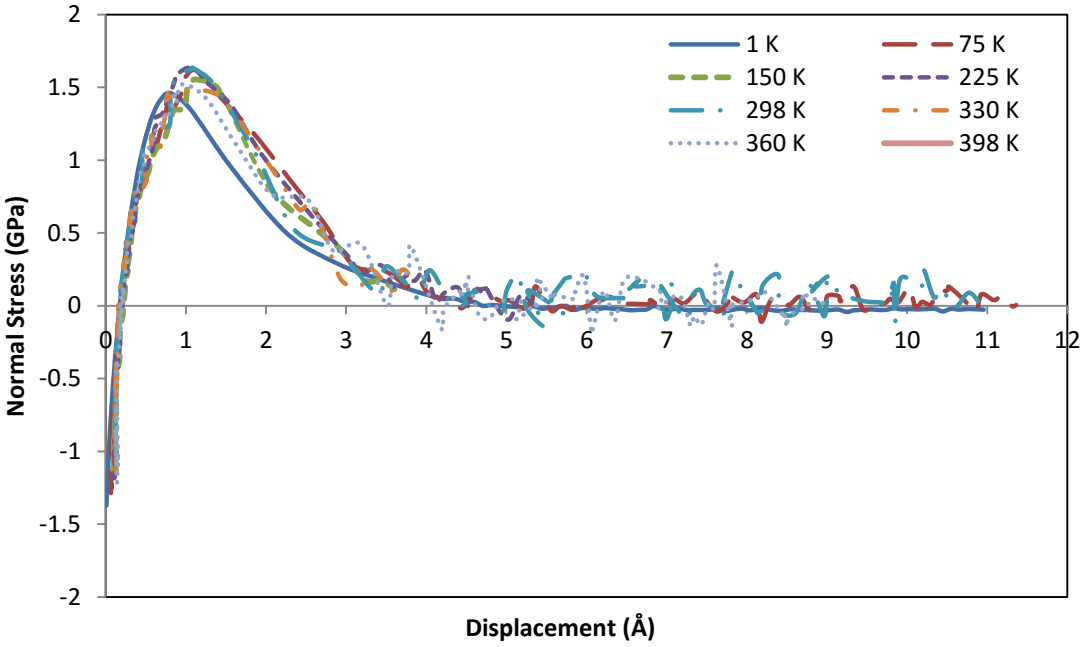

Fig. 38. Temperature effect on CZM

Fig. 39 and Fig. 40 summerize the relationship between temperature and both σ_{max} and $\delta_n$respectively. To evaluate the results systematically, a statistical analysis was conducted using IBM SPSS software [103]. An inverse functional relationship ($\sigma_{max} = c_1 + \frac{c_2}{\text{Temperature}}$ and $\delta_n = c_3 + \frac{c_4}{\text{Temperature}}$) was found to best fit the relationship between temperature and both σ_{max} and δ_n after conducting F-tests. The Coefficients of determination (r^2), which indicates how much the model explains the variability of the response data (σ_{max} or δ_n) around their mean, were evaluated for both sets of data. The closer this coefficient is to unity, the stronger evidence it is that there is a relationship between the temperature and each parameter. They have been found to be 0.35 and 0.68 for σ_{max} and δ_n respectively. These values are small indicating that there is not true relationship between temperature and both σ_{max} and δ_n. These small values also indicate that the variation on the

results is most likely caused by the randomness in the test. As the temperature increases, the kinetic energy increases and atoms oscillates with higher frequencies introducing some noise to the extracted results. Nonetheless, there seems to be a jump in the values as the temperature is increased from 1°K to 75°K. For the temperatures higher than 1°K, relative standard deviation was calculated for σ_{max} and δ_n. It shows 4% and 6% for σ_{max} and δ_n respectively. Thus, temperature has no significant effect when temperature is higher than 1°K.

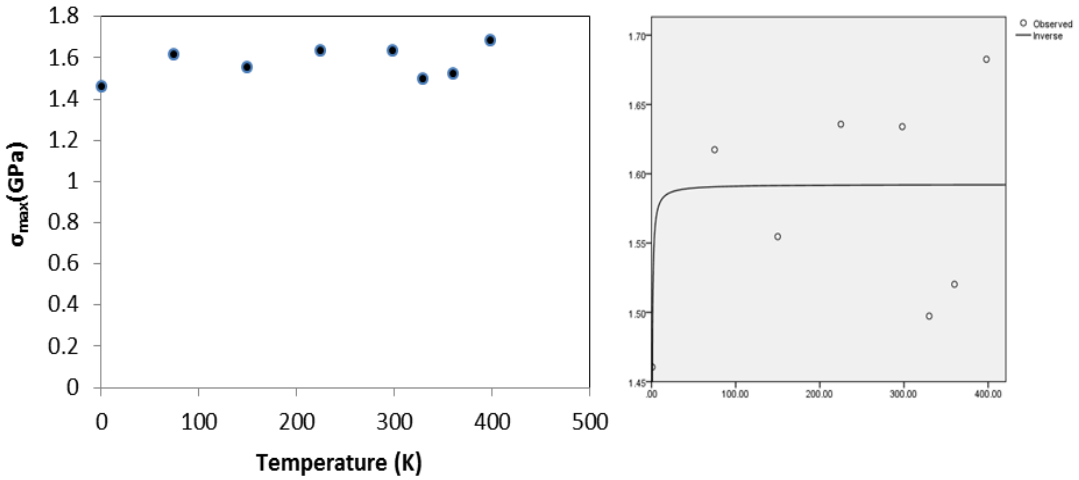

Fig. 39. Temperature effect on $\boldsymbol{\sigma_{max}}$

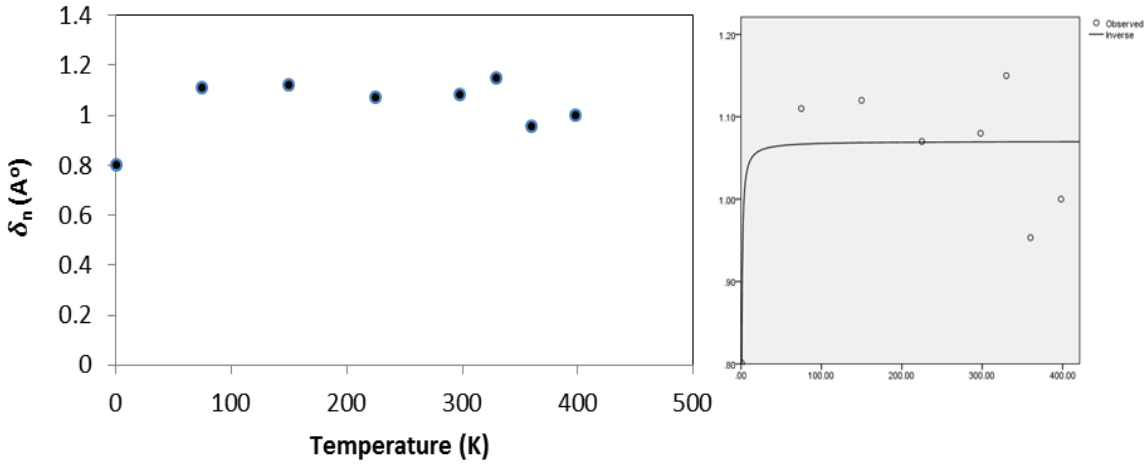

Fig. 40. Temperature effect on $\boldsymbol{\delta_n}$

3.3 Multiscale Behavior

Considering the previous finding, a multiscale modeling approach is conducted in order to evaluate the mechanical integrity of CNT/Cu-TSV. The current approach links nano- and microscales by using CZM parameters of CNT/Cu-interface extracted from MD simulations and using them in a continuum level finite element model.

3.3.1 *MD Results*

Two pull-out tests scenarios have been performed on the selected MWCNT (Fig. 12). Pull-outs in the axial direction and normal to the axial directions have been in order to evaluated the axial and normal CZMs, respectively.

3.3.1.1 *Pull-out in the Axial Direction*

C-Cu vdW potential energy (E_{vdW}) was calculated after each displacement controlled loading step. The pull-out force in z-direction (F_z) for a displacement (Δd_z) could be represented in terms of the change in C-Cu vdW potential energy (ΔE_{vdW}) as,

$$F_z = \frac{\Delta E_{vdW}}{\Delta d_z} \qquad \text{Eq. 13}$$

such that Δd_z is equal to the discrete pull-out displacement (0.1 Å) [101]. From the F_z – displacement curve (Fig. 41), force oscillates due to the slip-stick behavior [98] (separation and rejoining of C-Cu vdW interaction). This is a common behavior observed in many MD pull-out tests [48,87]. The amplitude in the current case is thought to be the result of the summation of the forces between each pair of C-Cu in slip-stick situation. As the number of C atoms in contact with Cu increases, the summation of forces increases and the oscillation's amplitude increases in return [87]. That explains the large amplitude in the current case since there are hundreds of C atoms in contact with Cu. As discussed in a previous study [87], average pull-out force is of concern in interfacial shear strength (τ_{max}) determination. The wide oscillations or fluctuations make it hard to predict the trend of the force-displacement curve. A moving average technique is used in many applications to smooth out short-term fluctuations and noise in order to emphasize the long-term significant trend of the curve [104]. Increasing the period size—the number of elements to be averaged—will enhance smoothing the curve but care has to be taken because increasing the period size will increase the number of eliminated elements and lost information. Therefore, force was averaged using moving average method with a period of 9, because less period sizes were found to give fluctuations that did not follow the intuitive trend and did not provide sufficiently smooth pattern. Fig. 41 shows the resulted curve after applying moving average technique. Form the behavior of the curve, average force starts at zero at the beginning of the pull-out test, then it begins to increase gradually until the maximum average force is attained (F_{avg}^{max}). After that it remains constant until complete

separation occurs and it drops down to zero. Interfacial shear strength (τ_{max}) [87] is a function of F_{avg}^{max}, oscillation wavelength (a) and the length of the interface (c). Thus,

$$\tau_{max} = \frac{F_{avg}^{max}}{ca}. \qquad \text{Eq. 14}$$

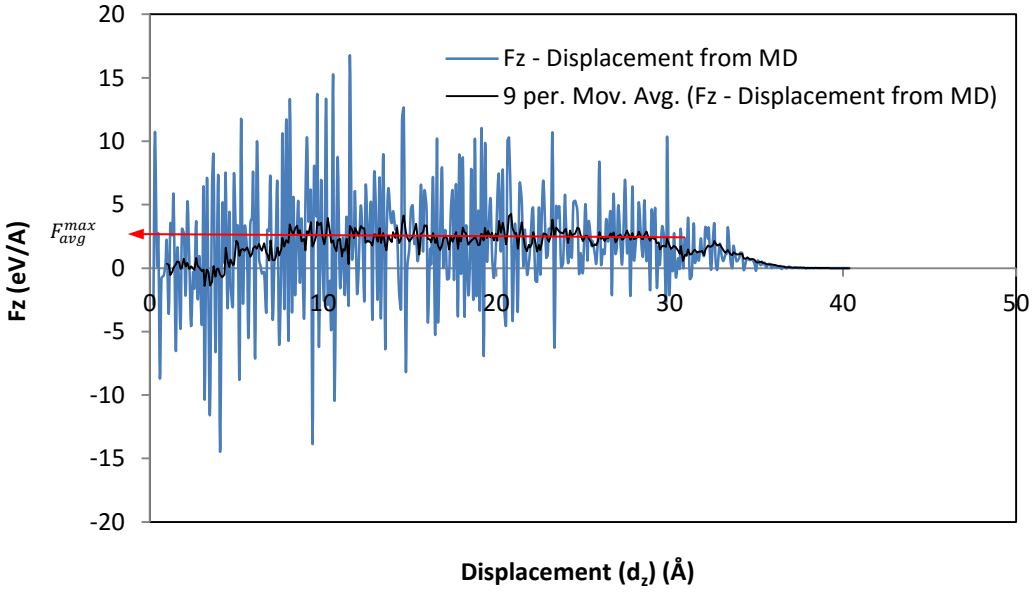

Fig. 41. Pull-out force – displacement curve in z-direction

Knowing τ_{max} and the accompanying displacement(Δu_s), where average force is first attained, bi-linear axial CZM could be given as shown in Fig. 42. Since the CZM is going to be employed in the micro-scale FE modeling, displacement at the separation (Δu_s^{sep}) is assumed to take place at the first breaking of C-Cu vdW interaction because this is the point instability starts at in the micro-scale. Then, shear stress (τ) drops down with the same slope as the slope of the pull-out force when it starts to decline at the end of pull-out in Fig. 41. Performing the $Favgmax$=2.5 ev/Å, a=2.1 Å and c=40 Å in Eqs. $Fz=\Delta EvdW\Delta dz$ Eq. 13 and $\tau_{max} = F_{avg}^{max} ca$. Eq. 14, τ_{max} is estimated ($\tau_{max=}$4.76 GPa). From Fig. 41, Δu_s and Δu_s^{sep} could be 8 Å and 18 Å, respectively.

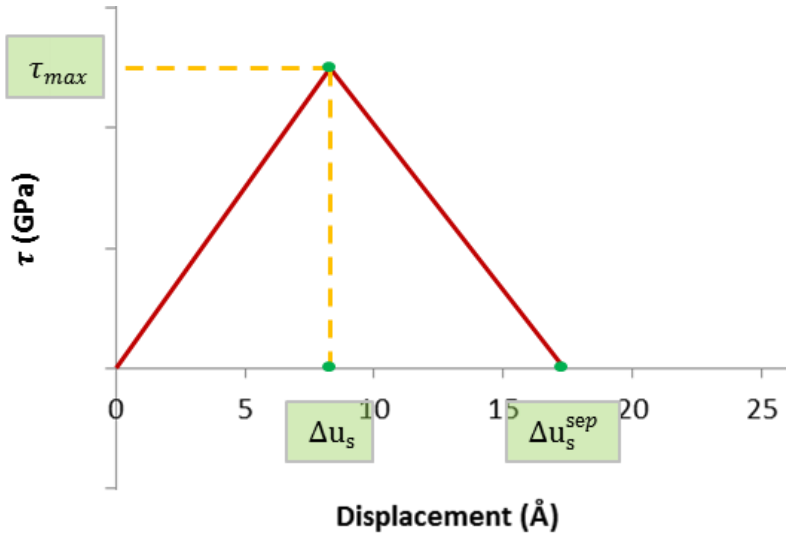

Fig. 42. Bilinear axial CZM

3.3.1.2 *Pull-out in the Normal Direction*

Force in this direction is hard to be evaluated in the same manner as the previous case, since the MWCNT atoms are not under the same conditions throughout the test. In this case the C-Cu separation takes place continuously and in a manner that a crack initiates and propagates, however in the previous case MWCNT is sliding over Cu surface and separation occurs in an intermittent manner. Moreover, as what will be discussed later in the squeezing effect part (Fig. 45), MWCNT is deformed more significantly that causes asymmetric C-Cu interactions for the C atoms inside the MWCNT. In the pull out test in axial direction however, the slip-stick behavior causes a periodic behavior which is inherently different from pull out in normal direction. During pull-out in y-direction in (Fig. 43), average stress was simply calculated for the atoms enclosed in the red box in Fig. 43. These atoms lie in C-Cu cut-off range where C-Cu vdW interaction is active.

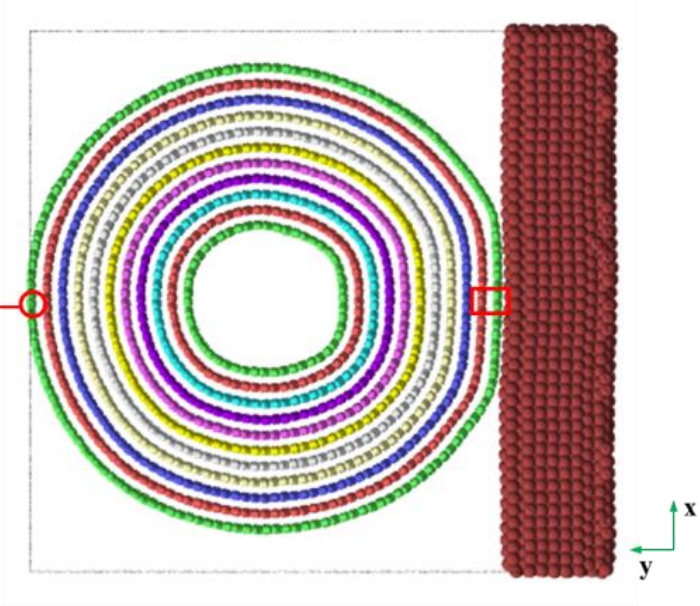

Fig. 43. Normal loading of MWCNT

Furthermore, they have the same magnitude and direction of displacement throughout the pull-out test. In MD, atomic stress (virial stress) could be extracted. As concluded from chapter 3 and a previous study [105], since stresses were time averaged for all times and no periodic boundary conditions in the stress calculation direction (y-direction) is activated, mechanical stress could be represented by virial stress when kinetic part is ignored and it is given in

$$\sigma_{ij} = \frac{1}{V}\sum_{\alpha \in V}\left[\frac{1}{2}\sum_{\beta=1}^{N}\left(r_i^{\beta} - r_i^{\alpha}\right) f_j^{\alpha\beta}\right] \qquad \text{Eq. 2.}$$

Normal stress (σ) – displacement curve (Fig. 44) was extracted from MD simulation. Compressive stress increases as the MWCNT is pulled out due to the inter-tubular effect. Fig. 45 illustrates the squeezing effect behind the compressive stress; the more the MWCNT strand is pulled out, the more it is squeezed and the inner walls push the outer walls further towards Cu causing increased compressive stress. After this squeezing effect vanishes, compressive stress decreases and tensile stress increases due to pull out. Tensile stress increases until normal strength (σ_{max}) is attained and then stress drops down rapidly until separation is

detected when C-Cu vdW interaction becomes 0 eV when C-Cu finite distance (σ= 3.088 Å) is attained Fig. 45. This takes place at a separation displacement ($d_{y,}$ in this case,=5.8 Å); however, stress is not zero at this point (Fig. 44) because there is some compressive stress due to the inter-tubular squeezing effect that will be discussed later.

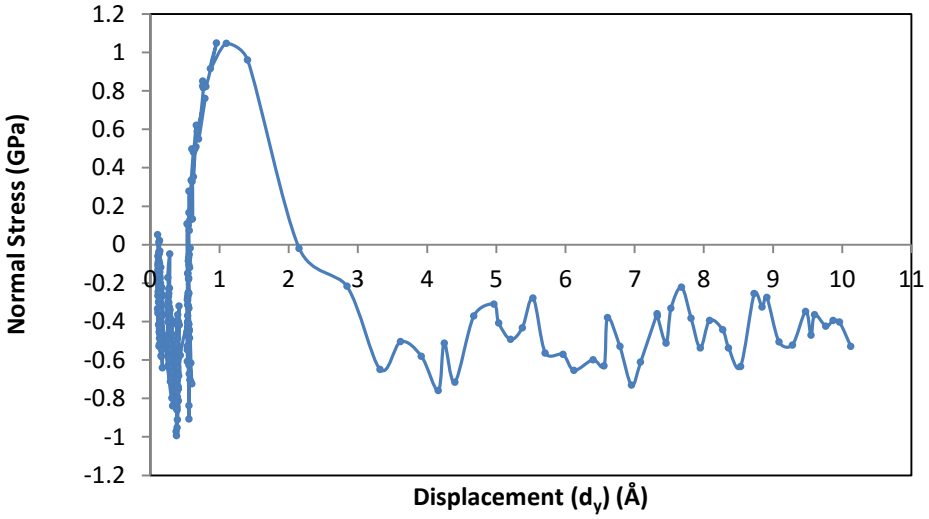

Fig. 44. Normal stress – displacement curve

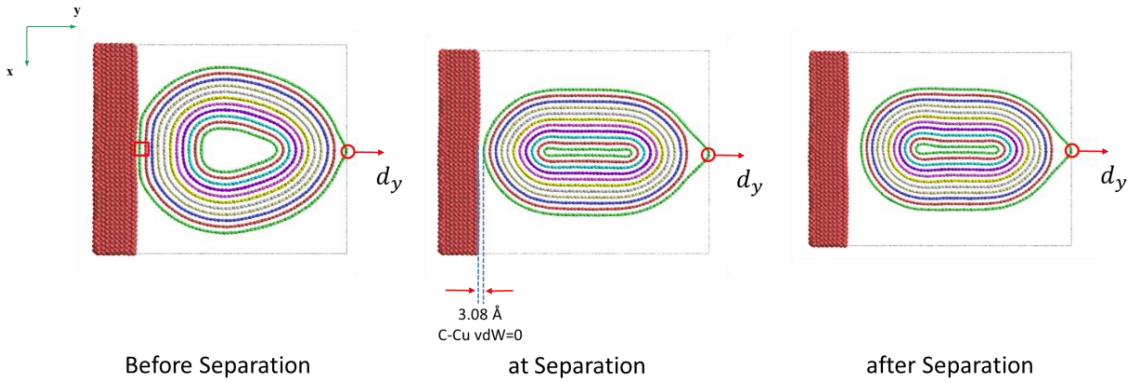

Fig. 45. Squeezing Effect

The compressive stress here is also believed to be a result of squeezing effect. As depicted in Fig. 45, even after separation, the MWCNT strand stays squeezed and there is some

compressive stress residue remaining. This compressive stress decreases gradually after separation (at 5.8 Å) as shown in Fig. 44 because the strand is trying to retain its cylindrical configuration.

Now, bilinear normal CZM could be assumed, for simplification, to be in the form shown in Fig. 46 such that $\Delta u_n^{sep} = 5.8$ Å. Here, Δu_n^{sep} is not attained at 0 stress as expected in Fig. 42 due to the squeezing effect and the squeezing effect is ignored in CZM prediction.

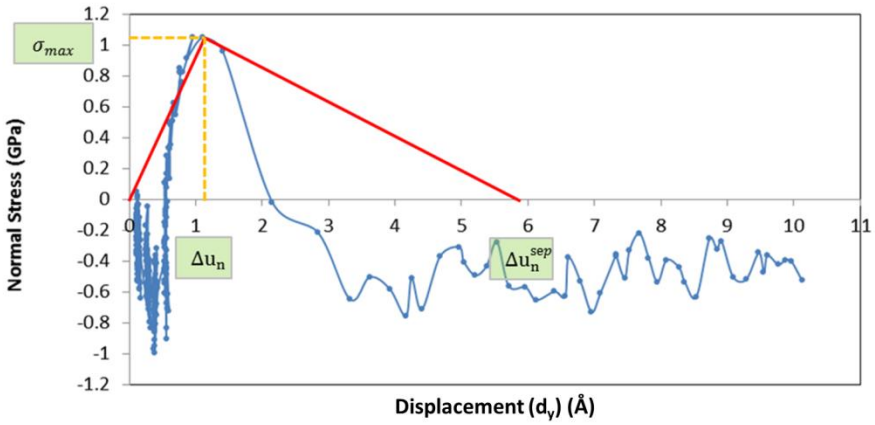

Fig. 46. Bilinear normal CZM

The effect of number of layers on the strength of the interface in nanotube is found to be insignificant [87]. The effect of chirality's is also assumed in substantial as the strength is believed to be influenced by Carbon atoms at proximity of Cu. Thus, CZM Parameters to be used in FE to describe the contact elements properties are summarized in Table 4.

Table 4: Summary of CZM parameters

Axial CZM		**Normal CZM**	
τ_{max}	4.76 GPa	σ_{max}	1.04 GPa
Δu_s	8 Å	Δu_n	1.1 Å
Δu_s^{sep}	18 Å	Δu_n^{sep}	5.8 Å

3.3.2 *FE Results*

Extracted CZM parameters from Table 4 are then used in a continuum level finite element models. Mechanical behavior of CNT/Cu-TSV is examined by applying two distinct loading scenarios; bending and thermal cyclic loading scenarios.

3.3.2.1 *Bending Scenario*

In the three-point bending case, the contact status was tracked throughout loading. Fig. 47 shows CNT/Cu contact status near the bottom of CNT/Cu contact at different steptimes. Separation took place when maximum deflection (D_{max}) was 46.2 μm and total mechanical strain in x-direction ε_x was 0.144 near the bottom of Cu. Deflection increased rapidly until separation took place at t=92.0763 s. After this instant, deflection slowly increased, whereas separation (FarOpen area in Fig. 47) propagated rapidly. This implies that the load was no longer transferred to the TSV to cause deflection. Rather, the load was transferred to the CNT/Cu interface to promote the separation near the bottom of the interface. At t=92.0763 s, FarOpen area lies between z= 15 μm and z = 25 μm from the bottom of the CNT/Cu interface and at the both sides. At that time, separation takes place.

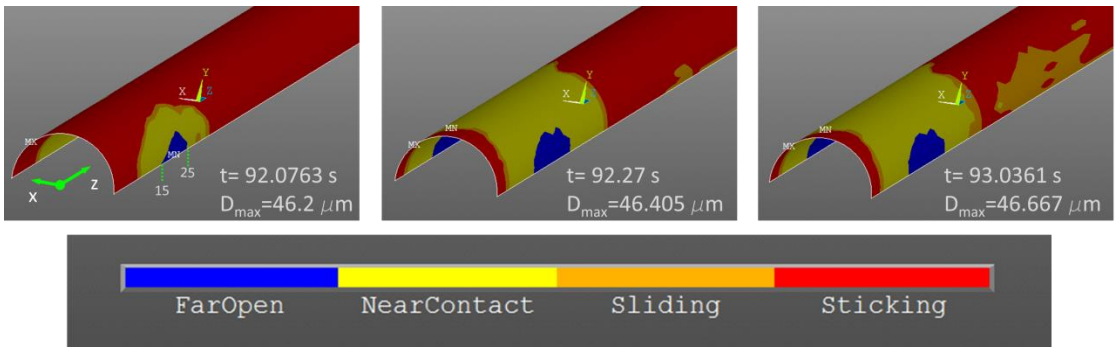

Fig. 47. Contact status near the bottom of CNT/Cu interface before, at and after separation instant

The occurrence of separation at that location requires some study of the deformation at the instant right before separation in order to define the causes of separation. Fig. 48-a—side view of the contact element—shows the contact status at the instant right before separation (t=92.075 s and D_{max}=46.19 μm). Fig. 48-b is a side view of the distribution of the displacement in x-direction (U_x) of the CNT/Cu-TSV. The graph in Fig. 48-c indicates the distribution of U_x along the path shown in Fig. 48-b. This path is at the passes through the CNT/Cu interface at the location shown in the figure. As depicted from Fig. 48-c, NearContact zone—weak zone—lies between z = 8 and z = 33 μm where there is a big difference between in U_x between CNT and Cu. Moreover maximum U_x is attained at z =25 μm and that is where separation took place in Fig. 47. The displacement in Cu in this portion is so high compared to CNT due to the big difference between the tangent modulus of Cu (517.8 MPa) and Young's modulus of the CNT bundle (1 TPa). The difference in displacement is a clear indication of separation.

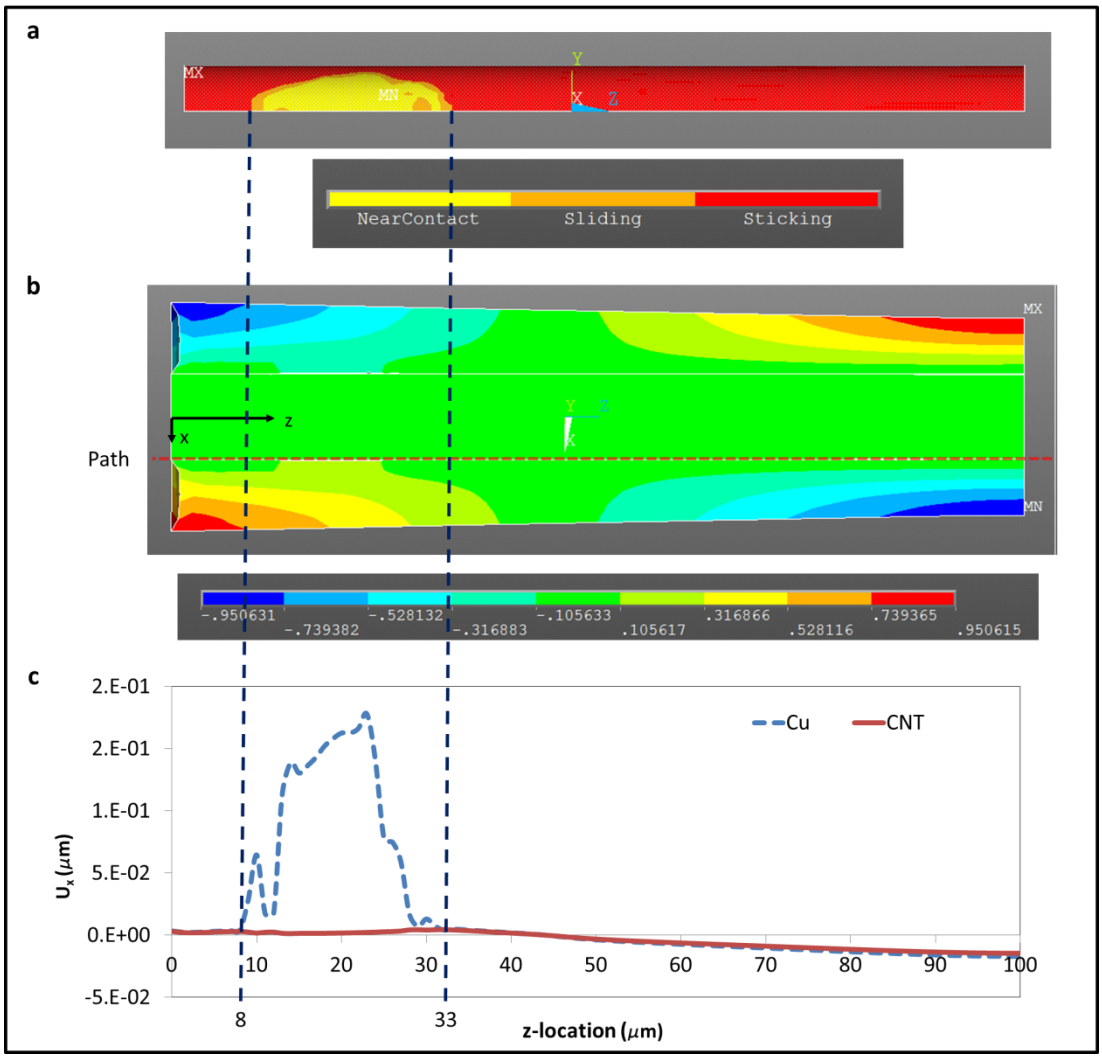

Fig. 48. [a] Side view of the contact elements; [b] top view of U_x in CNT and Cu; [c] U_x distribution along the dashed line path

Maximum stresses were also studied at the instant of separation in order to check if failure due to maximum stresses took place (Fig. 49). Maximum stress in Si was found to be 13.9 GPa which exceeds Si's UTS (7 GPa). This means that failure in Si occurs prior to CNT/Cu separation. CNT's UTS is 100 GPa and it was not exceeded. Maximum stress in Cu was found to be 380 MPa which exceeds the Yield strength (210 MPa). So, Cu continues to deform

plastically. Although failure occurred in Si, CNT/Cu interface is able to endure substantial deformations.

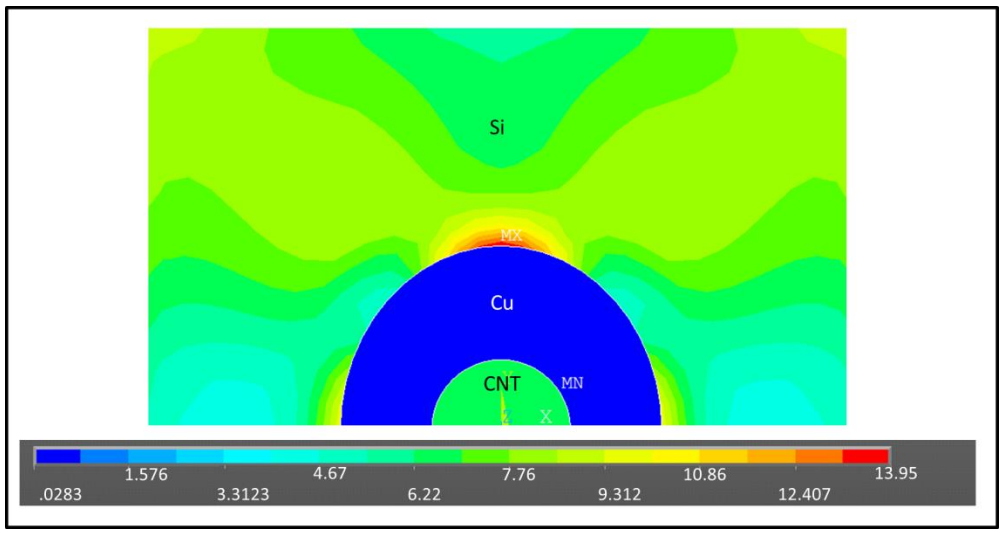

Fig. 49. von Misses Stress (GPa) at the top of the TSV at instant of separation

In order to understand the actual difference that can happen on a case where only Cu is used, a model was developed with only Cu filling the TSV. Plastic deformation started exactly at the same displacement value for both cases (D_{max}=1.43 μm). Equivalent plastic strain (EPS) in the CNT/Cu-TSV (0.78E-3) is higher than Cu-TSV (0.25E-3) when D_{max}=1.43 is attained for both cases at the top of the TSVs as shown in Fig. 50. Both maxima occur at the top of the TSV which is exposed to compression in both cases and it is higher in the CNT/Cu case because of the high stiffness of CNT bundle that promotes the compression of Cu. Therefore, in terms of plastic deformation of Cu, Cu-TSV can sustain larger displacements.

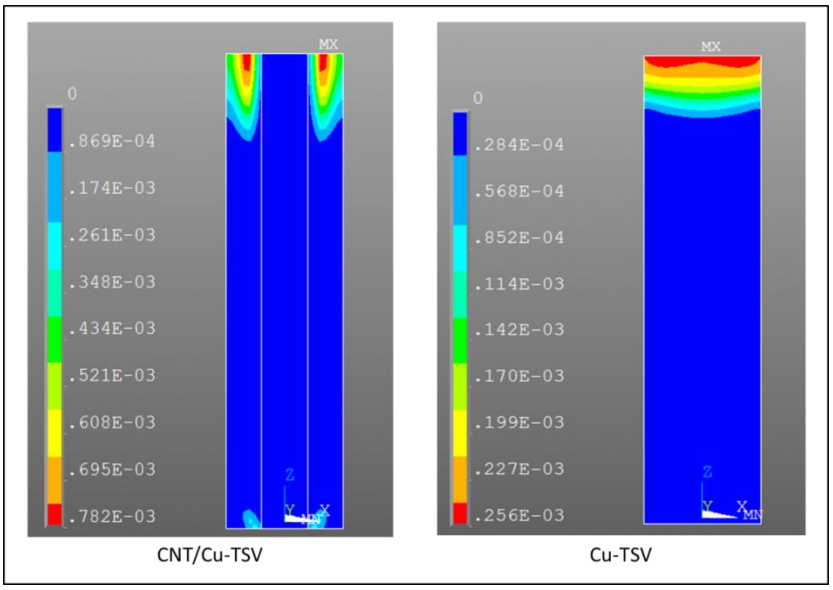

Fig. 50. EPS at the initiation of plastic deformation

3.3.2.2 *Thermal Cyclic Load Scenario*

When thermal cycle was applied (Fig. 19), separation never took place. However, interesting behavior was observed during loading. Fig. 51 shows ε_x when the maximum temperature was attained (398 K°). Die attach and substrate possess CTE values that are much higher than those of CNT and Si in the TSV layer. Therefore, TSV layer tends to bend causing tensile bending at the bottom of the TSV and compressive bending at the top. Furthermore, Cu's CTE is the highest amongst all and it expands and mostly shows positive strain during heating up as shown in Fig. 51. Thus, Cu pushes Si away due to the mismatch in CTEs but, meanwhile, Si is bent under the effect of CTE mismatch between the different layers; Si, underfill and substrate. Bending facilitates Cu expansion at the lower parts of the TSV where tensile bending exists and counteracts Cu expansion at the higher part where compressive bending exists. That explains the compressive strain conical contour profile formed around the TSV in Fig. 51.

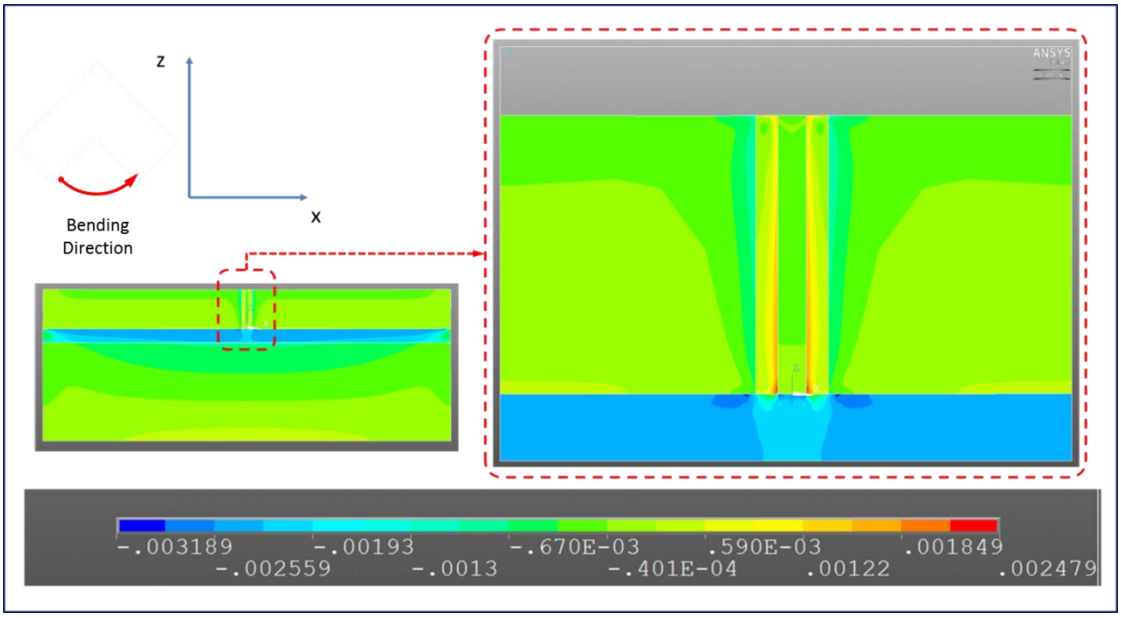

Fig. 51. ε_x distribution at 398 K°

Fig. 52 shows the strain distribution along the Si/Cu interface (at the Si surface) where total compressive strain increases moving from the bottom to the top of the TSV and the maximum value of -1.1E-3 occurs near the top. Meanwhile, maximum tensile strains occurs at the Cu/CNT (at the Cu Surface) interface due to the CTEs' mismatch since CNT has negative CTE values during heating as shown in Fig. 21 and Cu's CTE is always positive. Consequently, the interface is exposed to tensile strains and they decrease gradually as going upwards from the bottom to the top of the TSV by the bending effect in the direction shown in Fig. 52. Maximum tensile strain of 2.1E-3 was obtained at the bottom of the Cu/CNT interface.

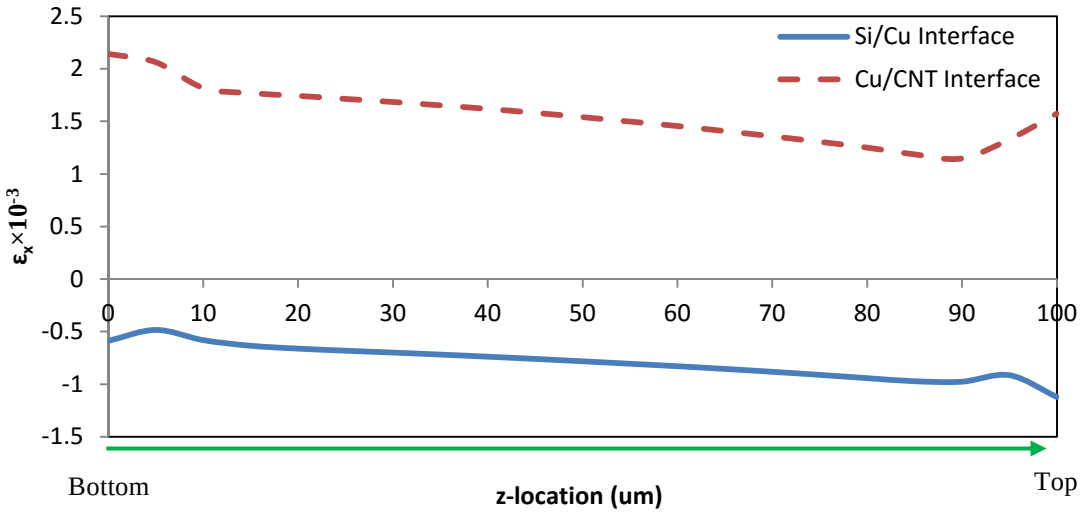

Fig. 52. ε_x distribution at the Si/Cu interface and Cu/CNT interface from the bottom to the top of the TSV 398 K°

Next, the results when the temperature went down to 233 K° are discussed. Evidently from Fig. 53, the results are typical inversion of the results in Fig. 51 since the layers are bent in the other direction due to the CTEs' mismatch and Cu is contracting instead of expanding. Apparently, CNT bundle expands during cooling down (Fig. 21) and this expansion compresses the Cu part causing compressive strains at CNT/Cu interface. Meanwhile, Cu contracts due to cooling down pulling the Si at the Cu/Si interface towards it. Under the effect of bending—due to the CTE mismatch between the different layers—and the Cu pulling effect, Si at the Si/Cu interface experiences more tensile strain. Bending causes Cu contraction at the lower parts of the TSV where compressive bending exists and counteracts Cu contraction at the higher part where tensile bending exists. That combined effect explains the tensile strain conical contour profile around the CNT/Cu-TSV in Fig. 53.

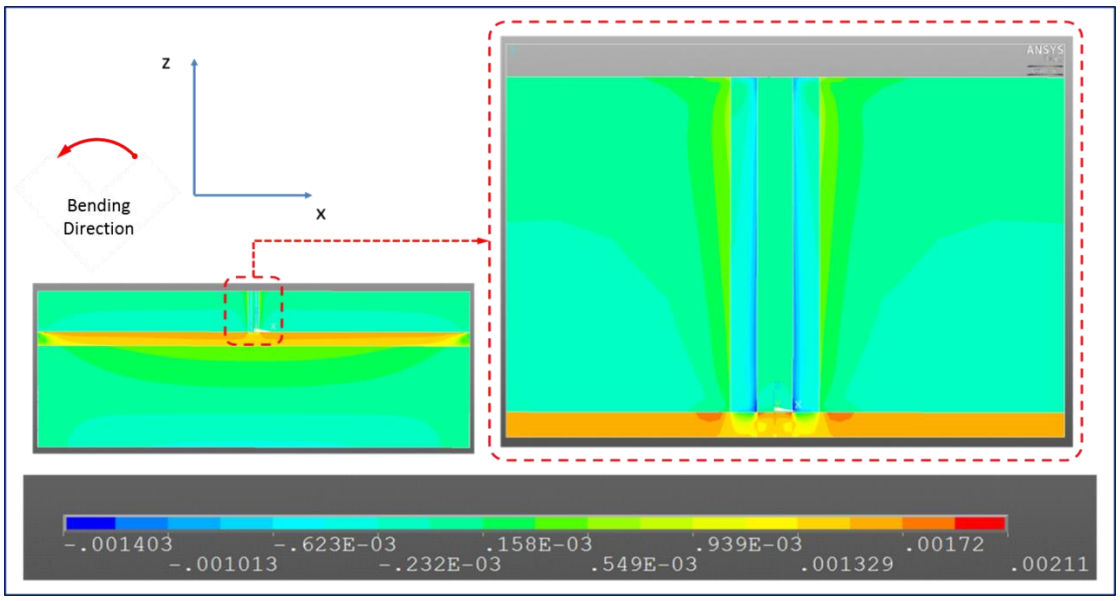

Fig. 53. ε_x at 233 K°

Fig. 54 shows the strain distribution along Si/Cu interface (at the Si surface) and Cu/CNT interface (at the Cu surface). The results appear to be also an inversion of the results shown in Fig. 52. Maximum tensile strains take place at the Si/Cu interface (at the Si surface) where total tensile strain is increasing moving from the bottom to the top of the TSV and the maximum value of 0.693E-3 occurs at the top. In the contrary, maximum compressive strains occur at the Cu/CNT interface (at the Cu surface) due to the CTE mismatch between Cu and CNT since Cu contracts and CNT expands during cooling down. The compressive strain decreases gradually from the bottom to the top of the CNT/Cu interface due to the bending in the direction shown in Fig. 53 induced by the CTE mismatch between the different layers. Maximum compressive strain occurs at the bottom of Cu/CNT interface (ε_x=-1.3E-3). Thus, maximum tensile and compressive strains in x-direction occur at the bottom of the CNT/Cu interface after heating up and cooling down, respectively.

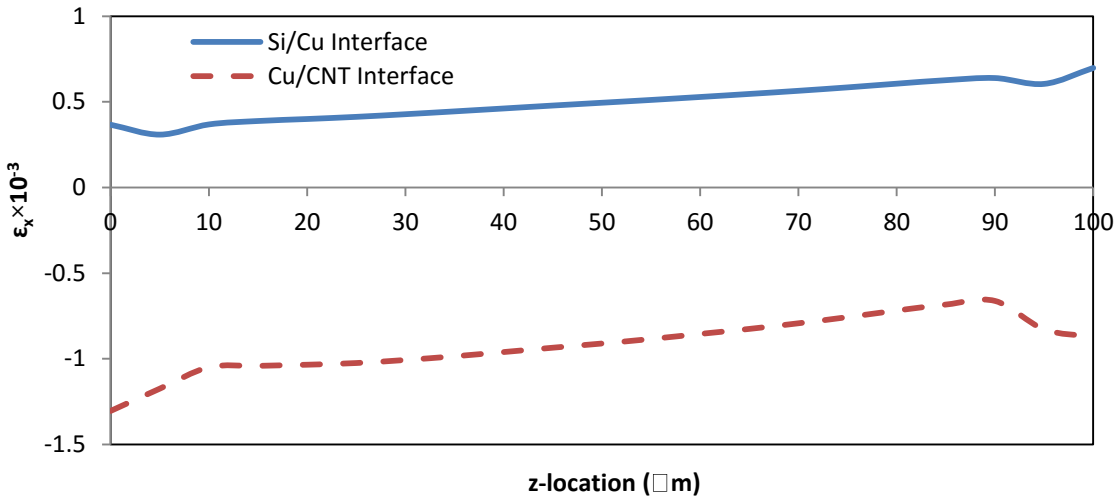

Fig. 54. ε_x distribution at the Si/Cu interface and Cu/CNT interface from the bottom to the top of the TSV at 233 K°

Maximum stresses were also studied to make sure that failure did not take place due to maximum stresses during the thermal cycle (Fig. 55). The highest stresses occurred at 398 K°. Maximum stresses in CNT and Si are 462 MPa and 290 MPa, respectively. Thus, neither CNT's Yield Strength (100 GPa) nor Si's UTS (7 GPa) has been exceeded. However, maximum stress in Cu is 202 MPa which is higher than Cu's Yield strength and that means that plasticity occurred in Cu.

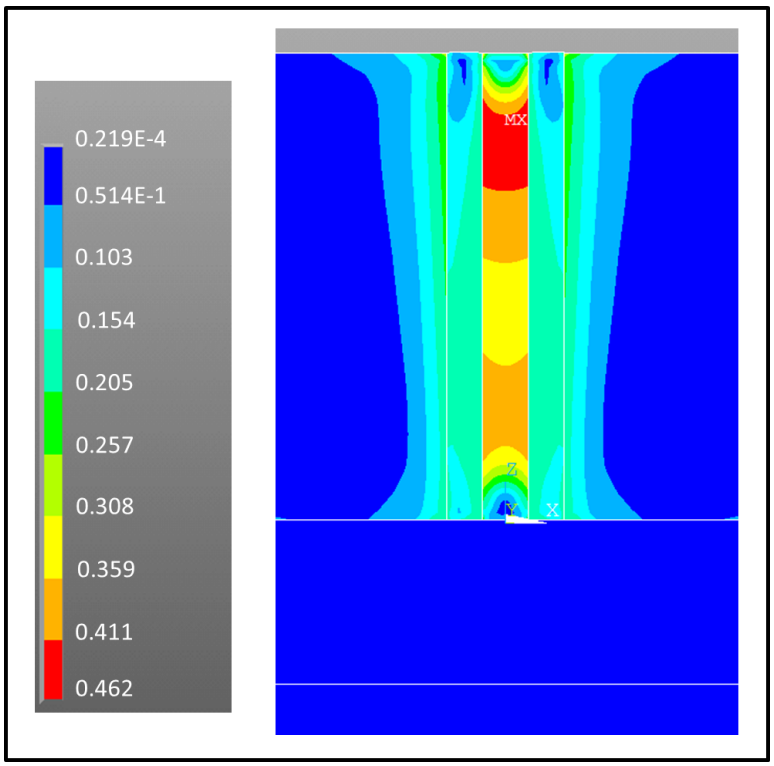

Fig. 55. von Misses Stress (GPa) distribution at 398 K°

Since plastic deformation occurred in Cu, plastic strain is of concern because it provides an indication of the TSV potential failure locations. At the end of the temperature cycle (298 K°), EPS in Cu is studied. From Equivalent plastic strain distribution shown in Fig. 56, very high plastic deformations take place around the bottom and the top of the CNT/Cu interface and the maximum locates at the top. From the plastic strain distribution, it could be said that deformation is caused by consequent, cyclic bending and promoted by the mismatch between CNT's and Cu's CTE values. Heating up took place two times; from 298 to 398 K° and from 233 to 298 K°. That explains that occurrence of the maximum plastic (≅0.73E-3) deformation at the top since it was exposed to tensile bending twice.

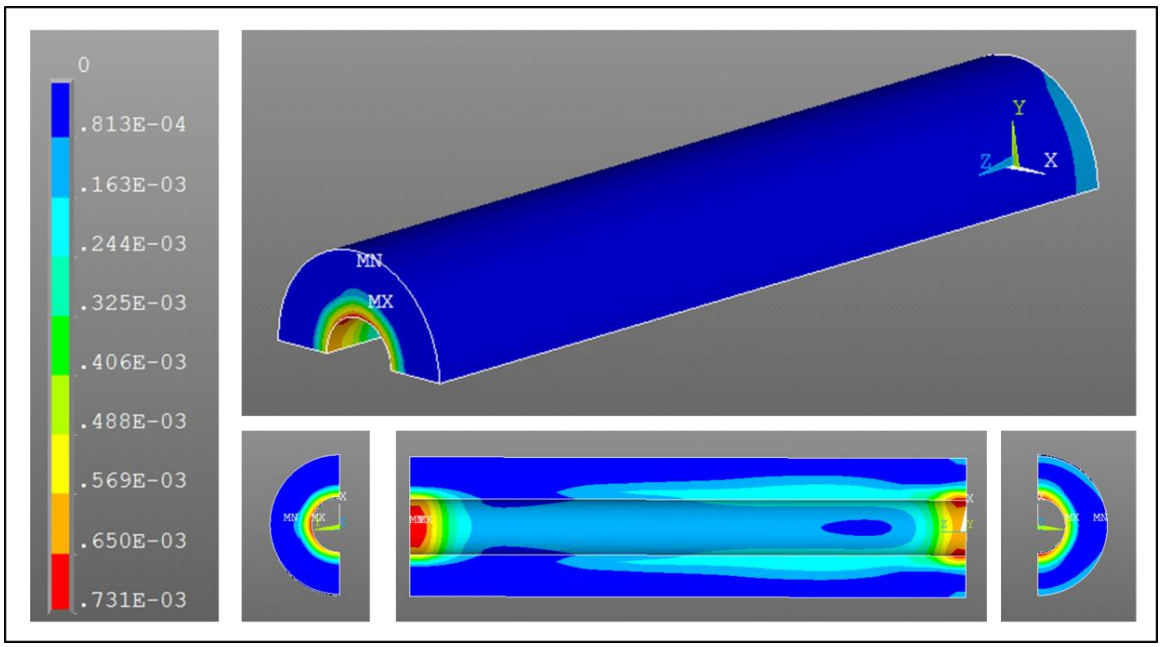

Fig. 56. EPS distribution in Cu at the end of the temperature cycle of CNT/Cu-TSV

The previous results are compared to Cu-TSV. At the end of the temperature cycle, plastic deformation occurred at the top and the bottom of Cu/Si interface and EPS has a maximum value (0.22E-3) at the bottom of the TSV as shown in Fig. 57. Maximum EPS in this case is less than the CNT/Cu-TSV (0.73E-3); however, both cases reached plasticity. Plastic deformation occurred at the top and the bottom of the Cu-TSV at the Cu/Si interface. Presumably, CNT's negative-sign CTE shifted the plastic deformation away from Cu/Si interface in the CNT/Cu-TSV case.

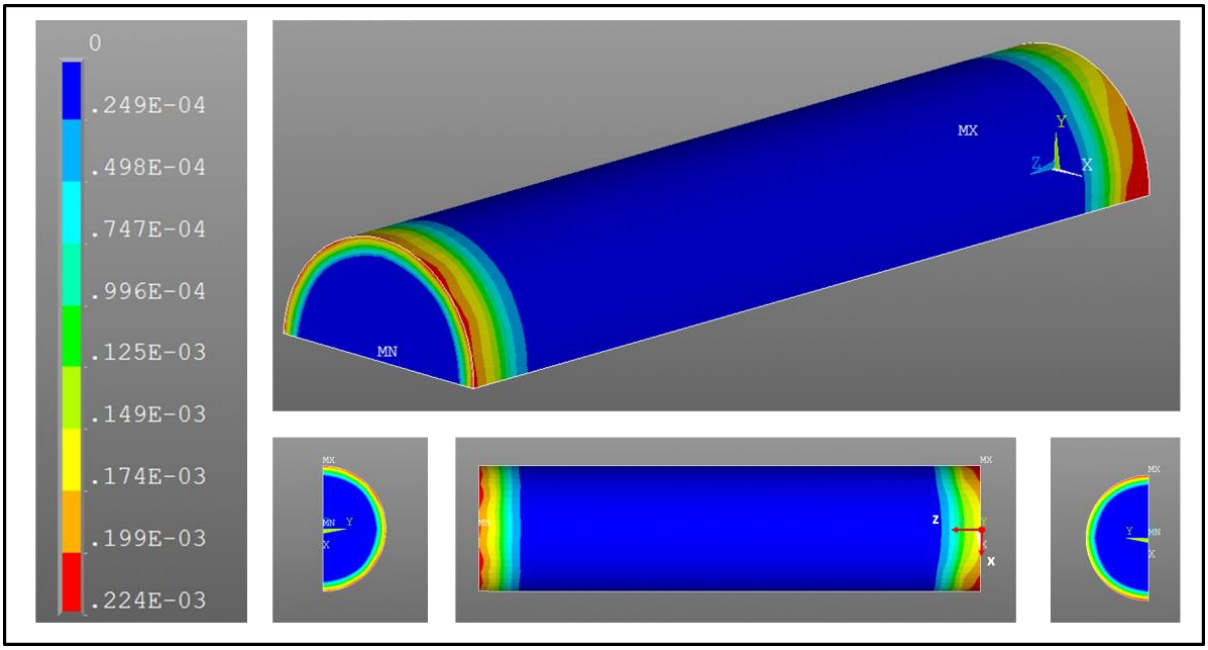

Fig. 57. EPS distribution in Cu at the end of the temperature cycle of Cu-TSV

3.4 Fatigue Life Expectancy

The previous multiscale model approach is modified to provide a more accurate estimation of the fatigue life of CNT/Cu-TSV. CNTs are nature specific. Their properties vary with their chirality, number of walls and temperature. Therefore, stress-strain behavior and CTE of the selected MWCNT in Fig. 12 have been evaluated and the extracted properties along with the previously defined CZM have been used in the finite element analysis.

3.4.1 *Molecular Dynamics Results*

3.4.1.1 *Stress-Strain Behavior*

The resulted stress-strain curve is shown in Fig. 58. Stress increases non-linearly until ε becomes 0.27, then it starts increasing rapidly until Ultimate tensile strength (UTS=233 GPa) is attained at $\varepsilon = 0.34$. At this point, crack initiates at the outer wall's surface and propagate

until the outer wall is entirely broken. Then, the other walls break in the same manner subsequently while stress is dropping rapidly to 0 GPa when complete rapture takes place.

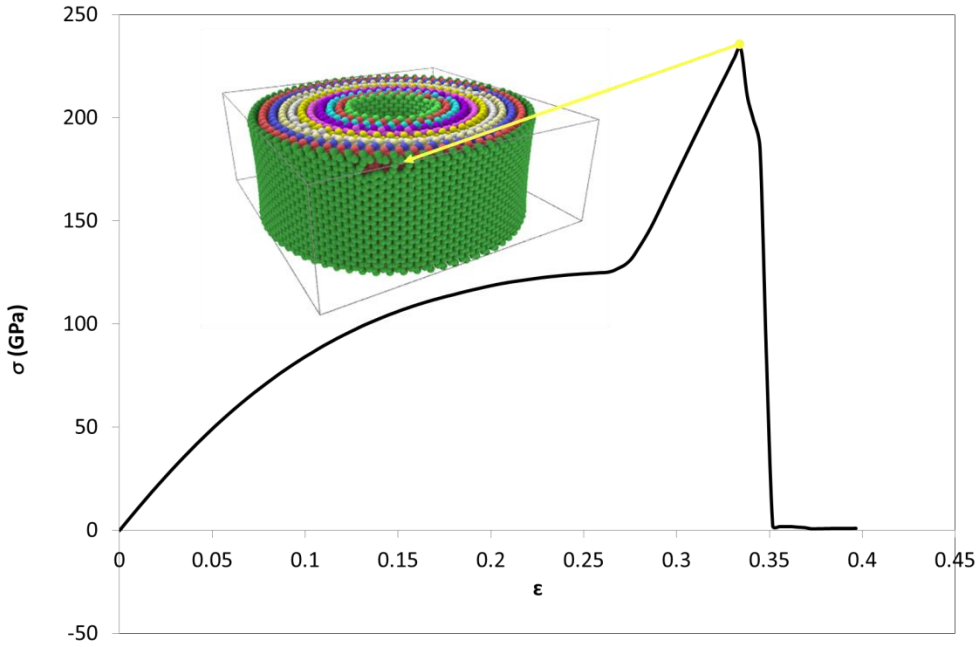

Fig. 58. Stress-strain curve

For stress-strain behavior of CNT bundle, the obtained curve (Fig. 58) is fitted to the cubic Yeoh's hyper-elastic model [106] in ANSYS (Eq. 15) which gave the best curve fitting (Fig. 59).

$$W = \sum_{i=1}^{3} C_{i0}(I_1 - 3)^i \qquad \text{Eq. 15}$$

In this model, strain-energy density (W) is given as a polynomial of first strain invariant (I_1). In the uniaxial loading case, I_1 is given as $I_1 = \lambda^2 + \frac{2}{\lambda}$ such that λ is the principal extension ratio in the axial direction. Accordingly, the strain is given by $\lambda - 1$ and the uniaxial stress-strain relationship will be given by (Eq. 16) such that C_{i0} is a material constant and it took the values 181.6 GPa, -487.6 GPa and 1023 GPa.

$$\frac{\sigma}{\lambda-\lambda^{-2}} = 2\frac{\partial W}{\partial I_1} = 2C_{10} + 4C_{20}(I_1 - 3) + 6C_{30}(I_1 - 3)^2 \qquad \text{Eq. 16}$$

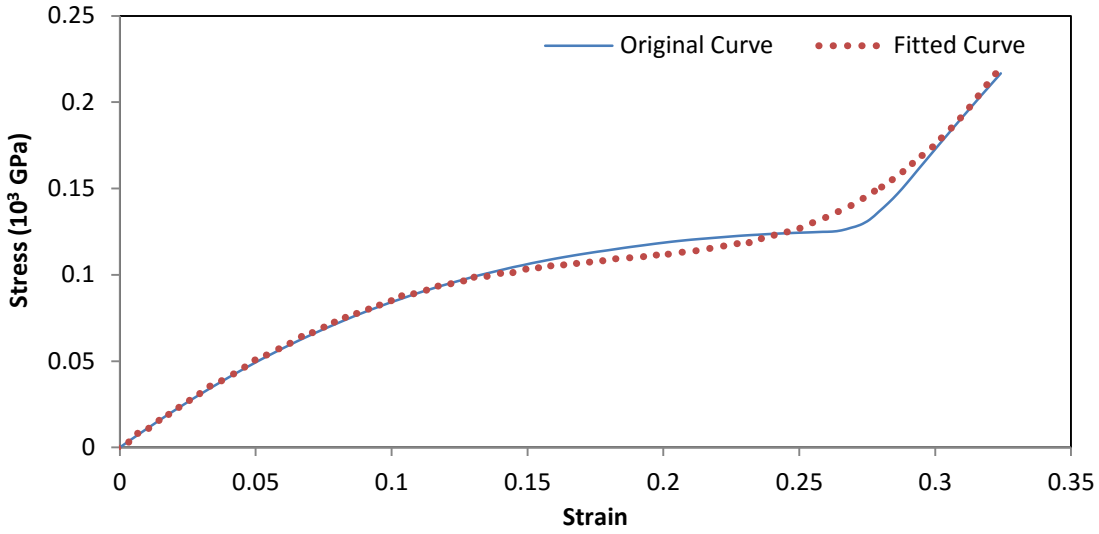

Fig. 59. Yeoh's curve fitting

3.4.1.2 *CTE*

The results are shown in Fig. 60. Radial and axial CTE are different in magnitude. CTE in radial direction is almost an order of magnitude larger than the CTE in axial direction. This difference is caused by the difference between the bond lengths and angles in the axial and the radial directions. Researchers have reported negative CTE values at low temperatures for SWCNT [91,107–110]. However, the obtained values depend on the chirality of the CNTs. Furthermore, it was found that the axial CTE curve moves up as the number of walls increases as shown in Fig. 61 from [111]. As seen in this figure, the CTE is initially negative at small number of walls and it slowly surpasses zero as the number of walls are increasing. If negative values of CTE could be called thermal contraction, rather than thermal expansion, increasing the number of walls suppresses the thermal contraction and initiates a thermal expansion Thus, the thermal contraction in the current case of 11-wall MWCNT is entirely suppressed and

CTE_a has positive values as shown in Fig. 60. Furthermore, CTE results shows dependence on temperature at low temperature (<200 ^oK) while there is insignificant dependence at higher temperatures (>200 ^oK).

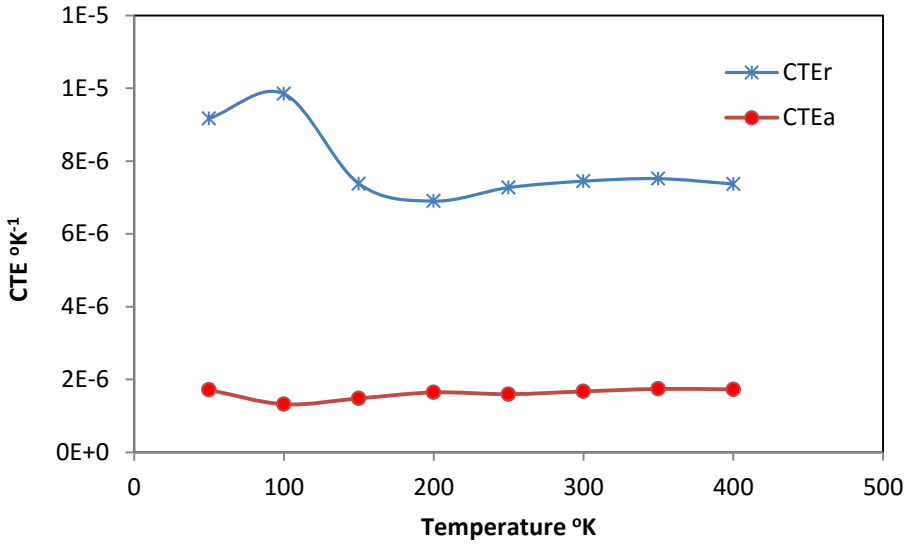

Fig. 60. Radial and axial CTEs

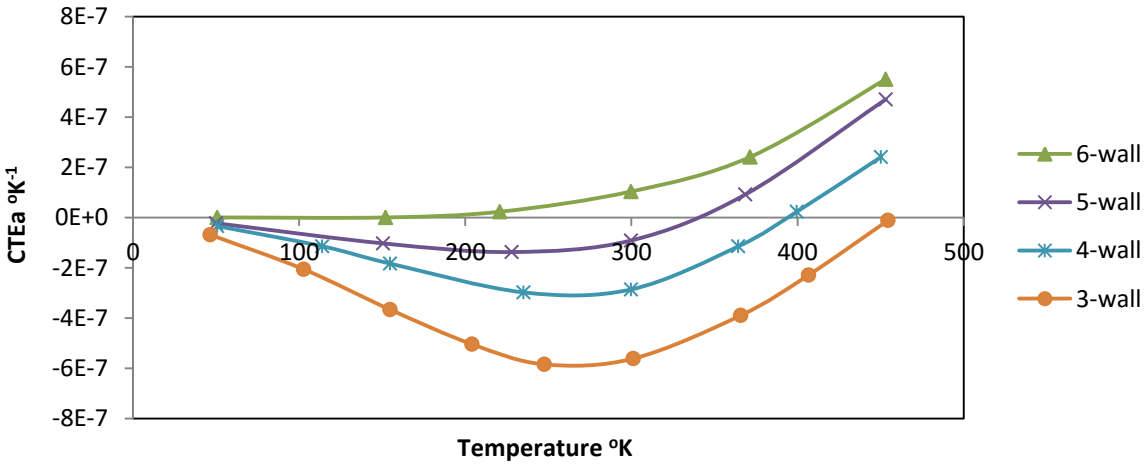

Fig. 61. Axial CTE reconstructed using data from [111]

3.4.2 *FE Results*

Failure in the current CNT/Cu-TSV may take place because of separation of CNT/Cu interface or excessive plastic deformation of Cu. Due to the CTE's mismatch of the different components of the model; Si, CNT, Cu, die attach and substrate, the TSV experience directional alternating bending during consequent heating-up and cooling-down processes [112]. Thus, that may result in the separation of the CNT/Cu-interface. The results of the FE analysis did not show any separation of the CNT/Cu-interface at any point during the cyclic loading. However, plastic deformation of Cu is of concern in this study in order to estimate the fatigue life. EPS is a key parameter in the estimation of the fatigue life. Therefore, Fig. 62 depicts the EPS distribution in Cu. Maximum values are attained at the CNT/Cu and Si/ Cu interfaces.

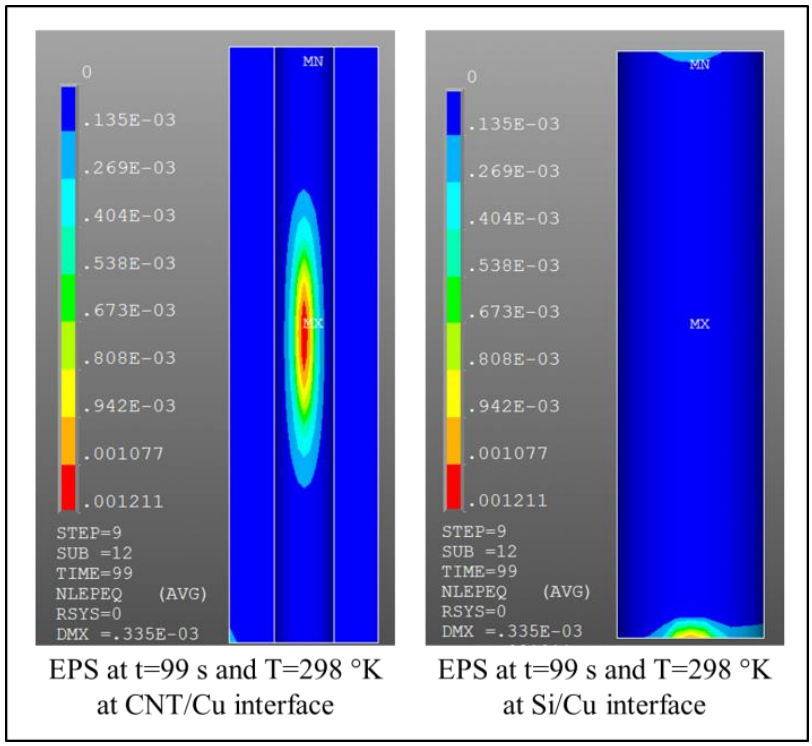

Fig. 62. EPS distribution in Cu

Investigating the total von Misses strains (Fig. 63) after the end of the heating-up (T=398 °K, t=76 s) and cooling-down (T=233 °K, t=92.5 s), maximum strains takes place at the location of maximum EPS. Cu's CTE is one order of magnitude higher than CNT's radial CTE and Si's CTE. Therefore, maximum strains took place in Cu at the CNT/Cu and Si/Cu interface during the thermal cycle. Moreover, there is maximum value at the bottom at the Cu/Si interface due to the interfacial strains mismatch and the consequent bending of the structure.

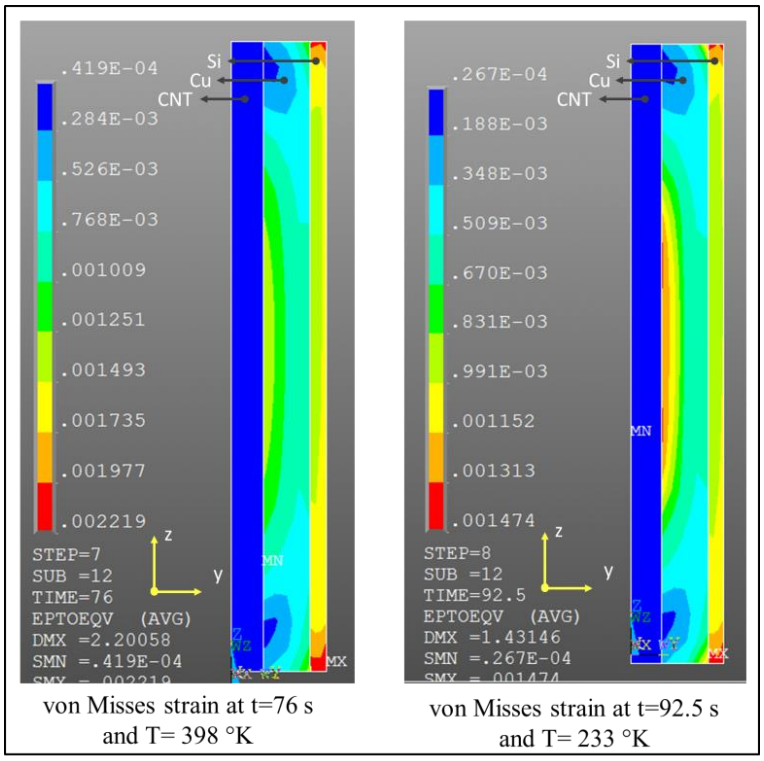

Fig. 63. Cross-section of the EPS distribution in CNT,Cu and Si

Pressure distribution at the contact elements also shows the great effect of CNT and Cu CTE mismatch. High tension and compression occur after heating-up (T=398 °K and t=76 s) and cooling-down (T=233 K° t=92.5 s), respectively as shown in Fig. 64.

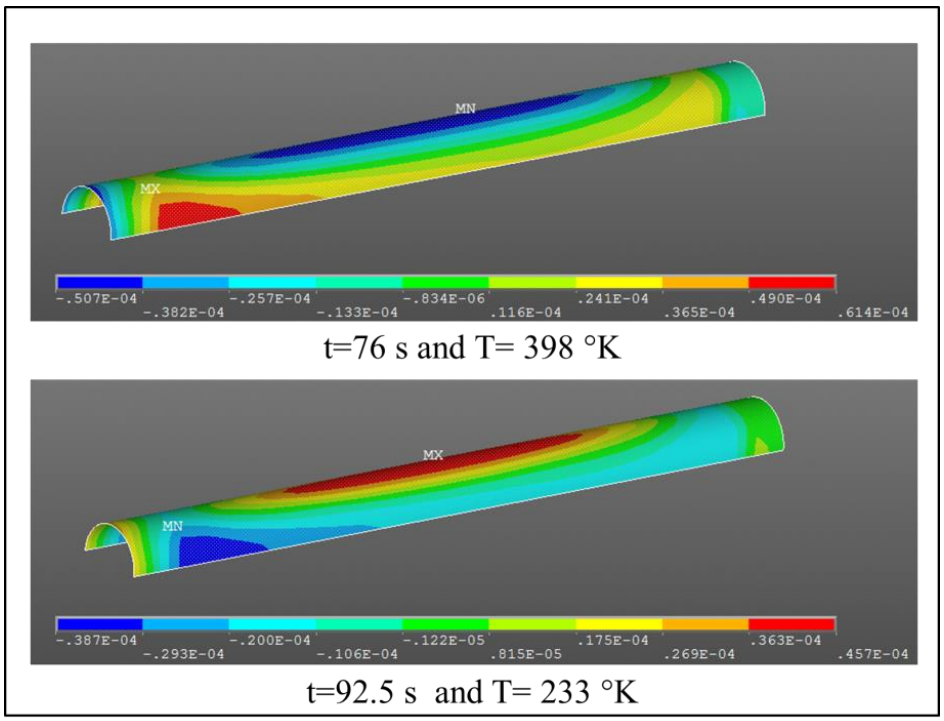

Fig. 64. Contact pressure at CNT/Cu-interface (×10^6 MPa)

For fatigue life estimation, $\Delta\varepsilon_f$ is related to the number of fatigue cycles N_f through Coffin-Manson relation ($\Delta\varepsilon_f = {\varepsilon_f}^{0.75}{N_f}^{c_3}$) such that $\Delta\varepsilon_f$ is the stabilized EPS amplitude, the EPS change between the end and the beginning of a thermal cycle, ε_f is the ductility of Cu at fracture and c_3 is the fatigue ductility exponent [113,114]. From the EPS distributions in Cu (Fig. 62), maximum values takes place at two locations; at the CNT/Cu interface and at the Cu/Si interface, which requires investigating which location acquires the maximum EPS change ($\Delta\varepsilon_f$) so as to appropriately estimate the fatigue life. In order to determine how EPS changes over the simulation time, EPS values are calculated for the elements in the vicinity of the maximum EPS locations (located at CNT/Cu and Si/Cu interfaces) by taking the average of the elements that lie in this vicinity so that any error due to mesh size optimization could be mitigated as much as possible, and a plausible fatigue life estimation could be resulted

accordingly. The elements to be taken the average of are chosen carefully in a way that assures that they surround the node that experiences the maximum EPS, and that EPS values do not vary wildly. Since the region of maximum EPS in Cu at CNT/Cu interface is larger than that at Si/Cu interface (Fig. 62), eleven elements that attain the maximum eleven EPS values are chosen at the CNT/Cu interface, while five elements are chosen at the Si/Cu interface. Then, the average of the EPS values is taken at each time-step to extract the average EPS-time behavior at the two vicinities where the maximum values occur in Cu. Fig. 65 shows average EPS change over the simulation time at the two locations of interest. Maximum EPS takes place at CNT/Cu interface throughout loading. However, the accumulation of plastic strain, which is the change in EPS is of concern for the fatigue life estimation. Therefore, the change of EPS in the final cycle is taken into consideration for fatigue life estimation since $\Delta\varepsilon_f$ after this point stabilizes. From the results, $\Delta\varepsilon_f$ at CNT/Cu (0.2×10^{-3}) is higher than that is at Cu/Si-interface (0.18×10^{-3}). Therefore, the results at CNT/Cu-interface are going to be accounted for in the fatigue life estimation.

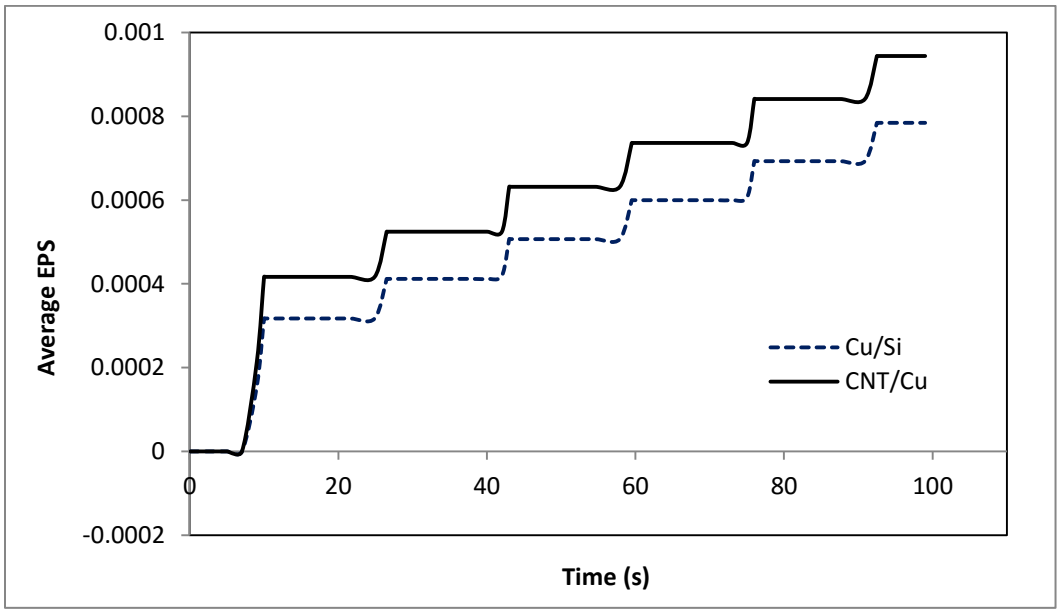

Fig. 65. Average EPS-Time in CNT/Cu-TSV

To have a control case for comparison, the same thermal cycle was applied to the Cu-TSV. In contrast with CNT/Cu-TSV, EPS took place in Cu at the Si/Cu interface as shown in Fig. 66.

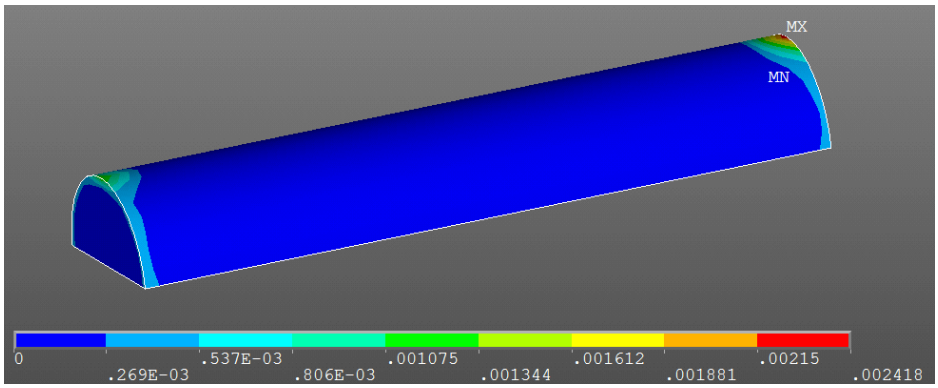

Fig. 66. EPS distribution in Cu

EPS is also calculated in the same way as CNT/Cu-TSV case. Fig. 67 shows average EPS change over time in CNT/Cu-TSV (at the CNT/Cu interface) and Cu-TSV (at Cu/Si interface). Average EPS is always higher in Cu/TSV case. Adding CNTs in the CNT/Cu-TSV case dislocated the maximum EPS away from the Cu/Si-interface to CNT/Cu-interface (Fig. 62) because it reduced the overall thermal expansion and contraction of the CNT/Cu-composite with respect to Si that has CTE one order of magnitude less than Cu. Thus, the mismatch between the CNT/Cu-composite and Si is reduced in the CNT/Cu-TSV case. In the current study, the plastic strain amplitude ($\Delta\varepsilon_f$) is the EPS change between the beginning (t=66 s) and the end (t=99 s) of the final cycle. $\Delta\varepsilon_f$ values are 0.2×10^{-3} and 0.404×10^{-3} for CNT/Cu-TSV and Cu-TSV, respectively. Hence, CNT/Cu-TSVs experience less $\Delta\varepsilon_f$.

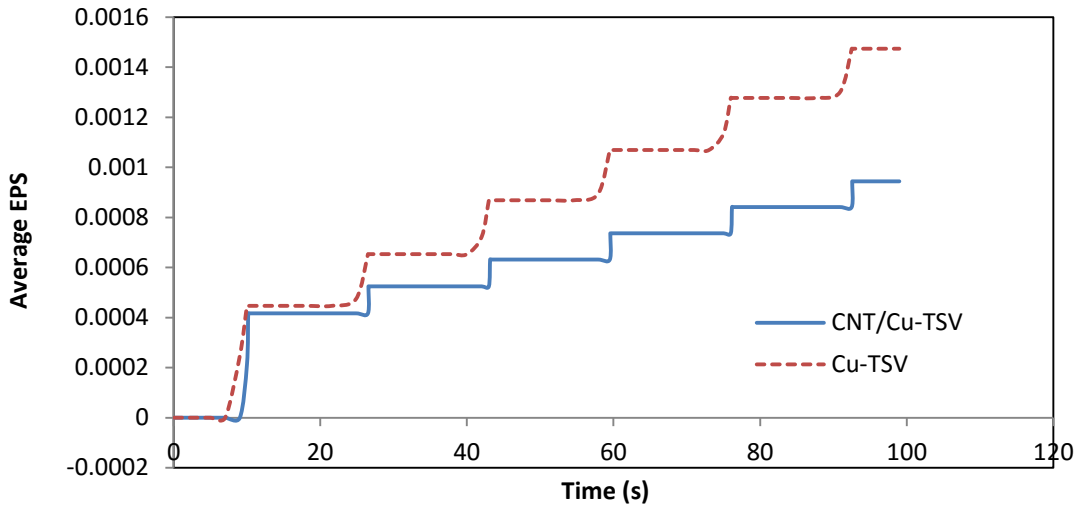

Fig. 67. Average EPS-time behavior for CNT/Cu-TSV and Cu-TSV

For electroplated Cu, the values of ε_f and c_3 are 0.3 and -0.6, respectively [115,116]. From the calculations, fatigue lives for CNT/Cu-TSV and Cu-TSV are 324,602 cycles and 100,561 cycles, respectively. In other words, a threefold increase in the fatigue life has been achieved by adding CNTs to Cu in TSVs, which indicates that the proposed material will enhance the fatigue life of TSVs in 3D ICs industry. Thus, CNT/Cu composite seem to be a reliable replacement to Cu in terms of the fatigue life and it can be adopted in the 3D ICs industry.

3.5 Conclusion

MD simulation was employed to examine the interfacial strength of SWCNT/Cu interface. Many arrangements of SWCNT/Cu have been simulated to study their effect. From MD simulation, increasing the number of SWCNTs in contact with Cu linearly increases the pull-out force. This relationship can be used to predict the total pull out force for a bundle of SWCNTs. Embedded length does not have a significant effect on the average pull-out forces. Only amplitude of oscillation increases because of stick-slip behavior but the average force is almost the same. When one SWCNT strand adjacent to another SWCNT strand and Cu slab is

pulled-out of Cu, C-Cu vdW interaction was found to be stronger than C-C vdW interaction. The SWCNTs were found to have a very strong C-C bonding. Adding interior SWCNTs which are not in contact with Cu, will not affect the value of average pull-out force. Interfacial shear strength is independent of the embedded length but dependent on the average force (F_{avg}) and work done by the pull-out force. The interfacial shear strength can be predicted for a bundle of SWCNTs by considering the previous effects.

MD simulation using LAMMPS is also employed in order to evaluate the CZM parameters and the effect of the number of walls and temperature. Virial stress with eliminating the kinetic part (from MD simulation) is used to represent the Cauchy stress. The CZM obtained from 2-, 3-, 4-, 5-, 6- and 7-wall MWCNT was found to be similar to Barenblatt model. The key parameter for the model were generated and reported here. The number of walls has a great effect on the CZM. As the number of wall increases, the interface gets weaker due to the inter-tubular effect of the inner walls. Inner walls attract the outer walls towards the center of the MWCNT strand and away from the interface with Cu. Thus, less load will be required to separate the MWCNT strand from Cu. Nonetheless, after separation, outer walls still have some compressive stress residue due to inner walls interaction and this residual compressive stress increases with increasing the number of walls.

The normal cohesive strength non-linearly decreases with increasing the number of walls. Furthermore, the displacement at the maximum stress also decreased non-linearly when the number of walls increased.

Effect of temperature on CZM parameters shows an abrupt change in the CZM when temperature changes from 1°K to 75°K. However, statistical analysis shows no true relationship between temperature and either σ_{max} or δ_n.The variation in the results is believed

to be greatly affected by the noise induced by atoms' oscillations. Furthermore, when relative standard deviation was calculated for temperatures above 1°K, temperature was found to have no significant effect on CZM parameters.

Multiscale modeling is employed in this study to bridge nano- through micro-scale in order to evaluate the mechanical Integrity of the novel CNT/Cu composite TSV. MD is used to evaluate CZMs in both axial and normal directions. Bilinear CZMs are fitted to MD simulation results and are used in FE analysis in order to apply bending loading and thermal cycling. Separation of the CNT/Cu interface was a concern during the FE analysis. In bending, separation initiated when D_{max}=46.19 μm. When von Misses stress distribution was checked at the instant of separation, Si's UTS was exceeded which implies that Si fails prior to CNT/Cu separation. In other words, CNT/Cu interface can withstand substantial deformation. The big difference in the axial displacement U_x is a clear indication of separation. This big difference is caused by the big difference between CNT's Young's modulus (1 TPa) and Cu's Tangent Modulus (517.8 MPa). In order to compare CNT/Cu-TSV to pure Cu-TSV, plastic deformation of Cu was chosen as a criterion. Separation of CNT/Cu interface did not take place prior to plastic deformation of Cu; however, after plastic deformation took place, EPS was found to be higher in CNT/Cu-TSV. This is believed to have been caused by high stiffness of CNT bundle which promotes the compression of Cu at the top of the via. In thermal cycling, the CTE mismatch of the different material causes bending of the via during the loading cycle. In order to study the bending effect, total mechanical strain in x-direction (ε_x) was studied. Maximum tensile and compressive strains in x-direction took place at the bottom of the CNT/Cu interface; 2.14E-3 and -1.3E-3, respectively—after heating up to 398 and cooling down to 299, respectively. At the end of the thermal cycle, no separation took place; however, plastic

deformation occurred at the top and the bottom of the Cu due to tensile and compressive stresses. Nonetheless, when CNT/Cu-TSV was compared to Cu-TSV, Cu underwent less plastic deformation in the Cu-TSV at the Cu/Si interface (EPS=0.22E-3) in contrast to 0.73E-3 at the CNT/Cu interface in the CNT/Cu-TSV. However, both cases reached plasticity at the end of the loading cycle. In the case of CNT/Cu-TSV, plastic deformation did not occur at Cu/Si interface because the CNT's negative-sign CTE is believed to have shifted the plastic deformation away from Cu/Si interface.

From the results of the bending and thermal loading cases, more investigation is recommended in order to alleviate the plastic deformation at the CNT/Cu interface in order to offer an efficient replacement to Cu-TSVs.

In the current study, a multiscale modeling technique is conducted to evaluate the fatigue life of CNT/Cu-TSV in 3D IC packages. A series of MD simulations are conducted in order to evaluate some significant mechanical properties at the atomic scale. Uniaxial stress-strain behavior of a selected MWCNT is evaluated. UTS of the selected MWCNT is found to be 233 GPa. CTE is also evaluated using MD simulations in the radial and axial directions at different temperatures. CTE was found to have a dependence on the temperature at lower temperature (<200), while it does not have a significant dependence on the temperature at higher temperatures (>200). FE analysis is conducted using the CNT's uniaxial stress-strain behavior and CNT's CTEs along with previously defined CZM for the CNT/Cu interface. An accelerated thermal cyclic load based on JEDEC standard is applied on a representative 3D IC package with a single TSV at the edge. No separation of CNT/Cu-interface was observed during thermal cyclic load. Out of the materials used for this package, Cu is expected to experience plastic deformation, thereby low cycle fatigue. Therefore, EPS was obtained in Cu

at CNT/Cu and Cu/Si interfaces. However, it was higher at the CNT/Cu interface. Moreover, $\Delta\varepsilon_f$ was higher at CNT/Cu-interface. Thus, Cu's EPS values at the CNT/Cu-interface are used for the fatigue life estimation. CNT/Cu-TSV was compared to Cu-TSV. Adding CNTs was found to be advantageous because it alleviated the overall CTE mismatch between CNT/Cu-composite and Si. Addition of CNTs redistributed the plastic deformation in Cu on two surfaces—CNT/Cu surface and Cu/Si surface—instead of having the plastic deformation on just one surface in the Cu-TSV. Finally, adding CNTs increased the fatigue life time by threefold.

CHAPTER 4. FABRICATION EXPERIMENTS

4.1 Fabrication

Encapsulating CNT bundle with Cu has not shown an improvement in the resistivity of the CNT/Cu-TSV when fabrication was attempted by Feng et al. [56,57]. High resistivity is believed to be resulted from the low density of the composite material. Therefore, creating a CNT/Cu composite by depositing Cu in a way that allows Cu to infiltrate CNTs is believed to overcome the density issue. Moreover, Cu is believed promote the adhesion between TSVs and the other metallic components, and its presence is believed to enhance the mechanical stability of the TSV. The proposed process in the introduction section is followed. The process starts with patterning the photoresist with 20 and 25-μm-diameter circles by photolithography (Fig. 8-a). Thick-type (AZ P 4620) photoresist is used for coating for the following Deep reactive ion etching (DRIE) process. DRIE is used to create 100-μm-deep cylindrical blind vias (Fig. 8-b). DRIE uses BOSCH process [117] technique where ions bombard Si at low temperature, and it is very convenient for creating cylindrical profiles with high aspect ratios. Then, photoresist is stripped away using Asher resist stripper. The vias are cleaned in accordance to Piranha clean process. The Piranha solution is (4:1) mixture of Sulfuric Acid (H_2SO_4) with Hydrogen

Peroxide (H_2O_2). Insulation layer of SiO_2 (200 nm) is diffused thermally on the surface of the wafer and the walls of the vias (Fig. 8-c). A 20-nm layer of Al_2O_3 is deposited as a buffer layer using Electron Beam (E-Beam) evaporation at room temperature and 2×10^{-3} mTorr. Buffer layer is deposited prior to catalyst deposition in order to avoid the formation of silicide during the growth process [118–120]. Alumina, in particular, assists to grow aligned CNTs. Another characteristic feature of alumina is that it restricts the surface mobility of the catalyst due to the strong substrate-catalyst interaction [121]. A catalyst layer of 2.5-nm Fe is deposited by E-Beam evaporator. Vertically aligned CNTs are grown using thermal Chemical vapor deposition (CVD). Aixtron-Black Magic Pro is used for the CVD process. The wafer is cleaned by 60 seconds of Ar flow at 1000 sccm in the CVD tool. The Fe catalyst is annealed by 500 sccm flow of H_2 for 180 seconds at 700 ^oC and 25 mBar. Then, the growth process is started by 50 sccm flow of C_2H_2 along with 500 sccm of H_2 for 300 seconds at 25 mBar (Fig. 8-d). Since CNT characteristics i.e. density, growth rate and crystallinity have been found affected by the growth temperature [122], different temperatures (675, 700 725 and 750 ^oC) are used for the growth step so as to study the temperature effect on the properties of the grown CNTs, and to inspect if CNTs grow inside the vias.

In order to optimize the properties of the grown CNTs, additional growths of CNTs on the top of the Si wafer is attempted using different under-layers, catalysts and growth process, e.g. plasma enhanced CVD (PECVD). After the creation of SiO_2 layer, Ti is deposited as an under-layer using AJA sputtering system in the presence of gaseous plasma (Ar). A 300-nm layer of Ti is deposited at room temperature and 3 mTorr pressure at a growth rate of 10 Å/s. Then a layer of 2.5-nm Fe catalyst is deposited using the latter E-Beam evaporation process. Then,

catalyst is annealed and growth takes place in the same thermal CVD process described earlier at 750 ^{o}C.

TiN is also attempted as an under-layer. A 100-nm layer of TiN is deposited using the sputtering system at room temperature and 3 mTorr pressure at a growth rate of 1.5 Å/s. Then, two kinds of catalysts are deposited using E-Beam evaporation. Thicknesses of 2.5 nm and 7 nm of Fe and Ni are deposited, respectively. Then, both CVD and PECVD CNT growth are conducted on each catalyst. Annealing and growth for thermal CVD is done in the previously described manner at 750 ^{o}C. Annealing for PECVD is done by flowing a 200 sccm of Amonia for 10 minutes at 650 ^{o}C. Then growth takes place by flowing C_2H_2 (precursor) along with Amonia (Annealing gas) at 100 sccm and 400 sccm, respectively for 30 minutes.

Three different processes are examined to deposit Cu; electroless plating, electroplating and sputtering. Electroless plating is done by the project partners at United Technology Research Center. Prior to electroless plating, the surface of the CNT/CNF goes through activation process in order to enable uniform nucleation formation. Surface activation is conducted by several repeated rinsing of the nanostructure with a solution of 1 g/L of Tin Chloride ($SnCl_2$), 1 mg/L of Hydrochloric acid (HCl- 37%) and 1 g/L of Palladium Chloride ($PdCl_2$). The main purpose of this activation process is to seed the surface of CNT/CNF with Pd nuclei, which initiate the Cu electroless plating process. During the activation process, Pd ions on the surface of CNT/CNF are reduced by Sn^{+2} according to Sn2+ + Pd2+ = Pd0 + Sn4+

Eq. 17 to for Pd nuclei that will catalyze Cu plating.

$$Sn^{2+} + Pd^{2+} = Pd^{0} + Sn^{4+} \qquad \text{Eq. 17}$$

Then, Cu plating is conducted using a solution of 16.67 g/L of Copper Sulfate Pentahydrate, 13.45 g/L of Ethylenediaminetetraacetic acid (EDTA) and 2Na $2H_2O$ and

1.28g/L of Hydrazine. Solution is maintained at 40 °C using a water bath, with continuous mixing of the solution. Cu deposition was performed after solution pH was increased above 11.0 using controlled addition of sodium hydroxide [27]. This pH restriction imposes the use of complexed Cu ions in the electroless solution in order to prevent precipitation of Cu (II) Hydroxide. Then, ~4% hydrazine solution was added slowly to make the hydrazine concentration 1.28 g/L. Hydrazine serves to reduce Cu ions to metallic Cu on the surface of the activated CNTs, as shown by the chemical reaction of

$N2H4 + 2Cu2+ + 4HO- \rightarrow N2\uparrow + 4H2O + 2Cu$ Eq. 18. The plating can last from one to three hours. Once the plating process was completed, the Cu coated CNTs were rinsed with deionized water and oven dried. A desired thickness of Cu can be achieved by plating several times.

$$N_2H_4 + 2Cu^{2+} + 4HO^- \rightarrow N_2\uparrow + 4H_2O + 2Cu \qquad \text{Eq. 18}$$

For electroplating process, a CHi potentiostat workstation with a standard 3-electrode setup is used where a pyrolytic graphite rod electrode was used as counter electrode, and saturated calomel electrode was used for a reference electrode in 1 M of $CuSO_4$ dissolved in 1 M of H_2SO_4 as electrolyte. A range of applied potential from -0.4 to -1.0 V was investigated. For calibration, the potential was applied for a certain time and investigated the deposition of Cu on the CNTs.

A physical Cu deposition technique was also tested. Plasma assisted sputtering system AJA was used as an alternative to deposit Cu on the CNT forest. A 7-μm layer of Cu is deposited at room temperature, under a pressure of 3 mTorr and at a growth rate of 10 Å/s.

4.2 CNT Growth

4.2.1 *CVD Growth of CNTs on Fe/Al_2O_3 stack inside TSV*

The alignment and the density of CNTs are key qualities that dictate the electrical conductivity of CNTs [123]. More aligned and denser CNT bundles provide better electrical conductivity. The following results are for the wafers that have TSVs and CNTs grown using thermal CVD, AL_2O_3 under-layer and Fe catalyst. This process was conducted at different growth temperatures (675, 700 725 and 750 ^oC). From observation, temperature had observable effect on the quality of the grown CNTs as seen in Fig. 68. From observation, CNTs grown at 750 °C obtained the highest quality; density and orientation.

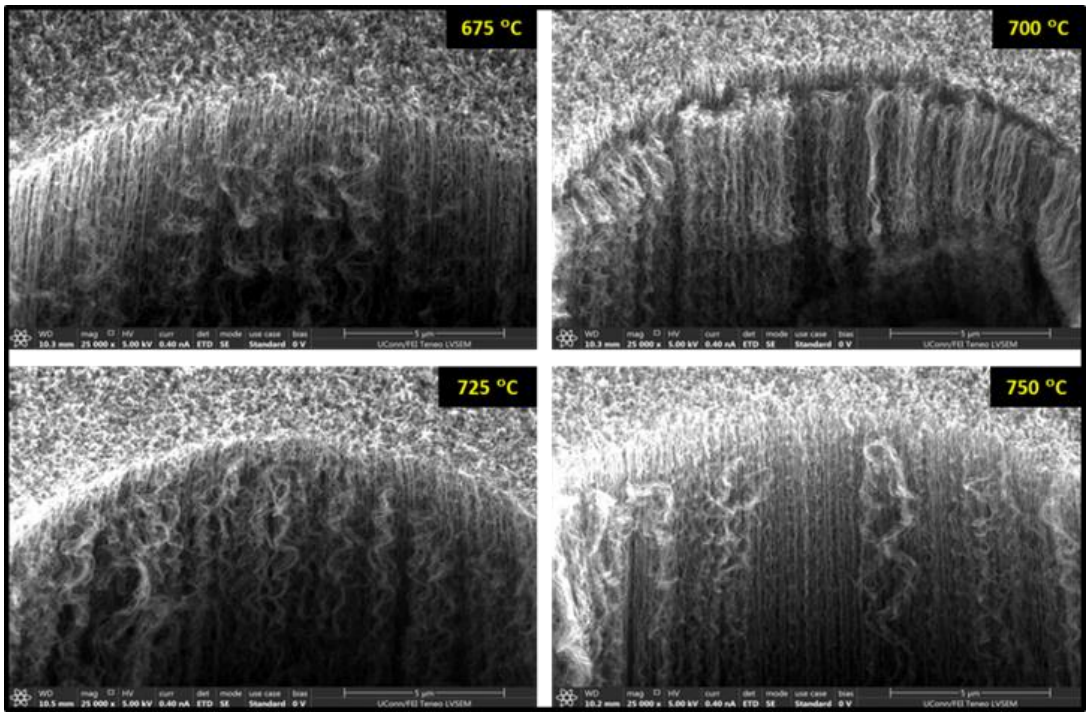

Fig. 68. (a) Top view of the grown CNTs (b) 30°-tilted view of the grown CNTs

Also the growth rate has been examined. As shown in in Fig. 69, the length increases as the temperature increases. The growth rate are found to be 15 μm/min, 25 μm/min, 50 μm/min and 80 μm/min for the samples grown at 675 ºC, 700 ºC, 725 ºC and 750 ºC, respectively. Thus, increasing the growth temperature increases the CNT growth rate.

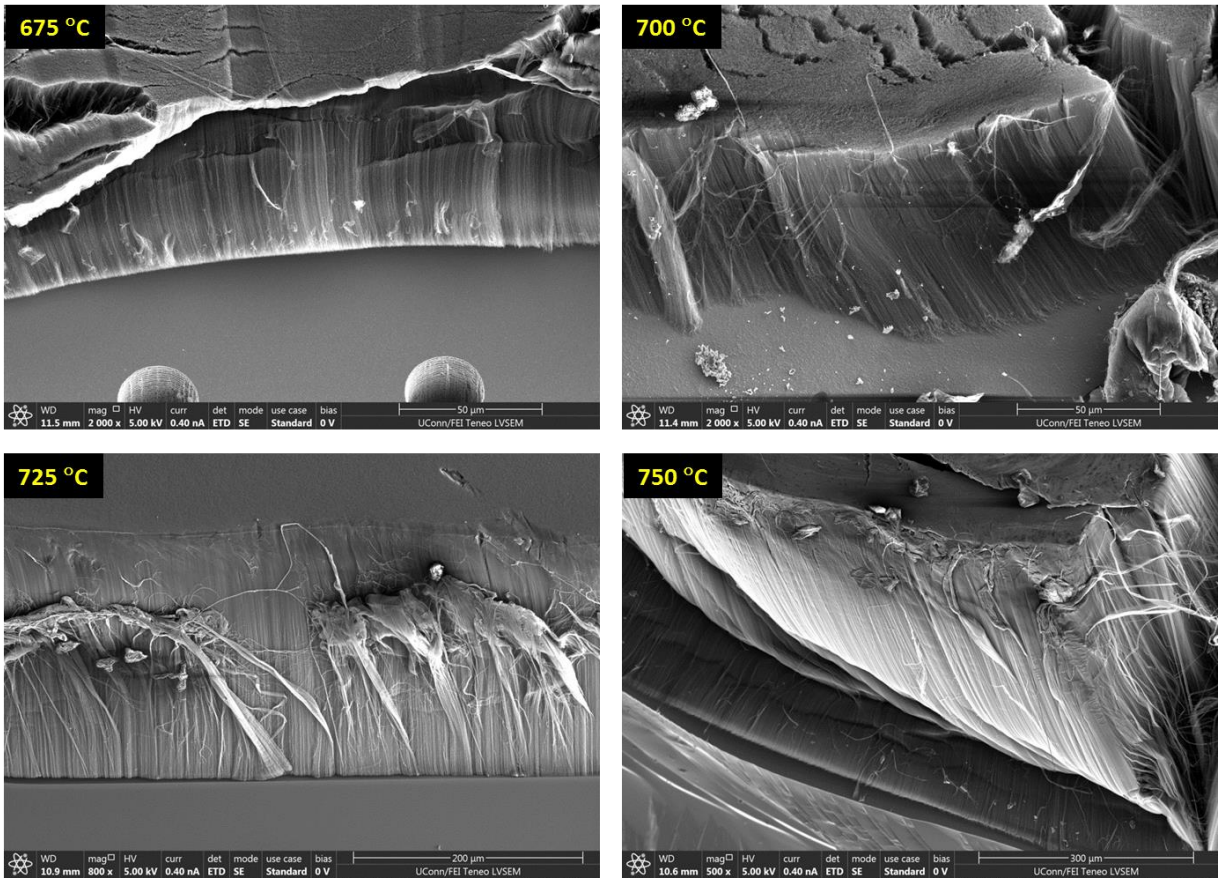

Fig. 69. Length of the grown CNTs

CNTs inside the vias are the main concern of this study. After cleaving the samples, CNTs were found protruding from vias in only the samples that were grown at 750 °C as seen in Fig. 70-a. CNTs were scrapped off of the surface of the wafers that have CNTs grown at different temperatures. CNTs could be observed in the TSVs of 750 °C sample (Fig. 70-b), while the TSVs in the other samples that were grown at the other temperatures looked empty

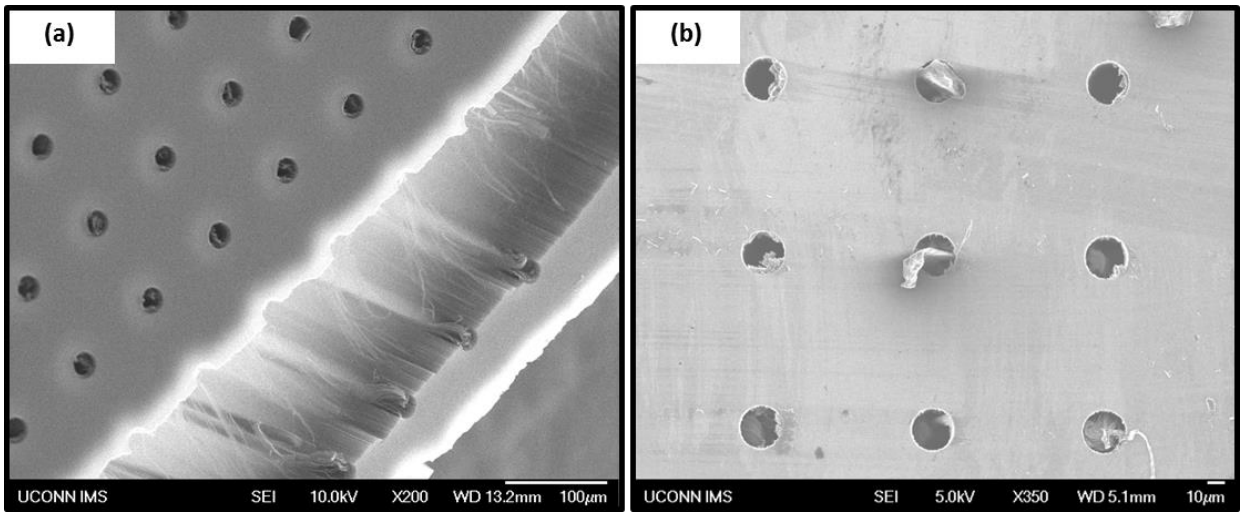

Fig. 70. Illustration of CNTs (a) using tilted view of the 750 °C ample after cleaving, (b) top-view of the 750 °C sample after scrapping CNTs off of the surface,

Therefore, cross-sectioning is required to inspect the TSVs from inside. Focused Ion Beam cross-sectioning was conducted to look inside the TSVs. However, CNTs were only found grown inside the 750 °C TSVs as shown in Fig. 71-a and b. For the 750-°C wafer, CNTs that are grown on the surface were scraped off manually in order to be able to locate the TSVs that have CNTs easily before cross-sectioning. The same process was done to the 725-°C wafer but CNTs could not be observed anyway. As seen in Fig. 71-b, CNTs are grown on the walls of the TSVs, which means that the catalyst was deposited on the wall of the CNTs. Therefore, more care should be taken during aligning the wafer inside the e-beam evaporator so that the catalyst is only deposited on the bottom of the TSV during the e-beam evaporation process. CNTs are not protruding from the TSV. This observation is believed to be a result of scraping them off such that the CNTs' tops were removed leaving the bottom parts attached to the bottom of the TSVs.

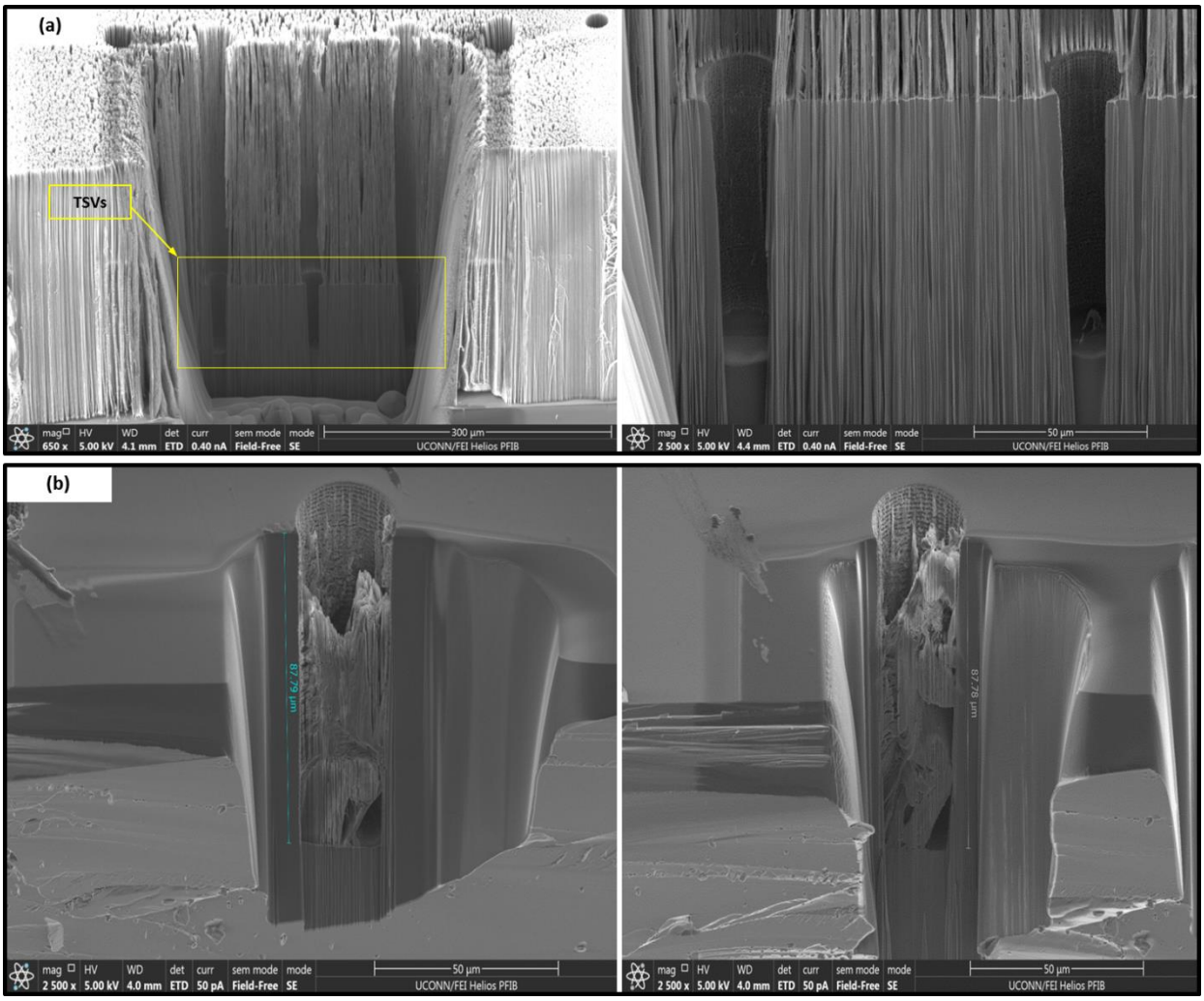

Fig. 71. FIB cross-sectioned TSVs for (a) the 725 °C sample and (b) the 750 °C sample

4.2.2 *CVD Growth on Fe/Ti Stack*

An alternative solution is proposed in order to overcome the adhesion issue. In later studies, using Ti as under-layer increases the adhesion and CNTs did not detach during the immersion in the plating solution [124,125]. Therefore, Ti is used as under-layer. Also, Ti acts as a seed layer for the electroplating process. A 300-nm layer of Ti was deposited using AJA sputtering system. A layer of 2.5-nm Fe was deposited as a catalyst using E-Beam evaporation. Then, CNTs were grown using the previously described thermal CVD recipe. As seen in Fig.

72, the quality of CNTs is very poor. They are tangled and short. Thus, Fe/Ti stack is inconvenient for the vertical interconnect applications. Ti is believed to be mixed with Fe during the nucleation of the catalyst at the high temperature so that a new catalyst layer (alloy of Ti and Fe) is formed that resulted in the current CNTs.

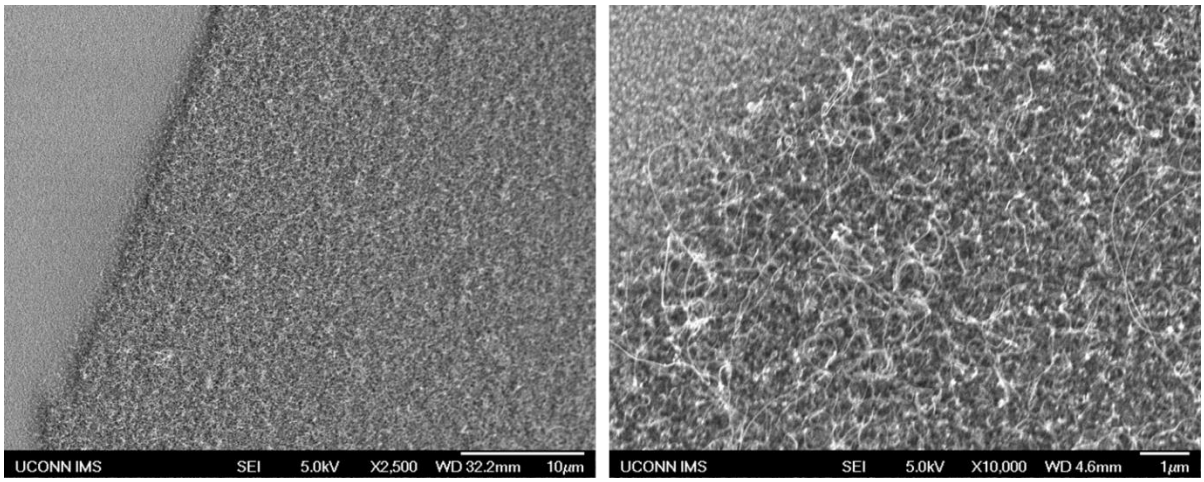

Fig. 72. SEM images of CNTs grown on Fe/Ti stack at different magnifications

4.2.3 *CVD and PECVD Growth on Fe/TiN and Ni/TiN Stacks*

TiN was also tried as under-layer. A layer of 300 nm thick TiN was deposited using the AJA sputtering system. Then, two kinds of catalysts were deposited individually. Fe and Ni were deposited using E-Beam evaporation and their thicknesses are 2.5 nm and 7 nm, respectively. Both thermal CVD and PECVD growth of CNTs were carried out on each catalyst. Neither Fe nor Ni has yielded CNT growth using thermal CVD as depicted in Fig. 73.

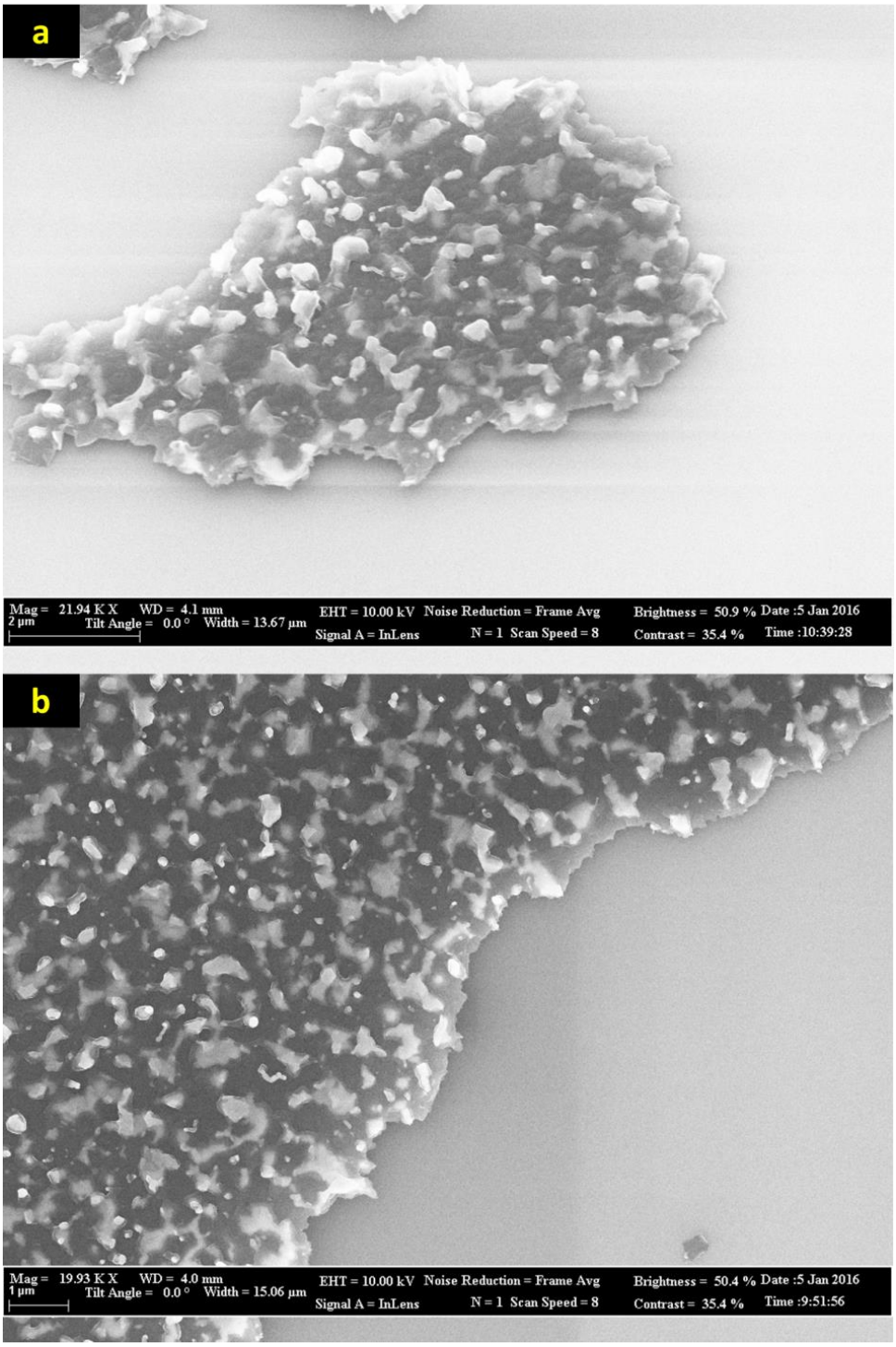

Fig. 73. Results of using thermal CVD on (a) Fe/TiN and (b) Ni/TiN stacks

Using PECVD on both Fe and Ni catalysts has yielded CNT growth as seen in Fig. 74. Grown CNTs are self-aligned; however, they are significantly shorter (≈3 μm) and less dense than CNTs grown using thermal CVD on Fe/AL_2O_3 stack. Moreover, growth rate is also low; it is almost 0.1 μm/min. Both CNTs grown on Fe/TiN and Ni/TiN have almost the same length range (≈2 μm), while CNTs grown on Ni/TiN are thicker than those grown on Fe/TiN.

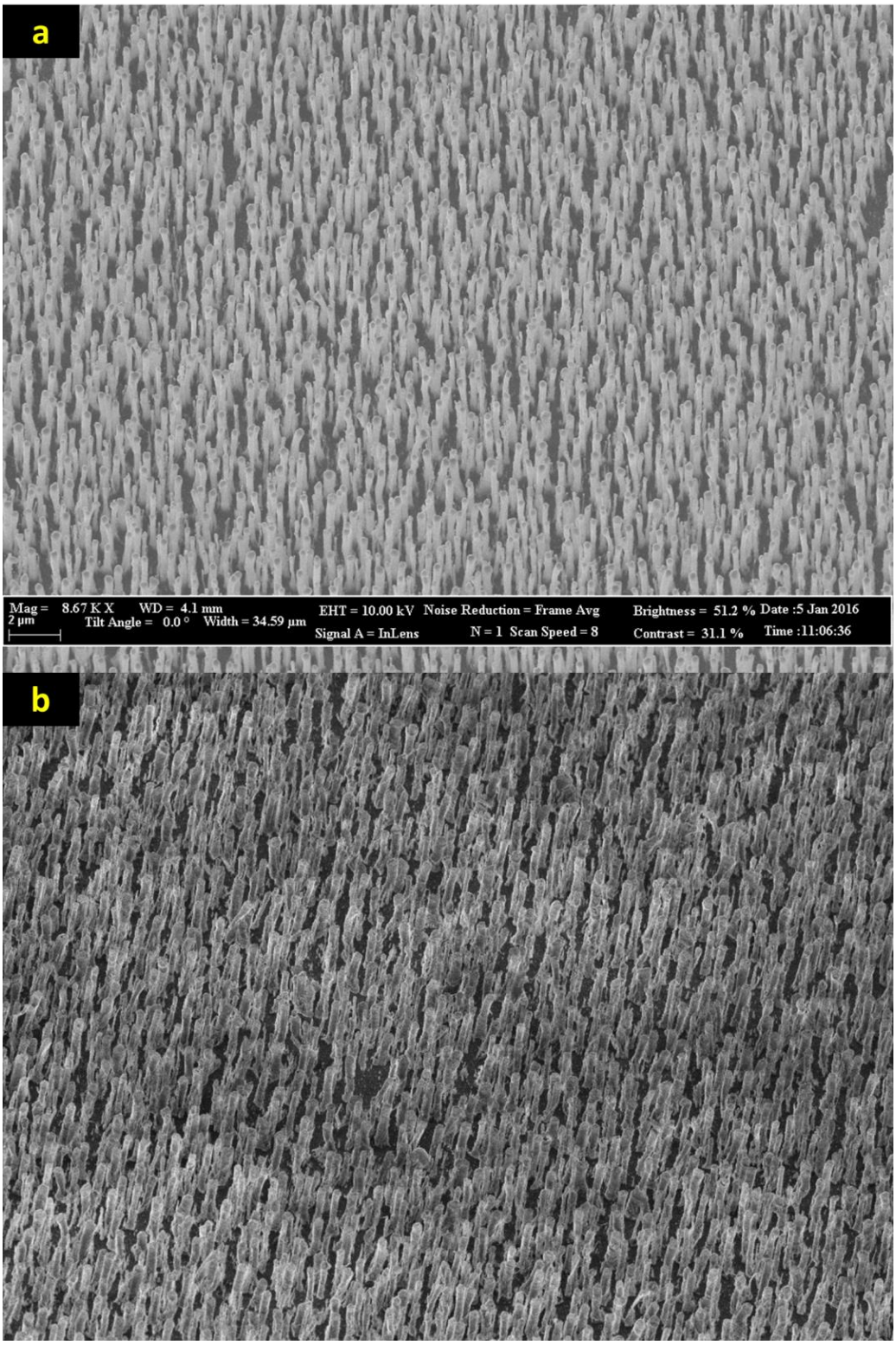

Fig. 74. Results of using PECVD on (a) Fe/TiN and (b) Ni/TiN stacks

4.3 Cu Deposition

Cu depositions were conducted on the grown CNTs that show promising properties such as growth rate, self-alignment and density.

4.3.1 *Electroless Plating*

Electroless plating was conducted on the CVD grown CNTs on Fe/Al_2O_3 stack because these CNTs has shown the highest growth rate (80 μm/min) and the most self-aligned densest structure. The advantage of electroless plating is that it does not need a seed layer. This process was conducted by United Technology Research Center. It was unsuccessful because CNTs detached from the surface of the substrate when it was left in the plating solution. The reason is believed to be the weak adhesion between the CNTs and the catalyst-coated substrate.

4.3.2 *Electroplating*

Electroplating Cu was conducted on the CVD grown CNTs on Fe/Al_2O_3 stack. Electroplating of the samples was done by immersing them in the electroplating solution for 30 hours; however, Cu was deposited discretely only on the top of the CNTs as seen in the SEM image and the associated Dispersive Energy Spectroscopy (EDX) results (Fig. 75). Cu was found deposited on the CNTs that are located around to the clips that is used to connect the sample to the potentiostat. Furthermore, most CNTs detached from the surface because of the weak adhesion between CNTs and the substrate. Discrete Cu deposition of the top part of CNTs is believed to be as a result of the lack of a conductive layer—seed layer—beneath CNTs and interlocked CNTs located at the top and near the potentiostat clips slightly conductive so that it could attract few Cu ions. Another possibility for the Cu deposition on the top of the CNTs is that tip-growth mode of CNTs took place such that CNTs grow beneath the

catalyst nuclei located on the top of the CNTs that would act as seed layer for the Cu deposition. However, Fe peaks were not found in the EDX spectrum in Fig. 75 and that makes this possibility invalid.

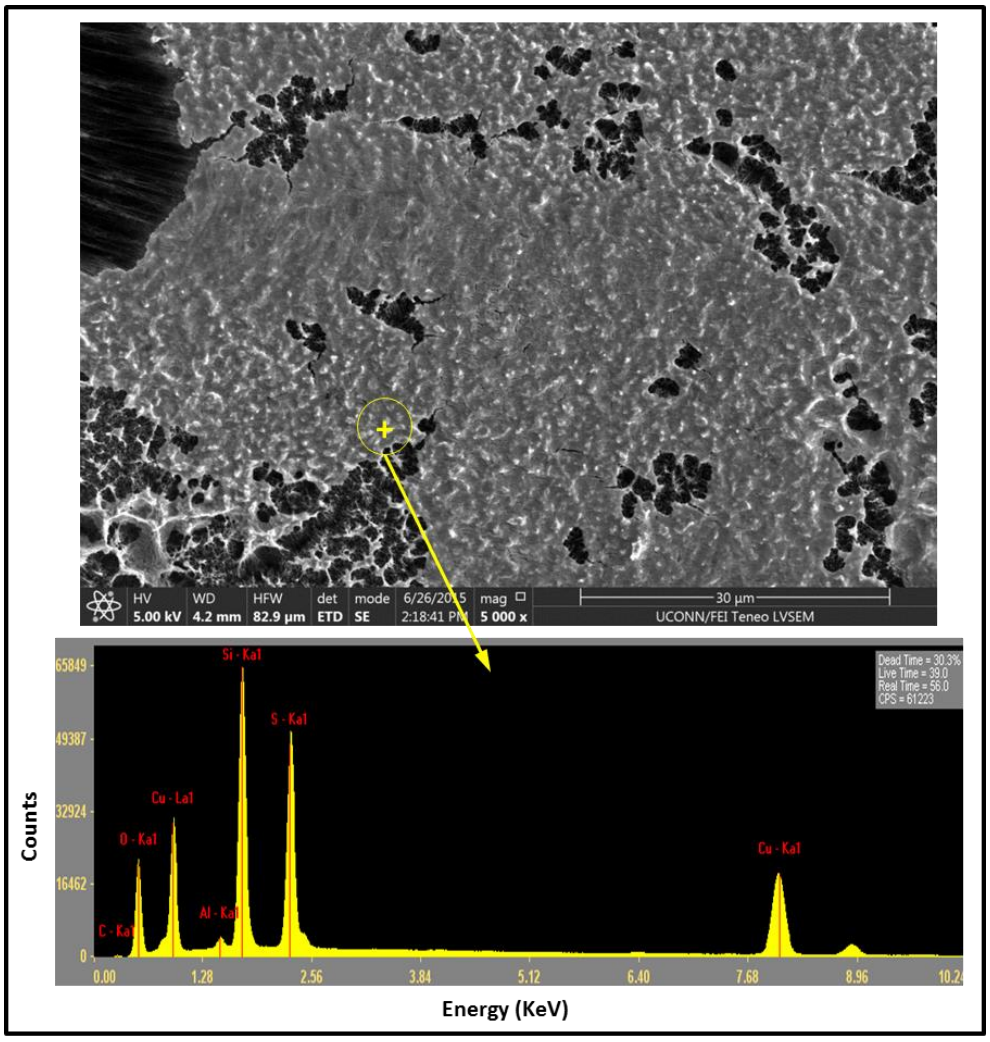

Fig. 75. Electroplated CNTs with EDX spectrum

Cu Electroplating of PECVD grown CNTs on Fe/TiN and Ni/TiN stacks was also attemted. Cu Electroplating was also tried on these grown CNTs. Cu could not be deposited. Electricity did not pass through the substrate because of the high resistance. The measured resistance was

found to be 1 MΩ. However, CNTs were stable and did not detach from the substrate during the electroplating process.

Thus, a different dry way of Cu deposition is required, or different under-layers (i.e. catalyst and buffer layers) that would promote the adhesion between CNTs and the substrate are required.

4.3.3 *Cu Sputtering*

A physical Cu deposition technique is attempted on the CVD grown CNTs on Fe/Al_2O_3 stack. AJA Sputtering system was used as an alternative to deposit Cu on the CNT forest. A 7-μm layer of Cu is deposited at room temperature, under a pressure of 3 mTorr and at a growth rate of 10 Å/s. However, as seen in Fig. 76-a, Cu could not infiltrate CNTs due to the low aspect ratio of sputtering process. However, Cu covered the CNTs that are located at the edge of the wafer as shown in Fig. 76-b.

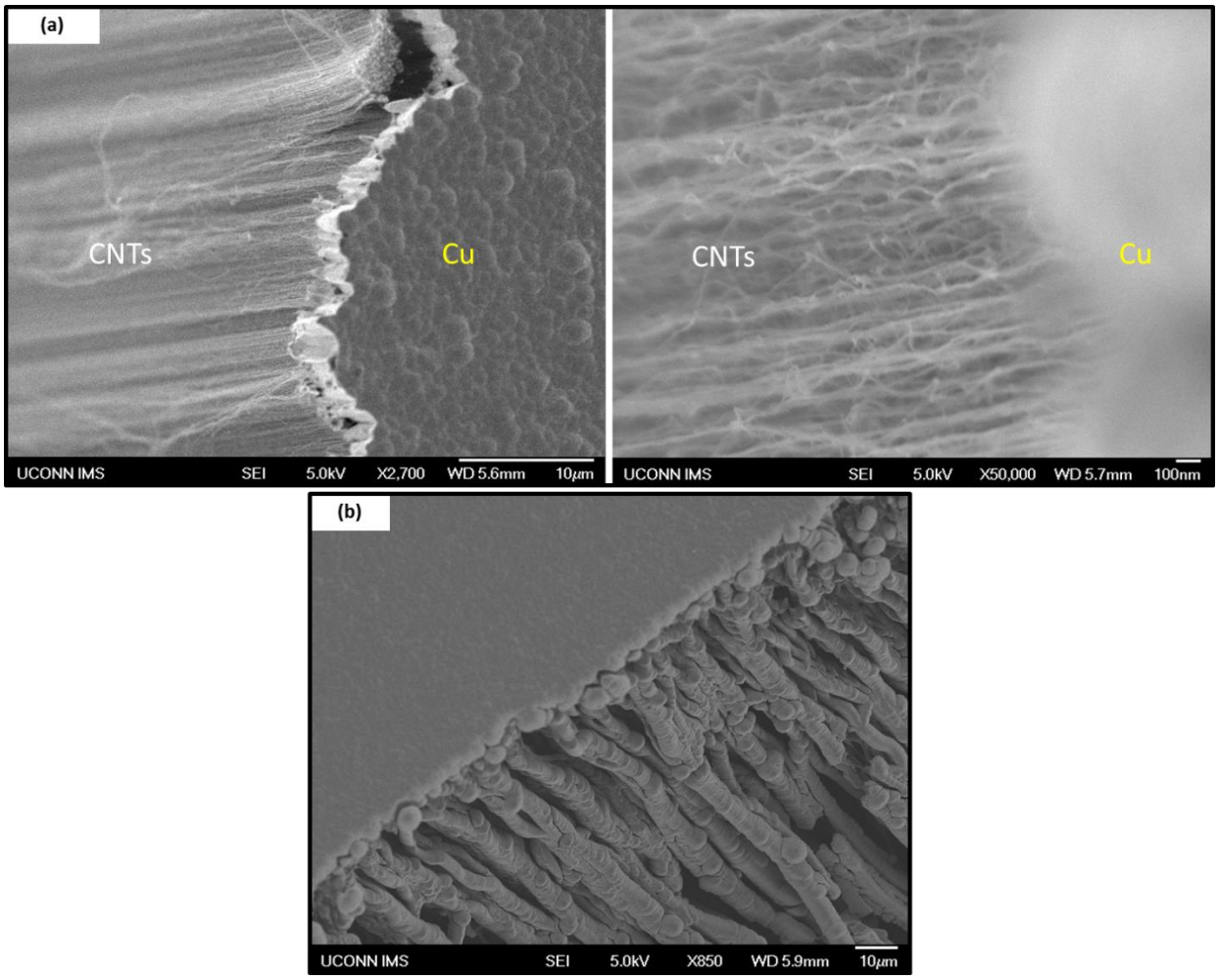

Fig. 76. SEM images of Cu deposited CNTs using e-beam evaporation (a) in the middle of the middle and (b) at the edge of the wafer

4.4 Summary and Conclusion

Fabrication of CNT/Cu-TSV has been investigated. Different CNT growth techniques, under-layers, catalysts and temperatures have been investigated in order to understand their effect on the properties of CNTs as depicted in Table 5. Using thermal CVD with Fe/Al_2O_3 has yielded self-aligned, long and dense CNTs. Moreover, the best alignment and densest CNTs have been obtained at growth temperature 750 ºC. TSVs were etched in these wafers. CNTs

have been observed only in the wafer that has CNTs grown at 750 ºC. CNTs grown on Fe/Ti stack using thermal CVD are tangled and very short. Also, CVD was conducted on Fe/TiN and Ni/TiN and CNTs have not been obtained. However, CNTs have been obtained when PECVD was used for the growth process instead of thermal CVD. Moreover, the obtained CNTs are self-aligned but neither dense nor long. The growth rate is very low (0.1 µm/min).

Table 5. Summary of CNT growth trials

Process	Under-layer	Catalyst	Temp (C°)	CNTs?	Key Properties	Attempted etching TSVs?	Observed CNTs inside TSVs?
CVD	Al_2O_3	Fe	675	Yes	Dense and aligned	Yes	No
			700	Yes	Dense and aligned	Yes	No
			725	Yes	Dense and aligned	Yes	No
			750	Yes	aligned, dense and fast growth (80 μm/min)	Yes	Yes
	Ti	Fe	750	Yes	Tangled and very short	No	
	TiN	Fe	750	No		No	
		Ni	750	No		No	
PECVD	TiN	Fe	650	Yes	aligned, not dense and slow growth (0.1 μm/min)	No	
		Ni	650	Yes		No	

Different techniques of Cu deposition were attempted on the highlighted samples in Table 5 that have grown CNTs. The findings are summarized in Table 6. For the CNTs grown on Fe/Al_2O_3 using thermal CVD, CNTs detached from the substrate during both the electroplating and the electroless plating techniques; however, Cu was found on the top of CNTs from the electroplating process, since the CNTs are interlocked at the top and it allowed current to pass through them in some parts. Cu deposited by sputtering could not infiltrate CNTs because of the low aspect ratio of the sputtering technique. Electroplating of CNTs grown on Fe/TiN and Ni/TiN could not be accomplished because of the high resistance of the wafers although TiN was deposited to perform as a seed layer.

Table 6. Cu Deposition trials

Sample / Cu Deposition	Fe/Al_2O_3 (CVD)	Fe/TiN (PECVD)	Ni/TiN (PECVD
Elctroplating	- Only on the top - Detachment	- No (high resistance) - Strong adhesion	- No (high resistance) - Strong adhesion
Electroless Plating	No (detachment)		
Sputtering	Only on the top and the edge		

CHAPTER 5. SUMMARY, CONTRIBUTION AND FUTURE RECOMMENDATIONS

5.1 Summary

A thorough investigation of the mechanical behavior of CNT/Cu-TSV is presented in this study from the atomic scale up to the microscale using a multiscale modeling approach. Mechanical evaluation of the interfacial properties of CNT/Cu interface has been evaluated by a series of pull-out tests in MD simulations. SWCNTs in different configurations are pulled out the interface in the axial direction so as to evaluate the interfacial behavior. The relationship between pull-out force and displacement has been monitored for several case studies. Moreover, MWCNT at the interface with Cu has been studied by MD simulations. Pull-out tests have been conducted in the normal-to-the-interface direction in order to evaluate the normal CZM. The effect of the number of walls and temperature on CZM has been evaluated. The concluded mechanical observations from the previous atomic simulations assisted in constructing a multiscale model to evaluate the mechanical integrity of CNT/Cu-TSV. CZMs in both axial and normal directions have been evaluated and used in the continuum FE model to define the contact element parameters between CNT bundle and Cu in CNT/Cu-TSV. CNT/Cu-TSV was subjected to two different loading scenarios; bending and thermal cyclic

loading. The mechanical integrity under these two loading conditions has been studied. In order to create a multiscale model that can represent the mechanical behavior more adequately, stress-strain behavior and CTE of the selected MWCNT have been evaluated using MD simulations in lieu of using previously published data as in the previous multiscale modeling technique. The mechanical reliability and fatigue life have been evaluated and CNT/Cu-TSV has been compared to Cu-TSV. Several fabrication experiments have been conducted in order to find a systematic fabrication technique of CNT/Cu TSV. Two processes of CNT growth have been utilized; CVD and PECVD. Different under-layer and catalyst stacks have been used. Different Cu deposition techniques have been also studied.

5.2 Conclusion and Key Findings

- Pull-out tests using MD simulations are conducted to investigate the interfacial strength between SWCNTs and Cu.
- Different arrangements of SWCNTs at the interface of Cu are modeled.
- Average pull-out force increases linearly with increasing the number of SWCNTs at the Cu interface
- Embedded length of SWCNTs does not have an effect on the average pull-out force at the SWCNT/Cu interface. Only the amplitude of the oscillations increases because of the stick-slip behavior
- C-Cu vdW interaction is stronger than C-C vdW interaction.
- Adding layers of SWCNTs to the layer that is at the interface with Cu will not increase the strength of the interface.

- MD simulation is also used to evaluate the cohesive properties between MWCNTs and Cu.
- Studying MWCNT/Cu interface, CZM parameters of MWCNT/Cu interface are predicted using MD simulations.
- Resulted CZM models are found to mimic the behavior of Barenblatt CZM model.
- As the number of wall increases, the interface gets weaker due to the inter-tubular effect of the inner walls.
- Temperature was found to have no significant effect on CZM parameters.
- After investigating the interfacial properties and the effect of different parameter such as CNT's length, inner layers, number of walls, and temperature, a multiscale modeling approach is conducted to investigate the mechanical integrity of CNT/Cu-TSV.
- Multiscale model bridges nano-scale to micro-scale.
- MD simulations and FEM are used for nano- and micr-scales, respectively.
- MWCNTs are used for the multiscale modeling approach, since they obtain conductive properties.
- CZM of CNT/Cu interface of a selected MWCNT is evaluated using MD simulations.
- Bilinear CZM is found to best fit the extracted CZM.
- Extracted CZM is then used to define the contact element properties between CNT bundle and Cu.
- A representative model of a TSV placed in the middle of a Si wafer is modeled in FEM to investigate the behavior of CNT/Cu-TSV under bending.

- CNT/Cu interface is strong enough to sustain substantial strains; ε_x at separation was 14.4%.
- Comparing CNT/Cu-TSV with Cu-TSV, EPS in Cu in CNT/Cu-TSV is higher than that in Cu-TSV because of the high stiffness of CNT bundle which promotes the compression of Cu at the top of the via.
- Another representative model of a 3D IC package consisting of a TSV attached to layers of die-attach and substrate is modeled using FEM so as to investigate the thermo-mechanical behavior induced by the CTE mismatch between the different components of the package.
- When an accelerated standard thermal cyclic load based on JEDEC is applied, separation of CNT/Cu interface does not take place.
- Plastic strains take place in Cu at the top and the bottom of the CNT/Cu interface due to subsequent tension and compression.
- Comparing CNT/Cu-TSV with Cu-TSV, EPS in Cu in CNT/Cu-TSV is higher than Cu-TSV due to the high stiffness and low CTE of CNT and
- EPS occurred at the Cu/Si interface in Cu-TSV, whereas it did not occur at the Si/Cu interface in CNT/Cu-TSV.
- CNT's low CTE dislocated the plastic deformation away from Si/Cu interface.
- In order to provide more robust evaluation of the mechanical integrity of CNT/Cu-TSV, another multiscale model is conducted in order to estimate the fatigue life of CNT/Cu-TSV.
- MD simulations are conducted to provide more accurate information about the stress-strain behavior and the CTEs of the selected MWCNT.

- CNT behaves hyper-elastically in accordance with Yeoh's hyper-elastic model.
- CNT's UTS was found to be 233 GPa.
- CTE is also evaluated using MD simulations in the radial and axial directions.
- CTE is temperature dependent at lower temperature (<200), whereas it does not have a significant dependence on the temperature at higher temperatures (>200).
- FE analysis is conducted using the CNT's uniaxial stress-strain behavior and CNT's CTEs along with previously defined CZM for the CNT/Cu interface.
- An accelerated thermal cyclic load based on JEDEC standard is applied on a representative 3D IC package with a single TSV at the edge.
- No separation of CNT/Cu-interface was observed during thermal cyclic load.
- Maximum EPS was obtained in Cu at CNT/Cu and Cu/Si interfaces. However, it was higher at the CNT/Cu interface.
- Fatigue life is estimated using Coffin-Manson model.
- Comparing CNT/Cu-TSV to Cu-TSV, plastic deformation takes place at both CNT/Cu and Si/Cu interfaces in CNT/Cu-TSV instead of at Si/Cu interface in Cu-TSV.
- CNT's addition redistributed the plastic deformation over the two interfaces, which reduced EPS in these locations.
- Adding CNTs increased the fatigue life by threefold.
- A systematic fabrication technique of CNT/Cu-TSV has been investigated.
- Using thermal CVD on Fe/Al_2O_3 stack yields self-aligned and dense CNT forests.
- Increasing temperature in the CVD growth of CNTs increases the growth rate.

- Best properties and highest growth rate was obtained at 750 ^{o}C for the CNTs grown by thermal CVD on Fe/Al_2O_3.
- Growth of CNTs inside TSVs was only obtained when thermal CVD growth was done at 750 ^{o}C on Fe/Al_2O_3 stack.
- Many Cu deposition techniques were attempted on the samples grown at 750 ^{o}C on Fe/Al_2O_3 stack using thermal CVD:
    - Electroplating: Cu was partially deposited on the top of CNT forest around the potentiometer clips because the lack of a conductive under-layer. Furthermore, CNTs detached from the substrate.
    - Electroless plating: CNTs detached from the substrate and deposition did not take place.
    - Physical deposition by sputtering: Cu was deposited on the top of CNT forests and could not infiltrate CNTs because of the low aspect ratio of sputtering process.
- Another way is replacing Al_2O_3 with Ti, since it is believed to increase the adhesion and act as a seed layer for Cu deposition by electroplating as well. However, grown CNTs' were so tangled and short that it would not comply with the CNTs' properties required for TSVs.
- Also, TiN was attempted as an under-layer.
- Two different catalysts were deposited on TiN; Fe and Ni. CNTs were grown using two different processes; thermal CVD and PECVD
    - CVD: No growth from both Ni/TiN and Fe/TiN stacks.

- PECVD: Self-aligned and not dense CNTs grown at 0.1 μm/min for both stacks

- Cu electroplating of the successfully grown CNTs was conducted but current could not pass through the sample because of the high resistance (1 MΩ).
- However, grown CNTs are stable and did not detach from the substrate during the electroplating process.
- From the results, there are three techniques of fabrication that have a good promise for the application in next-generation interconnects; CVD using Fe/Al_2O_3 and PECVD using Ni/TiN and Fe/TiN.
- Methods to promote the adhesion between CNTs and the substrate in the CVD process are needed.
- Methods to increase the growth rate of CNTs in PECVD are needed.
- Different Cu deposition methods can be also tried on PECVD samples such as electroless plating and sputtering.

5.3 Recommendations for Future Work

As a result from the preliminary theoretical investigation of CNT/Cu-TSV, CNT/Cu-composite has a promising potential to replace Cu in next-generation microelectronics due to its reported improved mechanical and thermos-mechanical performance. CNTs growth at 750 ^{o}C has yielded the sought CNT properties; fast growth rate (80 μm/min) and self-well-aligned dense CNT forests. However, CNTs adhesion to the substrate was so weak that they detached from the substrate once they were immersed in the plating solution. Researchers have investigated ways to promote the adhesion between CNTs and substrate. Pint et al. [126] has

demonstrated a new method to enhance the adhesion between grown CNTs and substrate. They were able to obtain CNTs anchored to the catalyst-coated substrate that can be only removed by peeling using adhesive material or brute wet etching using acids. The proposed method demonstrates cooling CNTs in C_2H_2 environment. As the catalyst (Fe) cools down, Fe-C compounds will form on the surface of Fe nucleus beneath the CNT strands. These compounds involve a surface-segregated shell surrounding Fe nucleus due to the surface energy difference between Fe and C. CNT will be fixed to Fe droplets by C-C bonds to the C shell, which has mixed Fe-C bonds to the catalyst. Thus, CNTs are fixed to the catalyst. Same procedure can be followed after CNT growth during cooling in the CVD chamber. Then, CNTs can be plated using either electroplating or electroless plating techniques. After fabrication is done, interfacial properties of CNT/Cu-interface can be evaluated by conducting atomic force microscope-assisted pull-out tests. Furthermore, resistivity of CNT/Cu-TSV can be evaluated by designing a daisy chain circuit—the current mask was designed to facilitate the resistivity measurement.

From a concurrent research done on the fabrication of Carbon Nanofiber (CNF)/Cu-composite (APPENDIX B), CNFs were grown using PECVD at lower temperature and they were successfully plated by Cu using electroless plating technique without detachment. Same Cu deposition technique can be conducted on the successfully grown CNTs using PECVD. Also, Cu can be physically deposited on them using the sputtering system. However, growth rate is very low (0.1 μm/min). Different catalyst layers can be used in order to enhance the growth rate in PECVD. Reported results of using Fe (1 nm)/Ti (1 nm) as catalyst stack has resulted in 100 μm of self-aligned CNTs in 10 minutes (≈8.34 μm/min) [127,128]. Hence, growth cost could be minimized as well. Thus, the same process can be also used with adding a

buffer layer beneath the catalyst. Also Cu can be physically deposited on these CNTs using sputtering.

In order to grow CNTs only inside the vias and to avoid growing them on the surface of the wafer, deposition of resist on the etched wafer prior to e-beam evaporation is required. The photoresist can be deposited and then patterned by aligning the original mask on the substrate and develop the resist such that the TSV locations are exposed. Then, e-beam evaporation can be conducted. After deposition, the resist and the deposited materials (catalyst and under-layer) above it can be removed by soaking the wafer in acetone. Thus, catalyst and under-layer will be only found on the bottom of the TSVs.

In order to evaluate the interfacial strength between CNT and Cu, pull-out tests can be conducted on the samples shown in Fig. 76 using atomic force microscope (AFM). Hence, the obtained results can be compared to the current results of the MD simulations.

APPENDIX A

ATOMISTIC SIMULATION PROCEDURE

A.1 Overview

In this appendix, a detailed description of the atomistic simulation procedures, from building the structure to running the MD simulation, is discussed. There are plenty of software packages that can be used to build the atomic structure for MD simulations. ASE [60] is a Python written programing language that is designed to setting up, steering and analyzing atomistic simulations. ASE facilitates setting up complicated atomistic structures e.g. nanotubes, graphene sheets, composites, etc. Therefore, ASE is used to build the atomistic structure of CNT/Cu-composite. After building the structure, LAMMPS is used to run the MD simulations. Following is a step-by-step illustration of the atomistic simulation procedures.

A.2 Procedure of Building the Atomistic Structure

ASE simulation is easier to run on Linux operating system, Thus, Ubuntu [129], an open source Debian-based Linux operating system, is installed. ASE is installed according to the instructions found on their webpage [130]. After installations are completed, Python is run from the Terminal command window of Ubuntu. The required objects (atoms, nanotube and graphical user interface) are then imported in order to start writing the commands. The commands used to import the required objects are:

```
from ase.lattice.surface import nanotube,fcc100,add_adsorbate,view, write
```

Objects “nanotube”, “fcc100”, add_adsorbate”, “view, and “write” are the objects used to build CNTs, build Cu slab, add CNTs to Cu slab, view the structure, and write the xyz file, respectively.

The command used to build the structure of the CNTs is

CNT1=nanotube(n, m, length=L)

such that CNT1 is a user defined name for the CNT, n and m are the chiral indices of the CNT, and L is the CNT’s length. The command used to build the structure of Cu is

SLAB = fcc100('Cu', size=(X,Y,Z))

such that SLAB is a user defined named for the Cu slab, fcc001 describes the crystalline structure of the unit cell (face-centered cubic) and 100 is the lattice vector. X, Y and Z define the slab’s dimensions. Defined CNTs and Cu slab are then combined together in one structure using ‘add_adsorbate’ command as follows:

add_adsorbate(cnt1, slab, Z, position=(X,-Y))

such that X,Y and Z are the displacements of Cu slab with respect to the center of CNT.

The structure is then written in xyz-format file using write command (write('slab.xyz', slab)).

In order to check the structure graphically, the command (ag) can be used to view the structure.

A.3 Procedure of Running the MD Simulation

A data file is created from the xyz file exported from ASE. The data file is a typical LAMMPS text file that contains the simulation box size and atoms numbers, types and positions. In order to minimize the calculation time, an access to a High Performance Computing (HPC) cluster is obtained. Each cluster has its own access regulations and procedures—they are not universal. The input file is then created. The input file reads the data

file and includes the MD simulation commands that define the interatomic potential energies, step time, simulation time, ensembles, loads, results, output files. Assigning the interatomic potentials to the atoms is not trivial in LAMMPS, specially, when the number of atom types gets larger. Maximum number of atoms used in the MD simulations is 12 atom types; atom-types 1:11 are assigned to CNT1 to CNT11 and atom-type 12 is assigned to Cu. The potentials between all the different atoms have to be defined as shown in Fig. 77. The command pair_style defines the types of potentials used in the simulation and their associated parameters i.e. cut-off ratio and cut-off distances. The command pair_coeff defines the pair coefficients for the selected atom types. The potential between C atoms in the same tube is Airebo. The asterisks are used to assign all the atom types to the given potential, which is Airebo and the coefficients are extrapolated in an external file CH.airebo. These coefficient are assigned to the 11 CNTs. Therefore, there are 12 Cs in that command line. Cu will not be assigned to Airebo. Therefore, there is a NULL. The interatomic potential between Cu atoms (atom-type=12) is EAM and the coefficient are given in the external file cuu6.txt. Then, LJ potential is defined between all 11 CNTs and Cu. 1*11 12 means that this potential is assigned to the interaction between atom-types from 1 to 11 (11 CNTs) and atom-type 12 (Cu). Number 1 following lj/cut refers to the first lj/cut defined in the pair-style command. The following coefficients are ε, σ and cut-off distance, respectively. The second LJ potential is assigned to the interaction between CNTs using the same logic used for assigning the potential between CNTs and Cu.

```
pair_style hybrid airebo 2.5 l l lj/cut 7.70625 lj/cut 8.5 eam
pair_coeff * * airebo CH.airebo C C C C C C C C C C NULL
pair_coeff l2 l2 eam cuu6.txt
pair_coeff l*ll l2 lj/cut l 0.02578 3.0825 7.70625
pair_coeff l*l0 ll lj/cut 2 0.00284 3.4 8.5
pair_coeff l*9 l0 lj/cut 2 0.00284 3.4 8.5
pair_coeff l*8 9 lj/cut 2 0.00284 3.4 8.5
pair_coeff l*7 8 lj/cut 2 0.00284 3.4 8.5
pair_coeff l*6 7 lj/cut 2 0.00284 3.4 8.5
pair_coeff l*5 6 lj/cut 2 0.00284 3.4 8.5
pair_coeff l*4 5 lj/cut 2 0.00284 3.4 8.5
pair_coeff l*3 4 lj/cut 2 0.00284 3.4 8.5
pair_coeff l*2 3 lj/cut 2 0.00284 3.4 8.5
pair_coeff l 2 lj/cut 2 0.00284 3.4 8.5
```

Fig. 77: Assigning potentials in MD

In order to apply discrete displacement, a loop is needed to be defined. Looping in LAMMPS is not trivial either. Before starting the loop, a discrete displacement named Disstep of 0.1 Å is applied using the commands seen in Fig. 78.

```
variable Disstep equal 0.1
displace_atoms sidec move 0 ${Disstep} 0 units box
```

Fig. 78. Defining discrete displacement

Then, the required fixes and computes are defined and the system is run for 10,000 time steps. The loop is then started by giving it a label (looppull) as depicted in Fig. 79. The counter is defined by the variable Z (from 1:100). Then, displacement is applied, and the equilibration will run for 10,000 time-steps. Command next will change Z to the next value in the loop. Finally, moving to the following iteration in the loop (looppull) is done by the command jump SELF.

```
label looppull
variable Z loop 100
displace_atoms sidec move 0 ${Disstep} 0 units box
run 10000
next Z
jump SELF looppull
```

Fig. 79. Defining the loop

APPENDIX B

FABRICATION OF CARBON NANOFIBER/COPPER-INTERCONNECT

5.4 Introduction

The difference between CNFs and CNTs is the orientation of basal planes (graphene planes). As seen in Fig. 80, in CNTs basal plane angle (α_b) is zero, whereas it can take any value within the open interval (0,90) in CNFs.

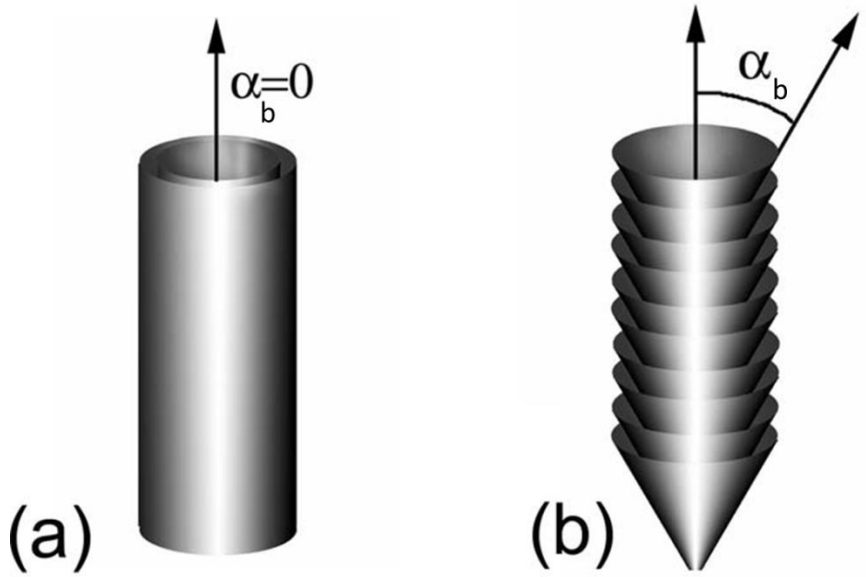

Fig. 80. Schematic of the difference between (a) CNTs and (b) CNFs (courtesy of [131])

CNF/Cu composite is proposed as lateral on-chip interconnects. In CNF, basal planes are conical and not parallel to the axis of the CNF. Therefore, electron transport will be a result of a serial combination of in- and out-of-basal plane conduction mechanisms [132]. CNF/Cu composite is used as general on-chip interconnect. It can be used in different forms of interconnects such as lines, interposers or vias. CNF-interconnects have been investigated extensively in the literature as replacement to Cu-interconnects [51,53,133]. The reliability of

CNF-interconnects was compared with ITRS requirements for next-generation microelectronics and they were found viable for future implementation in on-chip interconnects [132]. However, the obtained resistivity of CNF was found to be higher than that of Cu by one order of magnitude. Therefore, adding Cu between CNFs is believed to alleviate the resistivity of the interconnect.

5.5 Fabrication

This process does not include patterning and lithography because CNFs are grown on the surface of the substrate. Wafers are oxidized in a diffusion furnace to form insulation layer of 200-nm SiO_2. Then, 20-nm Ni catalyst is deposited using E-Beam evaporator. After Ni deposition, PECVD is carried out for CNF growth. Aixtron-Black Magic Pro is used for the PECVD process. The wafer is cleaned by 2 seconds of Ar flow at 500 sccm. Ni is then annealed by the flow of 200 sccm Amonia for 10 minutes at 650 °C. Then, plasma is turned on at 20 KHz alternating current and 150 W to start the PECVD growth process. Growth takes place by flowing C2H2 (precursor) and Amonia (annealing) at 100 sccm and 400 sccm for 30 minutes, respectively. Cu is then deposited using electroless deposition. Cu deposition is conducted by United Technologies Research Center.

5.6 Results

PECVD growth of CNFs is successful as shown in Fig. 81-a. The nanostructure is clearly CNFs since conical Basal planes could be observed from the Transmission Electron Microscope (TEM) images (Fig. 81-b). CNFs are around 4 μm long and diameters' range is 100-300 nm as shown in Fig. 81-a. They are very well aligned as well.

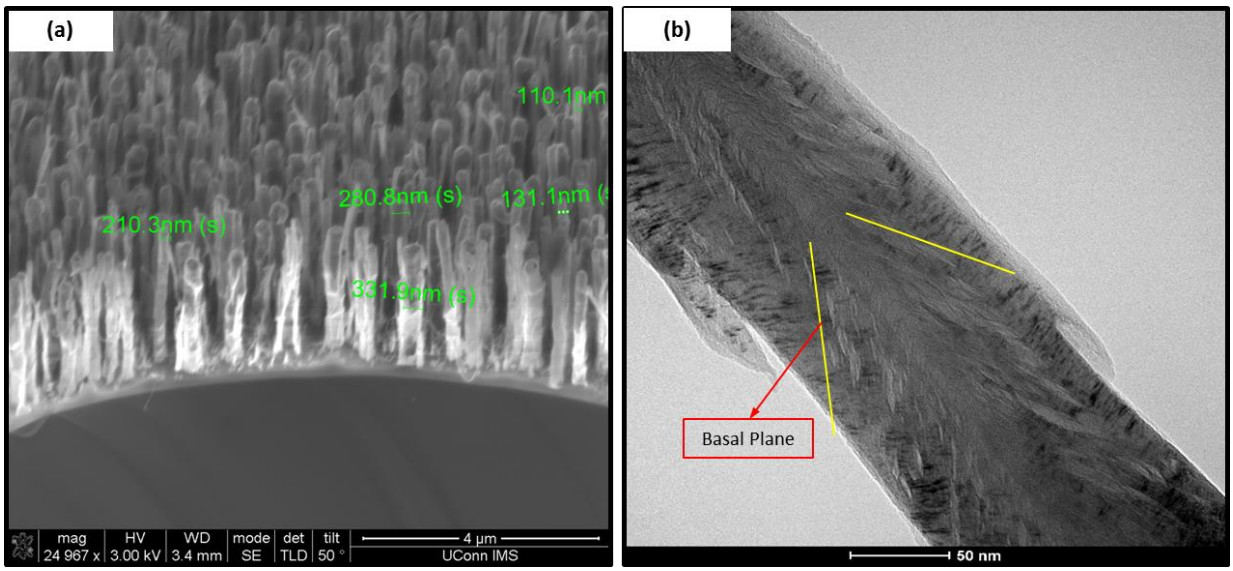

Fig. 81. Illustration of the grown CNFs using (a) SEM imaging and (b) TEM imaging

Cu is successfully deposited using electroless deposition as depicted in Fig. 82.

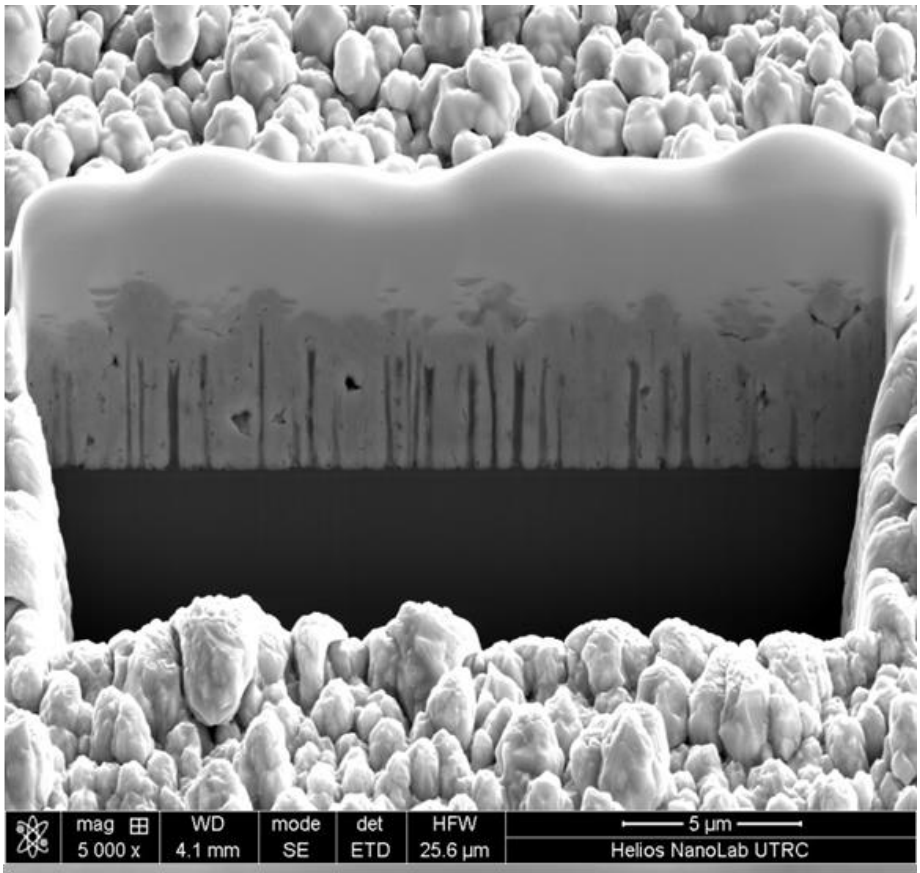
mag
5 000 x
WD
4.1 mm
mode
SE
det
ETD
HFW
25.6 µm
5 µm
Helios NanoLab UTRC

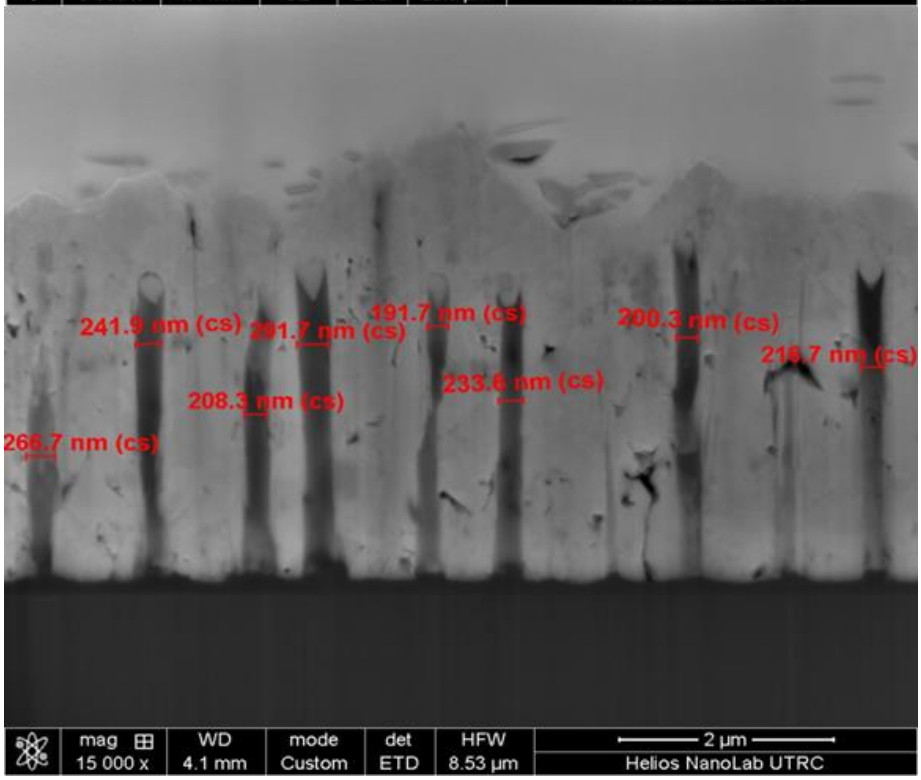
241.9 nm (cs)
291.7 nm (cs)
191.7 nm (cs)
200.3 nm (cs)
215.7 nm (cs)
233.6 nm (cs)
208.3 nm (cs)
266.7 nm (cs)
mag
15 000 x
WD
4.1 mm
mode
Custom
det
ETD
HFW
8.53 µm
2 µm
Helios NanoLab UTRC

Fig. 82. Cu-deposited CNFs

Resistivity of the CNF/Cu-composite is measured by using 4-Probe testing technique. Measurements were taken at seven different locations and the average obtained resistivity is found to be 1.88×10^{-5} Ω.cm, which is one order of magnitude lower than obtained CNF resistivity [51,132] and one order of magnitude higher than known Cu's resistivity [134] used for interconnects. However, Cu is incapable of maintaining its physical integrity at miniaturized scales due to low reliability and electro-migration issues that have not been observed in CNF structure [51,52,132,135]. Therefore, Cu addition to CNF enhanced the conductivity of CNF, and CNF/Cu-composite could be a good candidate to replace Cu in the next-generation interconnect.

5.7 Conclusion

CNFs have been studied extensively, and they have shown improved reliability and ampacity versus Cu. However, conductivity and mechanical stability of these nanostructures are yet issues that prohibit their application in interconnects industrially. Therefore, adding Cu is proposed to enhance the electrical and mechanical properties of these nanostructures. CNF/Cu-composite is proposed to be used as an interconnect for lateral connection. High quality self-aligned CNFs were successfully grown by PECVD. CNF/Cu-composite was also successfully developed using electroless plating. From 4-Probe resistivity measurements, CNF/Cu-Interconnect has shown one-order-of-magnitude improved resistivity to CNF alone. Nevertheless, the obtained resistivity is yet one order of magnitude higher than that of Cu-interconnects. However, Cu has shown its inability to maintain its physical integrity at the

miniaturized scales in the next-generation interconnects, which make CNF/Cu a reliable candidate to replace Cu.

REFERENCES

[1] W. Elmore, The transient response of damped linear networks with particular regard to wideband amplifiers, J. Appl. Phys. (1948). http://scitation.aip.org/content/aip/journal/jap/19/1/10.1063/1.1697872 (accessed June 4, 2015).

[2] GlobalFoundaries. 2012, GLOBALFOUNDRIES Fab 8 Adds Tools to Enable 3D Chip Stacking at 20nm and Beyond, 2012 Press Releases. (2012). http://www.globalfoundries.com/newsroom/press-releases/2012-press-releases/2014/03/01/globalfoundries-fab-8-adds-tools-to-enable-3d-chip-stacking-at-20nm-and-beyond.

[3] A.K. Tegueu, Fabrication and reliability testing of copper-filled through-silicon vias for three-dimensional chip stacking applications, (2010). http://gradworks.umi.com/34/39/3439818.html (accessed June 4, 2015).

[4] Global Interconnect Market 2015-2019, (n.d.). http://www.reportsnreports.com/reports/410523-global-interconnect-market-2015-2019.html.

[5] Three-dimensional Integrated Circuit (3D IC/Chip) & Through-Silicon Via (TSV) Interconnects Market - Global Forecast & Trend Analysis (2011 - 2016), (n.d.). http://www.marketsandmarkets.com/Market-Reports/3D-IC-Chip-and-TSV-Interconnect-Market-117.html.

[6] N. Srivastava, K. Banerjee, A comparative scaling analysis of metallic and carbon nanotube interconnections for nanometer scale VLSI technologies, (2004) 393–398. https://www.researchgate.net/publication/229027298_A_comparative_scaling_analysis_of_metallic_and_carbon_nanotube_interconnections_for_nanometer_scale_VLSI_technologies (accessed February 27, 2016).

[7] T. Wang, S. Chen, D. Jiang, Y. Fu, K. Jeppson, L. Ye, et al., Through-Silicon Vias Filled With Densified and Transferred Carbon Nanotube Forests, IEEE Electron Device Lett. 33 (2012) 420–422. doi:10.1109/LED.2011.2177804.

[8] Carbon Nanotube Devices: Properties, Modeling, Integration and Applications, John Wiley & Sons, 2008. https://books.google.com/books?hl=en&lr=&id=NjcM1Lqim3UC&pgis=1 (accessed June 5, 2015).

[9] T. Xu, Z. Wang, J. Miao, X. Chen, C.M. Tan, Aligned carbon nanotubes for through-wafer interconnects, Appl. Phys. Lett. 91 (2007) 042108. doi:10.1063/1.2759989.

[10] T. Wang, K. Jeppson, L. Ye, J. Liu, Carbon-nanotube through-silicon via interconnects for three-dimensional integration., Small. 7 (2011) 2313–7. doi:10.1002/smll.201100615.

[11] R. Xie, C. Zhang, M.H. van der Veen, K. Arstila, T. Hantschel, B. Chen, et al., Carbon

nanotube growth for through silicon via application., Nanotechnology. 24 (2013) 125603. doi:10.1088/0957-4484/24/12/125603.

[12] A. Jorio, G. Dresselhaus, M. Dresselhaus, Carbon Nanotubes: Advanced Topics in the Synthesis, Structure, Properties and Applications, Springer Berlin Heidelberg, 2008. doi:10.1007/978-3-540-72865-8.

[13] S. Saito, G. Dresselhaus, M.S. Dresselhaus, Physical Properties of Carbon Nanotubes, Imperial College Press, 1998. doi:10.1063/1.56490.

[14] P.J.F. Harris, Carbon nanotube science: synthesis, properties and applications, Cambridge University Press, 2009. http://centaur.reading.ac.uk/24738/.

[15] C. Subramaniam, T. Yamada, K. Kobashi, A. Sekiguchi, D.N. Futaba, M. Yumura, et al., One hundred fold increase in current carrying capacity in a carbon nanotube-copper composite., Nat. Commun. 4 (2013) 2202. doi:10.1038/ncomms3202.

[16] S. Iijima, Helical microtubules of graphitic carbon, Nature. 354 (1991) 56–58. doi:10.1038/354056a0.

[17] S. Iijima, P. Ajayan, T. Ichihashi, Growth model for carbon nanotubes., Phys. Rev. Lett. 69 (1992) 3100–3103. doi:10.1103/PhysRevLett.69.3100.

[18] R. Martel, T. Schmidt, H. Shea, Single-and multi-wall carbon nanotube field-effect transistors, Appl. Phys. …. (1998). http://scitation.aip.org/content/aip/journal/apl/73/17/10.1063/1.122477 (accessed December 29, 2015).

[19] S. Tans, A. Verschueren, C. Dekker, Room-temperature transistor based on a single carbon nanotube, Nature. (1998). http://www.nature.com/nature/journal/v393/n6680/abs/393049a0.html (accessed December 29, 2015).

[20] Q. Cao, S.-J. Han, J. Tersoff, A.D. Franklin, Y. Zhu, Z. Zhang, et al., End-bonded contacts for carbon nanotube transistors with low, size-independent resistance, Science (80-.). 350 (2015) 68–72. doi:10.1126/science.aac8006.

[21] M. Scarselli, P. Castrucci, M. De Crescenzi, Electronic and optoelectronic nano-devices based on carbon nanotubes., J. Phys. Condens. Matter. 24 (2012) 313202. doi:10.1088/0953-8984/24/31/313202.

[22] M.F.L. De Volder, S.H. Tawfick, R.H. Baughman, A.J. Hart, Carbon nanotubes: present and future commercial applications., Science. 339 (2013) 535–9. doi:10.1126/science.1222453.

[23] H. Li, C. Xu, N. Srivastava, K. Banerjee, Carbon Nanomaterials for Next-Generation Interconnects and Passives: Physics, Status, and Prospects, IEEE Trans. Electron Devices. 56 (2009) 1799–1821. doi:10.1109/TED.2009.2026524.

[24] G.L. Hornyak, J. Dutta, H.F. Tibbals, A. Rao, Introduction to Nanoscience, CRC Press, 2008. https://books.google.com/books?hl=en&lr=&id=FFzMBQAAQBAJ&pgis=1 (accessed August 23, 2015).

[25] C. Binns, Introduction to nanoscience and nanotechnology, 2010.

https://books.google.com/books?hl=en&lr=&id=3QA2n4sWGTIC&oi=fnd&pg=PR9&dq=Introduction+to+Nanoscience+and+Nanotechnology&ots=qZiJyc-V3L&sig=4GEz3dky6e72qGnAlX25gwIoZqc (accessed June 9, 2015).

[26] Automated Nanohandling by Microrobots, Springer Science & Business Media, 2007. https://books.google.com/books?id=rQJqln9nbEoC&pgis=1 (accessed February 26, 2016).

[27] Q. Wang, J. Dai, W. Li, Z. Wei, J. Jiang, The effects of CNT alignment on electrical conductivity and mechanical properties of SWNT/epoxy nanocomposites, Compos. Sci. Technol. 68 (2008) 1644–1648. doi:10.1016/j.compscitech.2008.02.024.

[28] T.-W. Chou, L. Gao, E.T. Thostenson, Z. Zhang, J.-H. Byun, An assessment of the science and technology of carbon nanotube-based fibers and composites, Compos. Sci. Technol. 70 (2010) 1–19. doi:10.1016/j.compscitech.2009.10.004.

[29] F.H. Gojny, M.H.G. Wichmann, U. Köpke, B. Fiedler, K. Schulte, Carbon nanotube-reinforced epoxy-composites: enhanced stiffness and fracture toughness at low nanotube content, Compos. Sci. Technol. 64 (2004) 2363–2371. doi:10.1016/j.compscitech.2004.04.002.

[30] J. Suhr, N. Koratkar, P. Keblinski, P. Ajayan, Viscoelasticity in carbon nanotube composites., Nat. Mater. 4 (2005) 134–7. doi:10.1038/nmat1293.

[31] J.N. Coleman, U. Khan, W.J. Blau, Y.K. Gun'ko, Small but strong: A review of the mechanical properties of carbon nanotube–polymer composites, Carbon N. Y. 44 (2006) 1624–1652. doi:10.1016/j.carbon.2006.02.038.

[32] S.R. Bakshi, A. Agarwal, An analysis of the factors affecting strengthening in carbon nanotube reinforced aluminum composites, Carbon N. Y. 49 (2011) 533–544. doi:10.1016/j.carbon.2010.09.054.

[33] T. Tsuda, T. Ogasawara, F. Deng, N. Takeda, Direct measurements of interfacial shear strength of multi-walled carbon nanotube / PEEK composite using a nano-pullout method, Compos. Sci. Technol. 71 (2011) 1295–1300. doi:10.1016/j.compscitech.2011.04.014.

[34] J.M. Wernik, B.J. Cornwell-Mott, S. a. Meguid, Determination of the interfacial properties of carbon nanotube reinforced polymer composites using atomistic-based continuum model, Int. J. Solids Struct. 49 (2012) 1852–1863. doi:10.1016/j.ijsolstr.2012.03.024.

[35] Y. Li, Y. Liu, X. Peng, C. Yan, S. Liu, N. Hu, Pull-out simulations on interfacial properties of carbon nanotube-reinforced polymer nanocomposites, Comput. Mater. Sci. 50 (2011) 1854–1860. doi:10.1016/j.commatsci.2011.01.029.

[36] B.-H. Kim, K.-R. Lee, Y.-C. Chung, J. Gunn Lee, Effects of interfacial bonding in the Si-carbon nanotube nanocomposite: A molecular dynamics approach, J. Appl. Phys. 112 (2012) 044312. doi:10.1063/1.4748133.

[37] L.Y. Jiang, Y. Huang, H. Jiang, G. Ravichandran, H. Gao, K.C. Hwang, et al., A cohesive law for carbon nanotube/polymer interfaces based on the van der Waals force, J. Mech. Phys. Solids. 54 (2006) 2436–2452. doi:10.1016/j.jmps.2006.04.009.

[38] H. Tan, L.Y. Jiang, Y. Huang, B. Liu, K.C. Hwang, The effect of van der Waals-based interface cohesive law on carbon nanotube-reinforced composite materials, Compos. Sci. Technol. 67 (2007) 2941–2946. doi:10.1016/j.compscitech.2007.05.016.

[39] L. Jiang, C. Nath, J. Samuel, S.S.G. Kapoor, Estimating the Cohesive Zone Model Parameters of Carbon Nanotube–Polymer Interface for Machining Simulations, J. Manuf. Sci. Eng. 136 (2014) 031004. doi:10.1115/1.4024941.

[40] S. Namilae, N. Chandra, Multiscale Model to Study the Effect of Interfaces in Carbon Nanotube-Based Composites, J. Eng. Mater. Technol. 127 (2005) 222. doi:10.1115/1.1857940.

[41] K.I. Tserpes, P. Papanikos, G. Labeas, S.G. Pantelakis, Multi-scale modeling of tensile behavior of carbon nanotube-reinforced composites, Theor. Appl. Fract. Mech. 49 (2008) 51–60. doi:10.1016/j.tafmec.2007.10.004.

[42] M.M. Shokrieh, R. Rafiee, Stochastic multi-scale modeling of CNT/polymer composites, Comput. Mater. Sci. 50 (2010) 437–446. doi:10.1016/j.commatsci.2010.08.036.

[43] J.M. Wernik, S.A. Meguid, Multiscale modeling of the nonlinear response of nano-reinforced polymers, Acta Mech. 217 (2010) 1–16. doi:10.1007/s00707-010-0377-7.

[44] A. Maiti, A. Ricca, Metal–nanotube interactions – binding energies and wetting properties, Chem. Phys. Lett. 395 (2004) 7–11. doi:10.1016/j.cplett.2004.07.024.

[45] N. Nemec, D. Tománek, G. Cuniberti, Contact Dependence of Carrier Injection in Carbon Nanotubes: An Ab Initio Study, Phys. Rev. Lett. 96 (2006) 076802. http://arxiv.org/abs/cond-mat/0512396.

[46] F. Banhart, Interactions between metals and carbon nanotubes: at the interface between old and new materials., Nanoscale. 1 (2009) 201–213. http://www.ncbi.nlm.nih.gov/pubmed/20644839.

[47] K. Toprak, Y. Bayazitoglu, Numerical modeling of a CNT–Cu coaxial nanowire in a vacuum to determine the thermal conductivity, Int. J. Heat Mass Transf. 61 (2013) 172–175. doi:10.1016/j.ijheatmasstransfer.2013.01.082.

[48] S. Hartmann, B. Wunderle, O. Hölck, Pull-Out Testing of SWCNTs Simulated by Molecular Dynamics, Int. J. Theor. Appl. Nanotechnol. 1 (2012) 59–65. doi:10.11159/ijtan.2012.009.

[49] S. Hartmann, O. Hblck, B. Wunderle, Molecular Dynamics Simulations for Mechanical Characterization of CNT IGoid Interface and its Bonding Strength, in: 14th Int. Conf. Therm. Mech. Multi-Physics Simul. Exp. Microelectron. Microsystems (EuroSimE), 2013, 2013: pp. 1–8.

[50] V. Desmaris, A.M. Saleem, S. Shafiee, J. Berg, M.S. Kabir, A. Johansson, Carbon Nanofibers (CNF) for enhanced solder-based nano-scale integration and on-chip interconnect solutions, in: 2014 IEEE 64th Electron. Components Technol. Conf., IEEE, 2014: pp. 1071–1076. doi:10.1109/ECTC.2014.6897421.

[51] Q. Ngo, T. Yamada, M. Suzuki, Structural and electrical characterization of carbon

nanofibers for interconnect via applications, Nanotechnology, …. (2007). http://ieeexplore.ieee.org/xpls/abs_all.jsp?arnumber=4359117 (accessed December 29, 2015).

[52] M. Nihei, A. Kawabata, D. Kondo, M. Horibe, S. Sato, Y. Awano, Electrical Properties of Carbon Nanotube Bundles for Future Via Interconnects, Jpn. J. Appl. Phys. 44 (2005) 1626–1628. doi:10.1143/JJAP.44.1626.

[53] Y. Ominami, Q. Ngo, M. Suzuki, A.J. Austin, C.Y. Yang, A.M. Cassell, et al., Interface characteristics of vertically aligned carbon nanofibers for interconnect applications, Appl. Phys. Lett. 89 (2006) 263114. doi:10.1063/1.2423241.

[54] K. Kannan, S. Kannan, B. Kim, Development of hybrid electrical model for CNT based Through Silicon Vias, in: 2013 IEEE Int. Symp. Circuits Syst., IEEE, 2013: pp. 1022–1026. doi:10.1109/ISCAS.2013.6572023.

[55] T. Wang, S. Chen, D. Jiang, Y. Fu, K. Jeppson, L. Ye, et al., Through-Silicon Vias Filled With Densified and Transferred Carbon Nanotube Forests, IEEE Electron Device Lett. 33 (2012) 420–422. doi:10.1109/LED.2011.2177804.

[56] M.B. Jordan, Y. Feng, S.L. Burkett, Development of seed layer for electrodeposition of copper on carbon nanotube bundles, J. Vac. Sci. Technol. B, Nanotechnol. Microelectron. Mater. Process. Meas. Phenom. 33 (2015) 021202. doi:10.1116/1.4907164.

[57] Y. Feng, S.L. Burkett, Fabrication and electrical performance of through silicon via interconnects filled with a copper/carbon nanotube composite, J. Vac. Sci. Technol. B, Nanotechnol. Microelectron. Mater. Process. Meas. Phenom. 33 (2015) 022004. doi:10.1116/1.4907417.

[58] Y. Li, G.D. Seidel, Multiscale modeling of the effects of nanoscale load transfer on the effective elastic properties of unfunctionalized carbon nanotube–polyethylene nanocomposites, Model. Simul. Mater. Sci. Eng. 22 (2014) 025023. doi:10.1088/0965-0393/22/2/025023.

[59] S. Plimpton, Fast Parallel Algorithms for Short-Range Molecular Dynamics, J. Comput. Phys. 117 (1995) 1–19. doi:10.1006/jcph.1995.1039.

[60] Center for Atomic-scale Materials Design, Atomic Simulation Environment, (2012). https://wiki.fysik.dtu.dk/ase/.

[61] V.V.& M.W.F. G. J. Acklandab, G. Tichyc, Simple N-body potentials for the noble metals and nickel, Philos. Mag. A. 56 (1987) 735–756. doi:10.1080/01418618708204485.

[62] S.J. Stuart, A.B. Tutein, J.A. Harrison, A reactive potential for hydrocarbons with intermolecular interactions, J. Chem. Phys. 112 (2000) 6472. doi:10.1063/1.481208.

[63] D.W. Brenner, O.A. Shenderova, J.A. Harrison, S.J. Stuart, B. Ni, S.B. Sinnott, A second-generation reactive empirical bond order (REBO) potential energy expression for hydrocarbons, J. Phys. Condens. Matter. 14 (2002) 783–802. doi:10.1088/0953-8984/14/4/312.

[64] K. Liew, C. Wong, X. He, M. Tan, S. Meguid, Nanomechanics of single and multiwalled carbon nanotubes, Phys. Rev. B. 69 (2004) 115429. doi:10.1103/PhysRevB.69.115429.

[65] C.H. Wong, V. Vijayaraghavan, Nanomechanics of Nonideal Single- and Double-Walled Carbon Nanotubes, J. Nanomater. 2012 (2012) 1–9. doi:10.1155/2012/490872.

[66] Y. Guo, W. Guo, Structural transformation of partially confined copper nanowires inside defected carbon nanotubes., Nanotechnology. 17 (2006) 4726–4730. http://www.ncbi.nlm.nih.gov/pubmed/21727604.

[67] J. Zhao, A. Buldum, J. Han, J. Lu, Gas molecule adsorption in carbon nanotubes and nanotube bundles, Nanotechnology. 13 (2002) 195–200. http://iopscience.iop.org/0957-4484/13/2/312 (accessed January 21, 2014).

[68] A. Volkov, R. Salaway, L. Zhigilei, Atomistic simulations, mesoscopic modeling, and theoretical analysis of thermal conductivity of bundles composed of carbon nanotubes, J. Appl. Phys. 114 (2013) 1–21. http://scitation.aip.org/content/aip/journal/jap/114/10/10.1063/1.4819911 (accessed January 21, 2014).

[69] C. Li, Y. Liu, X. Yao, M. Ito, T. Noguchi, Q. Zheng, Interfacial shear strengths between carbon nanotubes., Nanotechnology. 21 (2010) 115704. doi:10.1088/0957-4484/21/11/115704.

[70] H. Berendsen, Postma, van Gunsteren, DiNola, Molecular dynamics with coupling to an external bath, J. Chem. Phys. 81 (1984) 84–93. http://link.aip.org/link/?JCPSA6/81/3684/1 (accessed October 22, 2013).

[71] Yhteenveto suomeksi, Introduction to atomistic simulations 2008, (n.d.). http://www.physics.helsinki.fi/courses/s/compnano/exercises/exercise01.pdf.

[72] Temp/Berendsen - LAMMPS Documentation, (n.d.). http://lammps.sandia.gov/doc/fix_temp_berendsen.html.

[73] J.E. Jones, On the Determination of Molecular Fields. II. From the Equation of State of a Gas, Proc. R. Soc. A Math. Phys. Eng. Sci. 106 (1924) 463–477. doi:10.1098/rspa.1924.0082.

[74] R. Clausius, Physical Properties of Carbon Nanotubes [Paperback], World Scientific Publishing Company, London SW7 2BT, 1998. http://www.amazon.com/Physical-Properties-Carbon-Nanotubes-Saito/dp/1860942237 (accessed March 5, 2014).

[75] J.C. Maxwell, On Reciprocal Figures, Frames, and Diagrams of Forces, Trans. R. Soc. Edinburgh. 26 (2013) 1–40. doi:10.1017/S0080456800026351.

[76] R.J. Swenson, Comments on virial theorems for bounded systems, Am. J. Phys. 51 (1983) 940. doi:10.1119/1.13390.

[77] D.H. Tsai, The virial theorem and stress calculation in molecular dynamics, J. Chem. Phys. 70 (1979) 1375. doi:10.1063/1.437577.

[78] P.C. Andia, F. Costanzo, G.L. Gray, A classical mechanics approach to the determination of the stress–strain response of particle systems, Model. Simul. Mater.

Sci. Eng. 14 (2006) 741–757. doi:10.1088/0965-0393/14/4/015.

[79] F. Costanzo, G. Gray, P. Andia, On the definitions of effective stress and deformation gradient for use in MD: Hill's macro-homogeneity and the virial theorem, Int. J. Eng. …. (2005). http://www.sciencedirect.com/science/article/pii/S0020722505000376 (accessed July 29, 2014).

[80] M. Zhou, A new look at the atomic level virial stress: on continuum-molecular system equivalence, Proc. R. Soc. A Math. Phys. Eng. Sci. 459 (2003) 2347–2392. doi:10.1098/rspa.2003.1127.

[81] S. Shen, S. Atluri, Atomic-level stress calculation and continuum-molecular system equivalence, Comput. Model. Eng. …. (2004). http://care.eng.uci.edu/pdf/23.pdf (accessed July 30, 2014).

[82] Z.H. Sun, X.X. Wang, A.K. Soh, H.A. Wu, On stress calculations in atomistic simulations, Model. Simul. Mater. Sci. Eng. 14 (2006) 423–431. doi:10.1088/0965-0393/14/3/006.

[83] M.A. Tschopp, D.E. Spearot, D.L. McDowell, Atomistic simulations of homogeneous dislocation nucleation in single crystal copper, Model. Simul. Mater. Sci. Eng. 15 (2007) 693–709. doi:10.1088/0965-0393/15/7/001.

[84] Z. Yang, Y. Zhou, T. Wang, Q. Liu, Z. Lu, Crack propagation behaviors at Cu/SiC interface by molecular dynamics simulation, Comput. Mater. Sci. 82 (2014) 17–25. doi:10.1016/j.commatsci.2013.09.029.

[85] A.K. Subramaniyan, C.T. Sun, Continuum interpretation of virial stress in molecular simulations, Int. J. Solids Struct. 45 (2008) 4340–4346. doi:10.1016/j.ijsolstr.2008.03.016.

[86] J. Gao, J.H. Weiner, Excluded-volume effects in rubber elasticity. 1. Virial stress formulation, Macromolecules. 20 (1987) 2520–2525. doi:10.1021/ma00176a034.

[87] I. Awad, L. Ladani, Interfacial Strength Between Single Wall Carbon Nanotubes and Copper Material: Molecular Dynamics Simulation, J. Nanotechnol. Eng. Med. 4 (2014) 041002. doi:10.1115/1.4026939.

[88] T. Schneider, E. Stoll, Molecular-dynamics study of a three-dimensional one-component model for distortive phase transitions, Phys. Rev. B. 17 (1978) 1302–1322. doi:10.1103/PhysRevB.17.1302.

[89] L.J. Ladani, Numerical analysis of thermo-mechanical reliability of through silicon vias (TSVs) and solder interconnects in 3-dimensional integrated circuits, Microelectron. Eng. 87 (2010) 208–215. doi:10.1016/j.mee.2009.07.022.

[90] L.J. Ladani, Stress analysis of 3-dimensional IC package as function of structural design parameters, Microelectron. Eng. 87 (2010) 1852–1860. doi:10.1016/j.mee.2009.11.002.

[91] H. Jiang, B. Liu, Y. Huang, K.C. Hwang, Thermal Expansion of Single Wall Carbon Nanotubes, J. Eng. Mater. Technol. 126 (2004) 265. doi:10.1115/1.1752925.

[92] S. Park, H. Bang, H. Bang, J. You, Thermo-mechanical analysis of TSV and solder interconnects for different Cu pillar bump types, Microelectron. Eng. 99 (2012) 38–42.

doi:10.1016/j.mee.2012.05.056.

[93] S.-H. Choa, C.G. Song, H.S. Lee, Investigation of durability of TSV interconnect by numerical thermal fatigue analysis, Int. J. Precis. Eng. Manuf. 12 (2011) 589–596. doi:10.1007/s12541-011-0076-x.

[94] W. Shinoda, M. Shiga, M. Mikami, Rapid estimation of elastic constants by molecular dynamics simulation under constant stress, Phys. Rev. B. 69 (2004) 134103. doi:10.1103/PhysRevB.69.134103.

[95] N.R. Raravikar, P. Keblinski, A.M. Rao, M.S. Dresselhaus, L.S. Schadler, P.M. Ajayan, Temperature dependence of radial breathing mode Raman frequency of single-walled carbon nanotubes, Phys. Rev. B. 66 (2002) 235424. doi:10.1103/PhysRevB.66.235424.

[96] S.F. Choudhury, L. Ladani, Effect of Intermetallic Compounds on the Thermomechanical Fatigue Life of Three-Dimensional Integrated Circuit Package Microsolder Bumps: Finite Element Analysis and Study, J. Electron. Packag. 137 (2015) 041003. doi:10.1115/1.4031523.

[97] L. Ladani, Copper-CNT Hybrid TSVs: Thermo-Mechanical Stresses and Reliability Analysis, Int. J. High Speed Electron. Syst. 24 (2015) 1550006. doi:10.1142/S0129156415500068.

[98] R. Bennewitz, T. Gyalog, M. Guggisberg, M. Bammerlin, E. Meyer, H.-J. Güntherodt, Atomic-scale stick-slip processes on Cu(111), Phys. Rev. B. 60 (1999) R11301–R11304. doi:10.1103/PhysRevB.60.R11301.

[99] J. Gao, W.D. Luedtke, D. Gourdon, M. Ruths, J.N. Israelachvili, U. Landman, Frictional Forces and Amontons' Law: From the Molecular to the Macroscopic Scale, J. Phys. Chem. B. 108 (2004) 3410–3425. doi:10.1021/jp036362l.

[100] Y. Li, N. Hu, G. Yamamoto, Z. Wang, T. Hashida, H. Asanuma, et al., Molecular mechanics simulation of the sliding behavior between nested walls in a multi-walled carbon nanotube, Carbon N. Y. 48 (2010) 2934–2940. http://www.sciencedirect.com/science/article/pii/S0008622310002824 (accessed October 3, 2013).

[101] S. Liu, N. Hu, G. Yamamoto, Y. Cai, Y. Zhang, Y. Liu, et al., Investigation on CNT/alumina interface properties using molecular mechanics simulations, Carbon N. Y. 49 (2011) 3701–3704. doi:10.1016/j.carbon.2011.04.059.

[102] G.. Barenblatt, The formation of equilibrium cracks during brittle fracture. General ideas and hypotheses. Axially-symmetric cracks, J. Appl. Math. Mech. 23 (1959) 622–636. doi:10.1016/0021-8928(59)90157-1.

[103] IBM, SPSS, (n.d.). http://www-01.ibm.com/software/analytics/spss/.

[104] MathWorks, Signal Smoothing, (n.d.). http://www.mathworks.com/help/signal/examples/signal-smoothing.html.

[105] I. Awad, L. Ladani, Cohesive Zone Model for the Interface of Multi-walled Carbon Nanotubes and Copper: Molecular Dynamics Simulation, J. Nanotechnol. Eng. Med. 5 (2014) 031007. doi:10.1115/1.4029462.

[106] O.H. Yeoh, Some Forms of the Strain Energy Function for Rubber, Rubber Chem. Technol. 66 (1993) 754–771. doi:10.5254/1.3538343.

[107] C.C. Hwang, Y.C. Wang, Q.Y. Kuo, J.M. Lu, Molecular dynamics study of multi-walled carbon nanotubes under uniaxial loading, Phys. E Low-Dimensional Syst. Nanostructures. 42 (2010) 775–778. doi:10.1016/j.physe.2009.10.064.

[108] Y. Han, J. Elliott, Molecular dynamics simulations of the elastic properties of polymer/carbon nanotube composites, Comput. Mater. Sci. 39 (2007) 315–323. doi:10.1016/j.commatsci.2006.06.011.

[109] S. Frankland, The stress–strain behavior of polymer–nanotube composites from molecular dynamics simulation, Compos. Sci. Technol. 63 (2003) 1655–1661. doi:10.1016/S0266-3538(03)00059-9.

[110] P.K. Schelling, P. Keblinski, Thermal expansion of carbon structures, Phys. Rev. B. 68 (2003) 035425. doi:10.1103/PhysRevB.68.035425.

[111] N. Hu, B. Jia, M. Arai, C. Yan, J. Li, Y. Liu, et al., Prediction of thermal expansion properties of carbon nanotubes using molecular dynamics simulations, Comput. Mater. Sci. 54 (2012) 249–254. doi:10.1016/j.commatsci.2011.10.015.

[112] I. Awad, L. Ladani, Mechanical integrity of a carbon nanotube/copper-based through-silicon via for 3D integrated circuits: a multi-scale modeling approach., Nanotechnology. 26 (2015) 485705. doi:10.1088/0957-4484/26/48/485705.

[113] Kuo-Ning Chiang, Yung-Te Lin, Hsien-Chie Cheng, On enhancing eutectic solder joint reliability using a second-reflow-process approach, IEEE Trans. Adv. Packag. 23 (2000) 9–14. doi:10.1109/6040.826755.

[114] C.-T. Peng, C.-M. Liu, J.-C. Lin, H.-C. Cheng, K.-N. Chiang, Reliability Analysis and Design for the Fine-Pitch Flip Chip BGA Packaging, IEEE Trans. Components Packag. Technol. 27 (2004) 684–693. doi:10.1109/TCAPT.2004.838867.

[115] S.F. Choudhury, L. Ladani, Effect of Intermetallic Compounds on the Thermomechanical Fatigue Life of Three-Dimensional Integrated Circuit Package Microsolder Bumps: Finite Element Analysis and Study, J. Electron. Packag. 137 (2015) 041003. doi:10.1115/1.4031523.

[116] R.R. Tummala, P.M. Raj, A. Aggarwal, G. Mehrotra, S. Bansal, C.K. Ong, et al., Copper Interconnections for High Performance and Fine Pitch Flipchip Digital Applications and Ultra-Miniaturized RF Module Applications, in: 56th Electron. Components Technol. Conf. 2006, IEEE, 2006: pp. 102–111. doi:10.1109/ECTC.2006.1645632.

[117] F. Laermer, A. Schilp, Method of anisotropically etching silicon, (1994). http://www.freepatentsonline.com/5501893.html (accessed January 4, 2016).

[118] K.B.K. Teo, M. Chhowalla, G.A.J. Amaratunga, W.I. Milne, G. Pirio, P. Legagneux, et al., Characterization of plasma-enhanced chemical vapor deposition carbon nanotubes by Auger electron spectroscopy, J. Vac. Sci. Technol. B Microelectron. Nanom. Struct. 20 (2002) 116. doi:10.1116/1.1428281.

[119] V.I. Merkulov, A. V. Melechko, M.A. Guillorn, D.H. Lowndes, M.L. Simpson, Effects of spatial separation on the growth of vertically aligned carbon nanofibers produced by plasma-enhanced chemical vapor deposition, Appl. Phys. Lett. 80 (2002) 476. doi:10.1063/1.1433905.

[120] T. de los Arcos, M. Gunnar Garnier, P. Oelhafen, D. Mathys, J. Won Seo, C. Domingo, et al., Strong influence of buffer layer type on carbon nanotube characteristics, Carbon N. Y. 42 (2004) 187–190. doi:10.1016/j.carbon.2003.10.020.

[121] P.B. Amama, C.L. Pint, S.M. Kim, L. McJilton, K.G. Eyink, E.A. Stach, et al., Influence of alumina type on the evolution and activity of alumina-supported Fe catalysts in single-walled carbon nanotube carpet growth., ACS Nano. 4 (2010) 895–904. doi:10.1021/nn901700u.

[122] C.J. Lee, J. Park, Y. Huh, J. Yong Lee, Temperature effect on the growth of carbon nanotubes using thermal chemical vapor deposition, Chem. Phys. Lett. 343 (2001) 33–38. doi:10.1016/S0009-2614(01)00680-7.

[123] N. Behabtu, C.C. Young, D.E. Tsentalovich, O. Kleinerman, X. Wang, A.W.K. Ma, et al., Strong, light, multifunctional fibers of carbon nanotubes with ultrahigh conductivity., Science. 339 (2013) 182–6. doi:10.1126/science.1228061.

[124] Y. Chai, K. Zhang, M. Zhang, P.C.H. Chan, M.M.F. Yuen, Carbon Nanotube/Copper Composites for Via Filling and Thermal Management, in: 2007 Proc. 57th Electron. Components Technol. Conf., IEEE, 2007: pp. 1224–1229. doi:10.1109/ECTC.2007.373950.

[125] Q. Chen, Carbon nanotube reinforced metal composites, US Pat. 7,651,766. (2010). https://www.google.com/patents/US7651766 (accessed February 3, 2016).

[126] C.L. Pint, Y.-Q. Xu, M. Pasquali, R.H. Hauge, Formation of highly dense aligned ribbons and transparent films of single-walled carbon nanotubes directly from carpets., ACS Nano. 2 (2008) 1871–8. doi:10.1021/nn8003718.

[127] S. Kishimoto, Y. Kojima, Y. Ohno, T. Sugai, H. Shinohara, T. Mizutani, Growth of mm-Long Carbon Nanotubes by Grid-Inserted Plasma-Enhanced Chemical Vapor Deposition, Jpn. J. Appl. Phys. 44 (2005) 1554–1557. doi:10.1143/JJAP.44.1554.

[128] Y. Kojima, S. Kishimoto, T. Mizutani, Low-Temperature Growth of Carbon Nanotubes by Grid-Inserted Plasma-Enhanced Chemical Vapor Deposition, Jpn. J. Appl. Phys. 46 (2007) 8000–8002. doi:10.1143/JJAP.46.8000.

[129] Ubuntu, Canonical Ltd., Ubuntu Community. (n.d.). http://www.ubuntu.com/download.

[130] ASE Installation, (n.d.). https://wiki.fysik.dtu.dk/ase/download.html.

[131] A. V. Melechko, K.L. Klein, J.D. Fowlkes, D.K. Hensley, I.A. Merkulov, T.E. McKnight, et al., Control of carbon nanostructure: From nanofiber toward nanotube and back, J. Appl. Phys. 102 (2007) 074314. doi:10.1063/1.2786710.

[132] A.M. Cassell, A.J. Austin, S. Krishnan, M. Meyyappan, C.Y. Yang, Characteristics of aligned carbon nanofibers for interconnect via applications, IEEE Electron Device Lett. 27 (2006) 221–224. doi:10.1109/LED.2006.870865.

[133] Q. Ngo, B. Cruden, A. Cassell, Thermal interface properties of Cu-filled vertically aligned carbon nanofiber arrays, Nano Lett. (2004). http://pubs.acs.org/doi/abs/10.1021/nl048506t (accessed December 31, 2015).

[134] S.P. Murarka, S.W. Hymes, Copper metallization for ULSL and beyond, Crit. Rev. Solid State Mater. Sci. 20 (1995) 87–124. doi:10.1080/10408439508243732.

[135] B.Q. Wei, R. Vajtai, P.M. Ajayan, Reliability and current carrying capacity of carbon nanotubes, Appl. Phys. Lett. 79 (2001) 1172. doi:10.1063/1.1396632.